Harvesting Energy from Ambient Vibrations

A DISSERTATION SUBMITTED TO THE GRADUATE DIVISION OF THE UNIVERSITY OF HAWAI'I AT MĀNOA IN PARTIAL FULFILLMENT OF THE REQUIREMENTS FOR THE DEGREE OF

DOCTOR OF PHILOSOPHY

IN

CIVIL AND ENVIRONMENTAL ENGINEERING

August 2016

By

Hui Zhang

Dissertation Committee:

David T. Ma, Chairperson
Olga Boric-Lubecke
H. Ronald Riggs
Ian Robertson
Lin Shen

Keywords: Energy harvesting, Global resonance, Excitation roles, Energy transfer, Potential well, Period-one rotation

Abstract

In vibratory energy harvesting, the energy flow generally goes through three stages: the external vibration energy is firstly coupled into the device as kinetic energy, which is partially converted to electricity through electromechanical conversion unit (such as electromagnetic, piezoelectric, and electrostatic), then the generated electricity is applied to the electrical load circuit. The process of such energy flow indicates that the energy coupled in the first stage determines the maximum available energy converted to electricity, while the electricity delivered to the load depends on the characteristics of electrical load circuits. Note that the first stage for coupling energy is achieved by device dynamics. To best understand vibratory energy harvesting, the effects of device dynamics and electrical load circuits on energy harvesting performance are investigated in this dissertation.

For the effects of device dynamics, we do the study from four areas: parametric oscillator/device, global resonance, the roles of excitation, and dynamics outside the potential well. At first, we investigate the potential of using a nonlinear parametric oscillator/device to harvest energy. In such device, the excitation appears as a parameter of the dynamical system. Such parameterization of the excitation provides a cross-frequency energy transfer in the excitation, resulting in modifying the frequency content of the excitation, i.e. modulation of the excitation, which enables the device into the orbits of higher-order subharmonic oscillations more easily. A device with a pendulum-type architecture is proposed and used as an illustrative example.

The further investigation in device dynamics has proved that for a nonlinear device, there exists a generalized, global resonance condition which requires matching of all of the frequencies between the device and the excitation. Under global resonance, the device performance is optimized with the maximum energy harvesting efficiency, but its corresponding displacement is not the largest because the amplitude of global

resonance response is strongly correlated with the fundamental frequency supported by a nonlinear potential well (e.g. potential function). Such results suggest that traditionally relying only on increasing the device response in nonlinear systems can be misleading. The global resonance condition also shows that damping of the device and modulation of the excitation play critical roles in facilitating the frequency match required for resonance. According to the global resonance condition, it is revealed that the potential of nonlinear device in harvesting energy from multi-frequency vibrations benefits from multiple frequency match, not from the wider bandwidth obtained from single-frequency response. To harvest energy from multi-frequency vibration using nonlinear devices, a device-design concept based on global resonance is thus proposed.

When the global resonance condition is satisfied, the instantaneous power of the excitation is always non-negative, resulting in the maximum device performance. Conversely, when the condition is not satisfied, the excitation does negative work for a duration per cycle, leading to the reduction of the energy harvested. During such duration, the excitation actually takes energy back from the device, acting as a sink. The extent to which the excitation behaves as a sink determines the energy harvesting performance. We find that instantaneously changing device response to ensure the velocity in phase with the excitation can reduce the behavior of the excitation as a sink, resulting in dramatic increase of the energy harvested. Based on our findings, it has shown that an active method based on manipulating the roles of excitation would be more promising in bringing vibration energy harvesting to fruition.

Although the responses of a device are usually constrained by its potential well, it is possible for the dynamics of a pendulum-type device to escape from the potential well. Here, we also investigated the possibility of utilizing the dynamics outside the potential well of a device for harvesting energy from vibrations. A pendulum-type device is used as an example. Results show that when the device dynamics is outside the potential well and stays in stable orbits of period-one rotations, the harvested energy is proportional

to the energy level of the orbit, neither depending on the natural frequency of the device nor on the intensity of the excitation.

For the effects of electrical load circuits, we consider three types of non-resistive loads, such as a resistive load with a rectifier, a resistive load with a rectifier and a regulating capacitor, and a simple charging circuit consisting of a rectifier and a storing capacitor. Numerical results suggest that when the harvested energy is to be stored in capacitors, the ultimate voltages across capacitors are the same as the open-circuit voltage of the device minus the rectifier drop. For charging loads, therefore, the amount of stored energy is determined by the capacitance and the device performance under open circuit. Moreover, a larger capacitor is beneficial for an electromagnetic harvester, but not for a piezoelectrical harvester.

Acknowledgements

This research work would not have been possible without the support of many people. I owe my deepest gratitude to my supervisor, Prof. David T. Ma who was abundantly helpful and offered invaluable assistance, support and guidance for the research of this dissertation. His extensive expertise in structural engineering and nonlinear dynamics was invaluable for the critical review and editing of this manuscript.

Besides my advisor, deepest gratitude are also due to the members of my dissertation committee, Prof. Olga Boric-Lubecke, Prof. H. Ronald Riggs, Prof. Ian Robertson, and Prof. Lin Shen. Thanks them for agreeing to be on the committee for my dissertation and reviewing my work despite their extremely busy schedule. I really appreciate you for your invaluable comments and advice to help me improve my dissertation.

I would like to convey thanks to Prof. Ning-shou Xu who also gave constructive advice and guidance for my research. Special thanks also to all my graduate friends, especially for Lawrence Corr, thanks for his invaluable assistance in revising the abstract, introduction, and conclusions of my dissertation.

Last but not the least, I wish to express my love and gratitude to my beloved families: my parents Shui-fang Zhang and Jie-lian Hu, and my wife Rui Mao, for their understanding and endless love, through the duration of my studies. Financial support for this research work was provided by National Science Foundation (Grant No. CMMI 0758632), which is also highly acknowledged.

Contents

Abstract ii

Acknowledgements v

List of Figures x

1 Introduction 1

1.1 Background and Motivation 1

1.2 Literature Review 2

1.2.1 Mechanical Coupling 3

1.2.1.1 Linear mechanical coupling 3

1.2.1.2 Nonlinear mechanical coupling 4

1.2.2 Electrical Loads 5

1.3 Objectives of Dissertation 8

1.4 Organization of Dissertation 9

2 Parametrically Excited Nonlinear Energy Harvester 11

2.1 Proposed Device Architecture 11

2.2 Theoretical Analysis 16

2.2.1 Dynamics Response 16

2.2.2 Power Output 19

2.2.2.1 Optimal damping level 20

2.2.2.2 Power delivered to electrical load 20

2.2.3 Electromotive Forces and Voltages 22

2.3 Experiments . . . 24
2.3.1 Prototype Device . . . 24
2.3.2 Experiment Setup . . . 26
2.3.3 Results . . . 26
2.3.3.1 Device characterization . . . 26
2.3.3.2 Device performance . . . 26
2.3.4 Comparison with Linear Harvesters . . . 31
2.4 Concluding Remarks . . . 32

3 Full Potential of Nonlinear Energy Harvesting within potential well - Global Resonance 34

3.1 Theoretical Analysis . . . 35
3.1.1 Global Resonance Condition . . . 35
3.1.2 Comparison with Sub- and Super-harmonic Oscillations . . . 37
3.2 Demonstration . . . 38
3.2.1 Device and Experiment Setup . . . 38
3.2.2 Theoretical Results . . . 40
3.3 Results and Discussion . . . 42
3.4 Concluding Remarks . . . 43

4 Potential of Using Global Resonance to Enhance Energy Harvesting Performance 47

4.1 Governing Equation . . . 48
4.2 Bandwidth . . . 50
4.2.1 Linear System . . . 50
4.2.2 Nonlinear System . . . 52
4.3 Large-Amplitude Response and Nonlinear Resonance . . . 56
4.4 Potential of Nonlinear Energy Harvesting . . . 57
4.5 Concluding Remarks . . . 69

5 Investigation of Using Dynamics Escaped from Potential Well to Enhance Vibrational Energy Harvesting 71

5.1 Theoretical Analysis . . . 71

5.1.1 Exact Solution . . . 72

5.1.2 Approximate Solution . . . 74

5.1.2.1 Iterative Method . . . 74

5.1.2.2 Under Vertical Excitation ($\alpha = 0$) . . . 75

5.1.2.3 Under Horizontal Excitation ($\alpha = \pi/2$) . . . 77

5.1.3 Power Output . . . 80

5.2 Experiments . . . 80

5.2.1 Device and Experiment Setup . . . 80

5.2.2 Bounds of Excitation Amplitude . . . 81

5.2.3 Device Performance . . . 83

5.3 Concluding Remarks . . . 90

6 Effects of Non-resistive Circuits on the Performance of Vibratory Energy Harvester 91

6.1 Theoretical Analysis . . . 92

6.1.1 Resistive Loads . . . 93

6.1.2 Non-Resistive Loads . . . 93

6.1.2.1 Electromagnetic vibration energy harvester . . . 95

6.1.2.2 Piezoelectric vibration energy harvester . . . 99

6.2 Results and Discussion . . . 103

6.2.1 Electromagnetic vibration energy harvester . . . 103

6.2.2 Piezoelectric vibration energy harvester . . . 114

6.3 Concluding Remarks . . . 125

7 Manipulating Roles of the Excitation to Enhance Energy Harvesting Performance 128

7.1 Theoretical analysis . . . 130

7.2 Experimental materials and model . . . 132

7.3 Results and Discussion . . . 135

7.4 Concluding Remarks . . . 137

8 Conclusions **142**

Bibliography **146**

List of Figures

1.1 Energy flow for vibratory energy harvesting 3

1.2 Frequency response of monostable Duffing harvester: X_a is the response amplitude, ω_0 is the linear fundamental frequency, and ω_f is the excitation frequency. 6

1.3 Potential function of bistable harvester: X is the displacement and $U(x)$ is the potential function. 7

2.1 Schematic diagram of proposed device architecture. 13

2.2 Schematic diagram of inductive energy converter and equivalent circuit. 14

2.3 Magnetic flux density 25

2.4 Experiment setup 27

2.5 Frequency response of the device ($A_e = 0.14g$ and $R_L = 15$ kilohms). Markers: Experimental; Dashed line: Numerically calculated; Solid line: Theoretical 28

2.6 Effect of total damping level. Markers: Experimental; Dashed lines: Numerically calculated; Solid lines: Theoretical 29

2.7 Power delivered to the electrical load. Markers: Experimental; Dashed lines: Numerically calculated; Solid lines: Theoretical 30

2.8 Effective value of voltages generated. Markers: Experimental; Dashed lines: Numerically calculated; Solid lines: Theoretical 31

2.9 Frequency responses of the proposed device and a linear device 32

3.1 Prototype device: (a) a schematic diagram and (b) the experiment apparatus (the shaker, electrical load and the oscilloscope are not shown). 39

3.2 Results of theoretical and numerical studies for the resonance and non-resonance cases under three types of excitations (torque, vertical and horizontal) with the same amplitude of $p = 0.3$. (a) A response curve of the angular displacement, (b) the phase angle between the response and forcing function, (c) the dissipated power and (d) the damping levels. Red: torque excitation, green: vertical excitation, and blue: horizontal excitation. 44

3.3 Experimental results of the device performance at resonance under horizontal excitations ($1:1$ and $3:1$ subharmonic oscillations) and a vertical excitation ($2:1$ subharmonic oscillations). (a) The power delivered to the electrical load, (b) the load resistance, (c) the phase between response and forcing function and (d) the scaled amplitude of the power of forcing function ($P_{fi} = i\hat{\omega}A_iA_{fi}$). Horizontal excitations: blue, vertical excitation: green. 45

4.1 Frequency response curve for the normalized average power dissipated of a linear system. 52

4.2 Frequency response curves for average power dissipated in two nonlinear systems, i.e. $P_d = \frac{1}{T}\int_0^T \gamma\dot{x}^2 \mathrm{dt}$ where $T = \frac{2\pi}{\omega}$. (a) and (c): $U(x) = \frac{1}{2}x^2 - \frac{1}{24}x^4$; (b) and (d): $U(x) = \frac{1}{2}x^2 + \frac{1}{24}x^4$. 54

4.3 Frequency response curves for average power dissipated P_d in two nonlinear systems: (a) $U(x) = \frac{1}{2}x^2 - \frac{1}{24}x^4$, $\gamma = 0.1$ N·s·m^{-1}·kg^{-1}, and $A_e = 0.15$ m·s^{-2}; (b) $U(x) = \frac{1}{2}x^2 + \frac{1}{24}x^4$, $\gamma = 0.1$ N·s·m^{-1}·kg^{-1}, and $A_e = 0.2$ m·s^{-2}. 55

4.4 Time histories for instantaneous power dissipated (i.e. $p_d(t) = \gamma\dot{x}^2$ in two nonlinear systems: (a) $U(x) = \frac{1}{2}x^2 - \frac{1}{24}x^4$, $\gamma = 0.1$ N·s·m^{-1}·kg^{-1}, and $A_e = 0.15$ m·s^{-2}; (b) $U(x) = \frac{1}{2}x^2 + \frac{1}{24}x^4$, $\gamma = 0.1$ N·s·m^{-1}·kg^{-1}, and $A_e = 0.2$ m·s^{-2}. 56

4.5 Performance comparison between the traditional nonlinear response and the response closed to global resonance: (a) Single-frequency response curve and undisturbed response curve for response amplitude of the nonlinear system with $U(x) = \frac{1}{2}x^2 - \frac{1}{4}x^4$, (b) system energy $E(t) = \frac{1}{2}\dot{x}^2 + U(x)$, (c) instantaneous power dissipated at response A, and (d) instantaneous power dissipated at response B. 58

4.6 Potential functions of nonlinear systems $U(x)$: (a) symmetric and (b) asymmetric. 59

4.7 Frequency content and time history of excitations: (a) and (c) excitation for the first example; (b) and (d) excitation for the second example. . . 61

4.8 Potential function and the frequency content of an undisturbed response: (a) and (c) proposed device for the first example ($U(x) = 30x^2 - 180x^4 + 123x^6$); (b) and (d) proposed device for the second example ($U(x) = 50x^2 + 16.5x^3$). 62

4.9 Frequency response under single-frequency excitation: (a) average dissipated power of monostable duffing device and (b) average dissipated power of bistable device. A_e is the excitation level. 63

4.10 Time histories of (a) the instantaneous power of the excitation $p_f(t)$ and (b) the dissipated power $p_d(t)$ in the first example. Proposed device: $U(x) = 30x^2 - 180x^4 + 123x^6$; Linear device: $U(x) = 2(1.144\pi)^2x^2$. . . 64

4.11 Time histories of (a) the instantaneous power of the excitation $p_f(t)$ and (b) the dissipated power $p_d(t)$ in the second example. Proposed device: $U(x) = 50x^2 + 16.5x^3$; Linear device: $U(x) = 2(1.013\pi)^2x^2$. 65

4.12 Time history of excitations which contain high-order harmonic noise for: (a) the first example and (b) the second example. 66

4.13 When the excitation contains high-order harmonic noise, time histories of (a) the instantaneous power of the excitation $p_f(t)$ and (b) the dissipated power $p_d(t)$ in the first example. Proposed device: $U(x) = 30x^2-180x^4+123x^6$; Linear device: $U(x) = 2(1.144\pi)^2x^2$. 67

4.14 When the excitation contains high-order harmonic noise, time histories of (a) the instantaneous power of the excitation $p_f(t)$ and (b) the dissipated power $p_d(t)$ in the second example. Proposed device: $U(x) = 50x^2 + 16.5x^3$; Linear device: $U(x) = 2(1.013\pi)^2x^2$. 68

5.1 (a)Prototype Device and (b) Experiment Setup 82

5.2 Bounds of excitation amplitude, p. Dotted: Theoretical (Equation (5.37)); Solid line with markers: Numerically calculated ($\triangle$:lower bound, $\bigtriangledown$: upper bound) 84

5.3 Frequency response of the device ($R_L = 10$ kΩ). Markers: Measured ($\triangle$: $0.14g$, $\bigcirc$: $0.18g$, $\bigtriangledown$: $0.22g$); Solid lines: Numerically calculated; Dotted: Theoretical 85

5.4 Load characteristics of harvester at 4Hz. Markers: Measured ($\triangle$: $0.14g$, $\bigcirc$: $0.18g$, $\bigtriangledown$: $0.22g$); Solid lines: Numerically calculated 88

5.5 Effect of excitation intensity on output power ($R_L = 10$ kΩ). Markers: Measured; Solid lines: Numerically calculated 89

6.1 Schematic diagram of a vibratory energy harvester with electrical load. 92

6.2 Three basic types of non-resistive load considered, (a) Resistive load with a full-bridge rectifier, (b) Resistive load with a full-bridge rectifier and a regulating capacitor C_r, and (c) the simplest charging circuit consisting of a full-bridge rectifier and an energy storing element (e.g. capacitor and battery). 94

6.3 Effects of a parallel capacitor on load characteristics of an electromagnetic harvester under the excitation of $A_e = 0.5g$ and $f_e = 25$Hz: (a) Velocity $\dot{x}$, (b) Work efficiency of the excitation $\eta = \frac{\int_0^{\frac{2\pi}{\omega}} F(x,t)\dot{x}\mathrm{dt}}{\int_0^{\frac{2\pi}{\omega}} |F(x,t)\dot{x}|\mathrm{dt}}$ where ω is the excitation frequency, (c) Average power delivered to the resistance P_L, and (d) Average input power of the excitation P_f. 105

6.4 Effects of a full-bridge rectifier on load characteristics of an electromagnetic harvester under the excitation of $A_e = 0.5g$ and $f_e = 25$Hz: (a) Velocity $\dot{x}$, (b) Work efficiency of the excitation $\eta = \frac{\int_0^{\frac{2\pi}{\omega}} F(x,t)\dot{x}\mathrm{dt}}{\int_0^{\frac{2\pi}{\omega}} |F(x,t)\dot{x}|\mathrm{dt}}$ where ω is the excitation frequency, (c) Average power delivered to the resistance P_L, and (d) Average input power of the excitation P_f. 106

6.5 Effects of a parallel capacitor with a full-bridge rectifier on load characteristics of an electromagnetic harvester under the excitation of $A_e = 0.5g$ and $f_e = 25$Hz: (a) Velocity $\dot{x}$, (b) Work efficiency of the excitation $\eta = \frac{\int_0^{\frac{2\pi}{\omega}} F(x,t)\dot{x}\mathrm{dt}}{\int_0^{\frac{2\pi}{\omega}} |F(x,t)\dot{x}|\mathrm{dt}}$ where ω is the excitation frequency, (c) Average power delivered to the resistance P_L, and (d) Average input power of the excitation P_f. 107

6.6 Effects of a parallel capacitor on single frequency-response performance of an electromagnetic harvester with a resistive load ($R_L = 1300\Omega$): (a) Velocity $\dot{x}$, (b) Work efficiency of the excitation $\eta = \frac{\int_0^{\frac{2\pi}{\omega}} F(x,t)\dot{x}\mathrm{dt}}{\int_0^{\frac{2\pi}{\omega}} |F(x,t)\dot{x}|\mathrm{dt}}$ where ω is the excitation frequency, (c) Average power delivered to the resistance P_L, and (d) Average input power of the excitation P_f. 109

6.7 Effects of a parallel capacitor on single frequency-response performance of an electromagnetic harvester with a resistive load ($R_L = 1300\Omega$): (a) Velocity $\dot{x}$, (b) Work efficiency of the excitation $\eta = \frac{\int_0^{\frac{2\pi}{\omega}} F(x,t)\dot{x}\mathrm{dt}}{\int_0^{\frac{2\pi}{\omega}} |F(x,t)\dot{x}|\mathrm{dt}}$ where ω is the excitation frequency, (c) Average power delivered to the resistance P_L, and (d) Average input power of the excitation P_f. The parameters of the electrical elements were $L_w = 0.003$H, $C_r = 0.003$F, and $R_w = 0.2\Omega$. 110

6.8 Effects of a full-bridge rectifier on single frequency-response performance of an electromagnetic harvester with a resistive load ($R_L = 1300\Omega$): (a) Velocity $\dot{x}$, (b) Work efficiency of the excitation $\eta = \frac{\int_0^{\frac{2\pi}{\omega}} F(x,t)\dot{x}\mathrm{dt}}{\int_0^{\frac{2\pi}{\omega}} |F(x,t)\dot{x}|\mathrm{dt}}$ where ω is the excitation frequency, (c) Average power delivered to the resistance P_L, and (d) Average input power of the excitation P_f. 112

6.9 Effects of a parallel capacitor with a full-bridge rectifier on single frequency-response performance of an electromagnetic harvester with a resistive load ($R_L = 1300\Omega$): (a) Velocity $\dot{x}$, (b) Work efficiency of the excitation $\eta = \frac{\int_0^{\frac{2\pi}{\omega}} F(x,t)\dot{x}\mathrm{dt}}{\int_0^{\frac{2\pi}{\omega}} |F(x,t)\dot{x}|\mathrm{dt}}$ where ω is the excitation frequency, (c) Average power delivered to the resistance P_L, and (d) Average input power of the excitation P_f. 113

6.10 When the electricity generated by an electromagnetic harvester is stored in capacitors, time history of: (a) Voltage across the capacitor $V_L(t)$ and (b) instantaneous power of the excitation $p_f(t)$. The excitation was fixed at $0.5g$ and 25 Hz, and the voltage drop was 0.8V. Blue: $C_s = 10$ mF; Red: $C_s = 5$ mF; and Dark: $C_s = 1$ mF. Time for charging the capacitor to 99% ultimate voltage ($V_{L_{ult}} = 4.42$ V) was 29.4 s for $C_s = 1$ mF, 143.6 s for $C_s = 5$ mF, and 286.4 s for $C_s = 10$ mF, respectively. At such time instant, the energy stored in the capacitor $E_{C_s} = \frac{1}{2}C_s V_L$ was 0.0096 J for $C_s = 1$ mF, 0.0479 J for $C_s = 5$ mF, and 0.0957 J for $C_s = 10$ mF, respectively. 115

6.11 Effects of a parallel capacitor on load characteristics of a piezoelectric harvester under the excitation of $A_e = 0.5g$ and $f_e = 121$Hz: (a) Velocity $\dot{x}$, (b) Work efficiency of the excitation $\eta = \frac{\int_0^{\frac{2\pi}{\omega}} F(x,t)\dot{x}\mathrm{dt}}{\int_0^{\frac{2\pi}{\omega}} |F(x,t)\dot{x}|\mathrm{dt}}$ where ω is the excitation frequency, (c) Average power delivered to the resistance P_L, and (d) Average input power of the excitation P_f. 117

6.12 Effects of a full-bridge rectifier on load characteristics of a piezoelectric harvester under the excitation of $A_e = 0.5g$ and $f_e = 121$Hz: (a) Velocity $\dot{x}$, (b) Work efficiency of the excitation $\eta = \frac{\int_0^{\frac{2\pi}{\omega}} F(x,t)\dot{x}\mathrm{dt}}{\int_0^{\frac{2\pi}{\omega}} |F(x,t)\dot{x}|\mathrm{dt}}$ where ω is the excitation frequency, (c) Average power delivered to the resistance P_L, and (d) Average input power of the excitation P_f. 118

6.13 Effects of a parallel capacitor with a full-bridge rectifier on load characteristics of a piezoelectric harvester under the excitation of $A_e = 0.5g$ and $f_e = 121$Hz: (a) Velocity $\dot{x}$, (b) Work efficiency of the excitation $\eta = \frac{\int_0^{\frac{2\pi}{\omega}} F(x,t)\dot{x}\mathrm{dt}}{\int_0^{\frac{2\pi}{\omega}} |F(x,t)\dot{x}|\mathrm{dt}}$ where ω is the excitation frequency, (c) Average power delivered to the resistance P_L, and (d) Average input power of the excitation P_f. 119

6.14 Effects of a parallel capacitor on single frequency-response performance of a piezoelectric harvester with a resistive load ($R_L = 3500\Omega$): (a) Velocity $\dot{x}$, (b) Work efficiency of the excitation $\eta = \frac{\int_0^{\frac{2\pi}{\omega}} F(x,t)\dot{x}\mathrm{dt}}{\int_0^{\frac{2\pi}{\omega}} |F(x,t)\dot{x}|\mathrm{dt}}$ where ω is the excitation frequency, (c) Average power delivered to the resistance P_L, and (d) Average input power of the excitation P_f. 121

6.15 Effects of a full-bridge rectifier on single frequency-response performance of a piezoelectric harvester with a resistive load ($R_L = 3500\Omega$): (a) Velocity $\dot{x}$, (b) Work efficiency of the excitation $\eta = \frac{\int_0^{\frac{2\pi}{\omega}} F(x,t)\dot{x}\mathrm{dt}}{\int_0^{\frac{2\pi}{\omega}} |F(x,t)\dot{x}|\mathrm{dt}}$ where ω is the excitation frequency, (c) Average power delivered to the resistance P_L, and (d) Average input power of the excitation P_f. 122

6.16 Effects of a parallel capacitor with a full-bridge rectifier on single frequency-response performance of a piezoelectric harvester with a resistive load ($R_L = 3500\Omega$): (a) Velocity $\dot{x}$, (b) Work efficiency of the excitation $\eta = \frac{\int_0^{\frac{2\pi}{\omega}} F(x,t)\dot{x}\mathrm{dt}}{\int_0^{\frac{2\pi}{\omega}} |F(x,t)\dot{x}|\mathrm{dt}}$ where ω is the excitation frequency, (c) Average power delivered to the resistance P_L, and (d) Average input power of the excitation P_f. 124

6.17 When the electricity generated by a piezoelectric harvester is stored in capacitors, time history of: (a) Voltage across the capacitor $V_L(t)$ and (b) instantaneous power of the excitation $p_f(t)$. The excitation was fixed at $0.5g$ and 146 Hz, and the voltage drop was 0.8V. Blue: $C_s = 1$ mF; Red: $C_s = 0.5$ mF; and Dark: $C_s = 0.1$ mF. Time for charging the capacitor to 99% ultimate voltage ($V_{L_{ult}} = 22.86$ V) was 90.7 s for $C_s = 0.1$ mF, 582.7 s for $C_s = 0.5$ mF, and 1246.9 s for $C_s = 1$ mF, respectively. At such time instant, the energy stored in the capacitor $E_{C_s} = \frac{1}{2}C_sV_L$ was 0.0256 J for $C_s = 0.1$ mF, 0.1280 J for $C_s = 0.5$ mF, and 0.2561 J for $C_s = 1$ mF, respectively. 126

7.1 Vector representation of the excitation $F(x,t)$ and the velocity of the response $\dot{x}(t)$. 133

7.2 Prototype Device. (a) Schematic diagrams, and (b) the experiment apparatus (the shaker, the electrical load, and the oscilloscope are not shown). 134

7.3 Relationship between diamagnetic force and the displacement. Line: fitting function, circle: experimental results, solid circle: rest position of the center of pyrolytic graphite. 135

7.4 Results obtained under single-frequency excitations ($R_L = 1$ kΩ). (a) The average power P_L delivered to the resistive load, (b) the coupling efficiency η, (c) changes in the positive and negative work of the excitations ΔW. Lines: numerical results, circles: experimental results. In (a) and (b), solid lines: the prototype device, dashed lines: the artificial system without the amplitude constraint. 138

7.5 The instantaneous work of single-frequency excitations ($A_e = 1$ g, $R_L = 1$ kΩ) for the five difference cases (i.e. I$\sim$V). Solid lines: the prototype device. Dashed lines: the artificial system without the amplitude constraint. 139

7.6 Numerical results obtained using band-limited excitations ($R_L = 1$ kΩ, bandwidth = 10 Hz, and PSD = 0.005π g^2·Hz^{-1}). (a) The average power P_L delivered to the resistive load, (b) the coupling efficiency η, and (c) the changes in the positive and negative work of the excitations ΔW. In (a) and (b), solid lines: the prototype device, dashed lines: the artificial system without the amplitude constraint. 140

Chapter 1

INTRODUCTION

1.1 Background and Motivation

Harvesting low-level, ambient energy from the environment has received significantly increasing attention over the last decades. Such dramatic growth in research efforts has been motivated by a number of factors. One of them is related to the desire of realizing autonomous and self-sustained long-term operation of miniature electronic devices (e.g., wireless sensors, transmitters, medical implantable devices, etc.). Advances in wireless and semiconductor manufacturing technologies have promoted the use of miniature electronic devices in different fields of technology, such as structural health monitoring, environmental monitoring, and in vivo biomedical implants, leading to significant changes. However, further evolution in these technologies has become stagnant due to the lack of a sustainable power supply. At present, the power supply of miniature devices is mainly based on batteries. Because of the limited lifespan, batteries must be replaced periodically, which can be expensive and challenging. For structural health monitoring, for instance, wireless sensors could be placed in remote locations or even embedded in structures, making the regular replacement of batteries infeasible. For medical implants (e.g. pacemakers), periodic battery replacement increases the risk of infection for patients. To solve such issues, it is necessary to replace battery technology with a sustainable energy supply to achieve autonomous and self-sustained long-term

operation of miniature devices. Considering the abundance of energy in the ambient environments, e.g. solar, wind, vibration, etc, and low-power consumption of miniature devices, development of energy harvesting technology appears to be a viable way of seeking an improved solution over the traditional battery based technology. Among these ambient energy sources, vibration energy is highly available in the environment around technical applications (e.g. vibrations of structures and machines, human motions, and ocean waves, etc), without limitation of weather condition, and thus has received much more attention in the literature.

1.2 Literature Review

Research efforts on harvesting energy from ambient vibrations to provide electricity for miniature devices were initiated in late 90's [1–5]. Numerous schemes and devices have been developed since then for a variety of applications, many of which have been summarized in review articles [6–12]. In general, an energy harvesting device consists of a mechanical coupling unit, which can be linear or nonlinear, and a means of electromechanical transduction (e.g. electromagnetic, piezoelectric, electrostatic, etc.). When an energy harvesting device is used for harvesting energy from vibrations, the energy flow usually goes through three stages, as shown in Figure 1.1: (1) the energy harvesting device utilizes its mechanical coupling unit to capture mechanical energy from vibration sources, (2) the coupled mechanical energy is partially converted to electricity through electromechanical transduction, and (3) the generated electricity is applied to electrical loads. From such energy flow, we can see that the performance of the mechanical coupling unit determines the maximum available energy for electromechanical conversion, while the electrical energy delivered to the load is strongly correlated to the characteristics of electrical loads. In this regard, the existing work has been reviewed with respect to these two aspects.

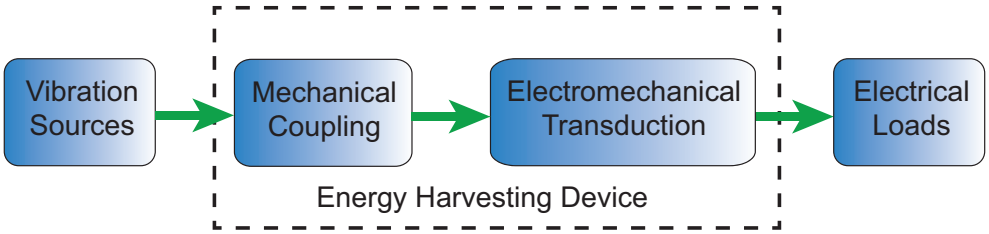

Figure 1.1: Energy flow for vibratory energy harvesting

1.2.1 Mechanical Coupling

1.2.1.1 Linear mechanical coupling

Energy harvesting devices have been designed based on linear mechanical coupling since the concept of vibration energy harvesting was proposed. Many linear devices can be found in review articles [6–8]. Note that linear energy harvesting devices mainly rely on a linear resonance condition to harvest energy. For an excitation with a fixed frequency, maximum device performance can be obtained when the natural frequency of the linear device is designed to be equal, or very close to, the excitation frequency. To obtain much more energy at resonance, these devices are also designed with low damping level (e.g. damping ratio smaller than 0.04), because the energy harvested at resonance is inversely proportional to the damping. If the excitation frequency has a slight offset from the resonance frequency, the performance of linear devices will dramatically decrease. In the real world, the energy of ambient vibrations is normally distributed over a wide spectrum of frequencies, or their dominant frequency is time-varying. For these kinds of excitations, relying on linear resonance to harvest energy becomes very difficult and challenging. On one hand, it is impossible to design the natural frequency of a purely passive linear device to target a time-varying frequency or multiple frequencies. On the other hand, the bandwidth of a linear device is proportional to its damping level. The bandwidth may be enlarged by increasing the damping level, however, it is achieved at the cost of reduced power output[1, 13].

To overcome these issues, resonance tuning mechanisms and arrays of harvesters have been introduced to linear energy harvesting [14]. Resonance tuning methods focus on tuning the natural frequency of a linear device to match the excitation frequency through passively/actively changing the stiffness or mass of the device [15–19]. Although the resonance of a device can be shifted via tunable methods when the excitation frequency changes slowly, resonance tuning mechanisms become ineffective when the excitation is broadband or its fundamental frequency changes rapidly. In addition, passive tuning methods need direct human interference to complete the resonance tuning, while active tuning methods usually require extra energy input to facilitate the adjustment of the natural frequency, resulting in low efficiency of the energy harvesting device. The methods based on arrays of harvesters generally design an array of harvesters with different natural frequencies such that at least one of them can be at resonance with one of the component of excitation [20–25]. While the device with an array of harvesters seems to be at resonance with multi-frequency excitation, only one of the harvesting elements is at resonance with one corresponding excitation frequency. Actually, such a design not only reduces power density, but also is not beneficial for the scalability of devices.

1.2.1.2 Nonlinear mechanical coupling

Recently, use of nonlinear mechanical coupling for enhanced energy-harvesting performance has been investigated. It has been shown that under certain conditions, the presence of mechanical nonlinearities in the device may lead to improved device performance as compared to the standard linear devices [26–30]. Thus, mechanical nonlinearities have been intentionally introduced to device design over the last decade, resulting in a variety of nonlinear energy harvesters, such as monostable Duffing harvesters [31–42], bistable harvesters [43–50], and vibro-impact harvesters [51–58]. For a monostable Duffing harvester, its potential function only has a single potential well. If the nonlinear

stiffness coefficient in the potential function is positive, the frequency response curve of a monostable harvester bends to the right, exhibiting a hardening nonlinearity; otherwise, its frequency response curve bends to the left, displaying a softening nonlinearity, as shown in Figure 1.2. Different from monostable Duffing harvesters, the potential function of a bistable harvester has two potential wells (Figure 1.3). If the potential energy of the device is within one of the two potential wells, the frequency response of the device exhibits a softening nonlinearity. However, if the potential energy of the device escapes from these two wells, the device response becomes larger, as compared to being within one of the two wells, and a hardening nonlinearity is exhibited. For a vibro-impact harvester, it usually consists of a linear harvester combined with obstacles/stoppers. Because of the presence of obstacles/stoppers, the device stiffness is globally nonlinear, even if it is piecewise linear, leading to nonlinear dynamic behaviors. Frequency response curves of nonlinear systems show that the large-amplitude response of a nonlinear device can be extended to a wider range of frequencies compared to that of a linear counterpart. Under single-frequency excitation, nonlinear energy harvesters may perform well over a broader spectrum of frequencies [10]. However, such "broadband"performance does not indicate that nonlinear harvesters still have satisfactory performance when the excitation contains multiple frequency components; this is due to the inapplicability of the principle of superposition. Therefore, nonlinear harvesters may not offer any benefit under multi-frequency excitations [59–62].

1.2.2 Electrical Loads

Electrical loads generally can be divided into two categories, energy dissipating element (i.e. electrical resistance) and energy storing element (e.g. capacitor and battery). For energy dissipating elements, they directly dissipate electrical energy through resistance no matter what the direction of current is, i.e. being suitable for alternating current

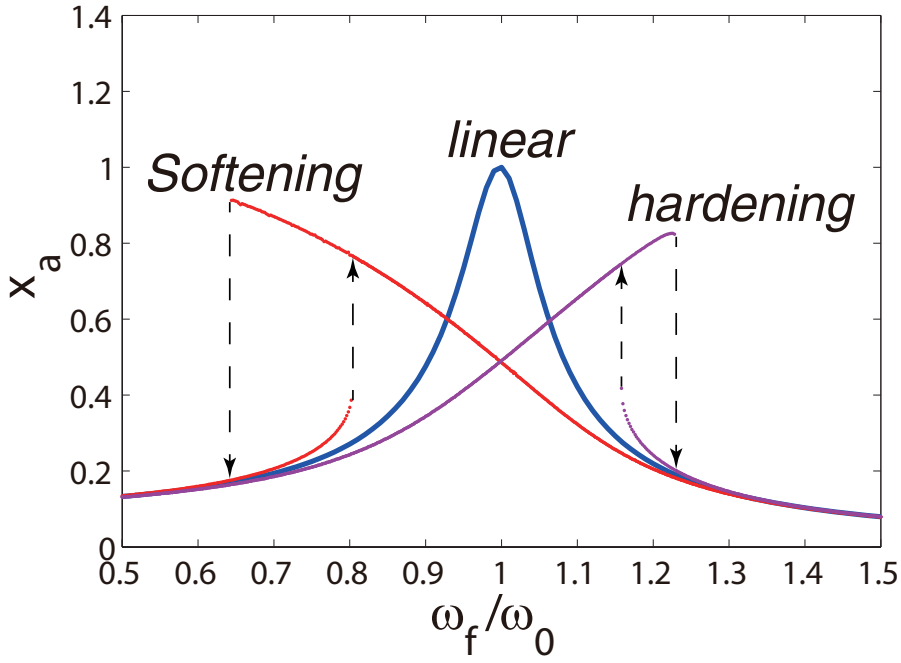

Figure 1.2: Frequency response of monostable Duffing harvester: X_a is the response amplitude, ω_0 is the linear fundamental frequency, and ω_f is the excitation frequency.

(AC) and direct current (DC). For energy storing elements, energy storage is achieved by the accumulation of electric charge. To realize charge accumulation, electric charge needs flow in one direction, i.e. only DC current, which can be directed to energy storing elements. Thus, AC current needs be converted to DC current through an AC-DC converter, such that it can be stored

In vibration energy harvesting, it is conventionally considered that the mechanical energy of a harvester is removed by damping (e.g. mechanical damping and electrical damping) [63]. Thus, the majority of existing schemes use the damping mechanism (i.e. electrical damping) to harvest energy. It is noticed that when electrical resistance is directly connected to a vibration energy harvester, the electromechanical effect of electrical resistance on device dynamics is usually simplified as an equivalent electrical damping. Therefore, electrical resistance has been traditionally considered in the performance evaluation of an energy harvesting device. Considering real applications,

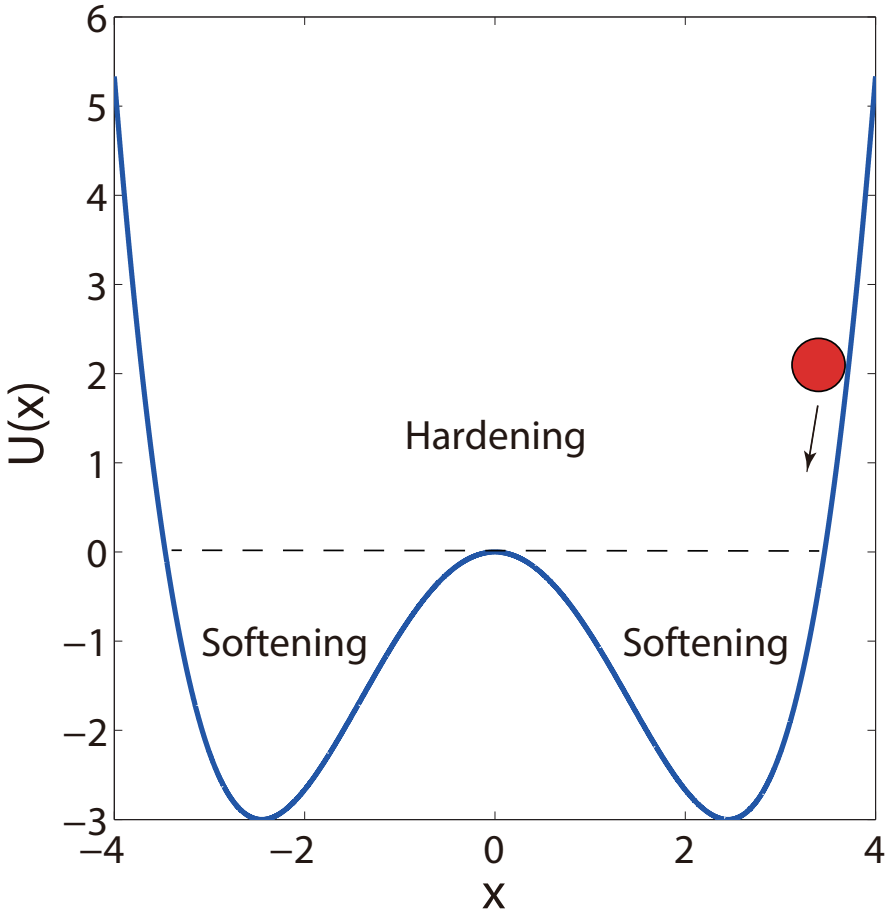

Figure 1.3: Potential function of bistable harvester: X is the displacement and $U(x)$ is the potential function.

harvesters connected to electrical resistance with an AC-DC converter has also been considered. To improve the efficiency of the AC-DC converter, a method of synchronized switch harvesting on inductor (SSHI) [64], which synchronizes the output voltage and current of the harvester, was developed and applied [65]. For the method of SSHI, it is usually assumed that the device response is independent of changes in the phase between the output voltage and current of the harvester [64, 66, 67]. This assumption may be applied to a harvester with a weak electromechanical coupling, but it is not true for strong electromechanical coupling; therefore, the method of SSHI may not offer any benefit when the electromechanical coupling is strong [64]. Although we have many existing conclusions about the device performance derived from electrical resistance, such device performance cannot be generalized for applications based on energy storing elements (e.g. capacitor and battery), because the characteristics of capacitors and batteries are very different to that of electrical resistance. It was shown that as more electrical energy is stored in capacitor and battery, voltage across capacitor and battery increases [68], resulting in changes in the reverse electromechanical effect, and thus changes in dynamics of the device.

1.3 Objectives of Dissertation

The aim of this dissertation is to develop and implement a method that will effectively enhance vibration energy harvesting. Considering the existing issues shown above, the effects of mechanical coupling and energy storing elements on energy harvesting performance are investigated in this dissertation. For the effects of mechanical coupling, some fundamental features of nonlinear systems are studied, such as parametric excitation, bandwidth, nonlinear resonance, and dynamics with potential energy outside the potential well. The objective of this dissertation is also to find a method which can effectively enhance the performance of the device under multi-frequency excitations.

For the effects of energy storing elements, a simple charging circuit, consisting of an AC-DC converter and an energy storage element, is considered. The effects of such charging circuit on device dynamics is numerically investigated.

1.4 Organization of Dissertation

This dissertation is organized as follows: In chapter 2, the potential of using a nonlinear parametric oscillator/device to harvest energy is investigated. A pendulum-type architecture with electromagnetic induction as the energy conversion mechanism is proposed as an illustrative example. A prototype device with a natural frequency of approximately 2Hz is fabricated and evaluated experimentally. The performance of the device is studied theoretically and numerically.

Chapter 3 presents the investigation on the fundamental features of nonlinear dynamic systems in the context of vibration-based energy harvesting. A generalized, global, multi-frequency resonance condition is shown to exist in nonlinear systems where the energy harvesting efficiency has been maximized. The function of modulation of the excitation in vibration energy harvesting is examined in this chapter. The difference between the global resonance and the traditional nonlinear vibrations (i.e. sub- and super-harmonic vibrations) is also discussed.

The fourth chapter provides some new insights into the potential of using nonlinear systems to harvest energy from vibrations with multiple frequencies. The misunderstanding about bandwidth and nonlinear resonance is introduced and corrected. The fundamental features of the traditional resonance is presented and compared to that of the global resonance. A device design concept based on global resonance is proposed in this chapter.

In Chapter 5, the potential of utilizing the dynamics outside the potential well of a

device for harvesting energy from vibrations is investigated. A pendulum-type system subjected to parametrical excitation is used to demonstrate the concept. The focus is placed on stable orbits of period-one rotations. The method of Iterative Harmonic Balance is used to solve the analytical approximations for period-one rotations. The performance of the device is studied theoretically and numerically.

Chapter 6 focuses on investigating the effects of non-resistive electrical circuits on the dynamics of a vibration energy harvester. Three types of non-resistive electrical loads, such as a resistance with a rectifier, a resistance with a rectifier and a regulating capacitor, and a simple charging circuit consisting of a rectifier and a storing capacitor, are considered. Numerical experiments are respectively carried out for electromagnetic vibratory energy harvester and piezoelectrical vibratory energy harvester.

In chapter 7, the role of excitation in energy harvesting applications is investigated. While the energy ultimately comes from the excitation, it is shown that the excitation may not always behave as a source of energy. When the device characteristics do not perfectly match the excitation, the excitation alternately behaves as an energy source and a sink. The extent to which the excitation behaves as a sink determines the energy harvesting efficiency. Such contradictory roles are shown to be dictated by a generalized phase defined as the instantaneous phase angle between the velocity of the device and the excitation. An inductive prototype device with a diamagnetically levitated seismic mass is proposed as a passive example to demonstrate the effect of changing the role of excitation on energy harvesting performance.

Lastly, chapter 8 summarizes the research findings and their implications in practical applications. The potential topics of further research are also discussed.

Chapter 2

PARAMETRICALLY EXCITED NONLINEAR ENERGY HARVESTER

Motivated by the fact that parametrically excited structures may generate larger response as compared to the case of linear resonance [69], the feasibility of utilizing parametrical resonance for enhanced energy harvesting performance is investigated in this chapter. A device with rigid-body based architecture was proposed and used as an illustrative example. A prototype device with a mini pendulum was designed, fabricated, and tested in laboratory. Results of theoretical and numerical studies were validated with experimental measurements.

2.1 Proposed Device Architecture

The proposed device architecture is schematically shown in Figure 2.1. The device consists of a pendulum and an energy converter. The pendulum has effective length and mass of L and M, respectively. After passing through a rectifier (REC), the generated electricity is delivered to an electric load, L_d. The energy converter consists of a rotor and a stator. A cylindrical permanent magnet that is free to rotate about its axis is used as the rotor. The stator consists of two sets of coils fixed to the housing, as schematically shown in Figure 2.2(a). When attached to a vibrating body (energy source), mechanical

energy is coupled into the device through the swing of the pendulum, which then generates electricity because of magnetic induction. Considering the case of vertical excitation and assuming that the device is significantly small compared to the source such that the effect of the device dynamics on the vibration of the source is negligible, the equation of motion of the device can be written as

$$\left(ML + \frac{J}{L}\right)\ddot{\theta}(t) + C_m L\dot{\theta}(t) + M\left[g + \ddot{y}_0(t)\right]\sin\theta + F_{em}\frac{\rho_w}{L} = 0 \tag{2.1}$$

where θ represents the angular position of the pendulum, J the moment inertia of the magnet and other rotating components, C_m the intrinsic viscous mechanical damping of the device, F_{em} the total tangential electromotive force generated by the coils, and ρ_w denotes the effective radius of the coils (Figure 2.1).

In order to focus on the mechanism of the energy harvesting method, the following assumptions are made.

1. The two sets of coils A and B are identical and positioned so that they are orthogonal to each other (Figure 2.2(a)). Symbols e_A, e_B and i_A, i_B respectively denote the instantaneous electromotive forces and currents in the respective winding. When at rest, the position of the magnet is specified by the angle between the magnetic axis and the center-line of one of the windings, ϕ (Figure 2.2(b));

2. The spatial distribution of magnetic flux density outside the rotor surface in the peripheral direction is sinusoidal, i.e. $B(\rho, \phi) = B_m(\rho)\cos(\phi)$, $\rho \geq \rho_R$, where $B_m(\rho)$ is the amplitude of the magnetic flux density at the radius ρ, which nearly decays exponentially with ρ. Symbol ρ_R denotes the radius of the magnet;

3. Windings A and B are connected to resistive electrical loads with the same resistance;

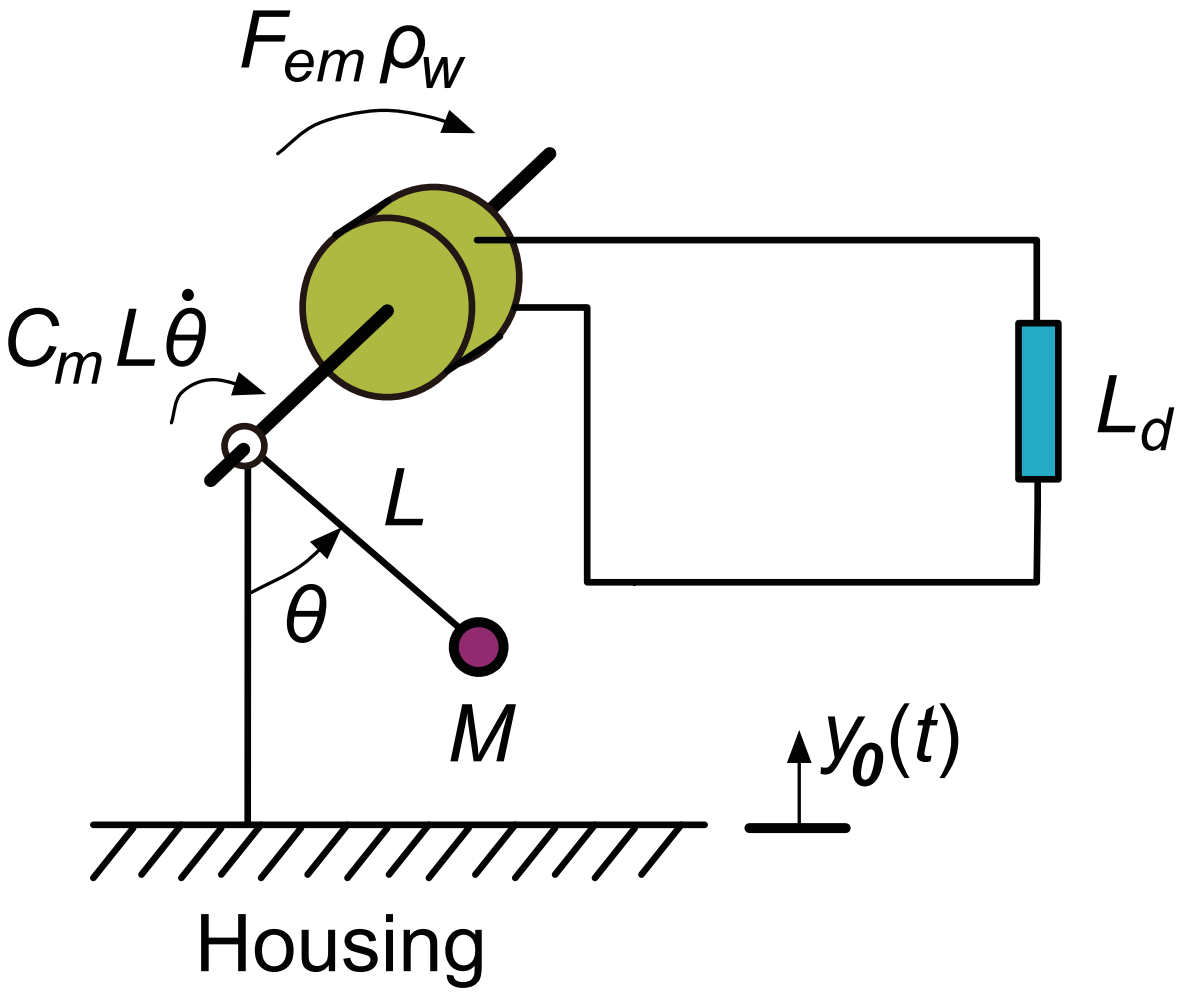

Figure 2.1: Schematic diagram of proposed device architecture.

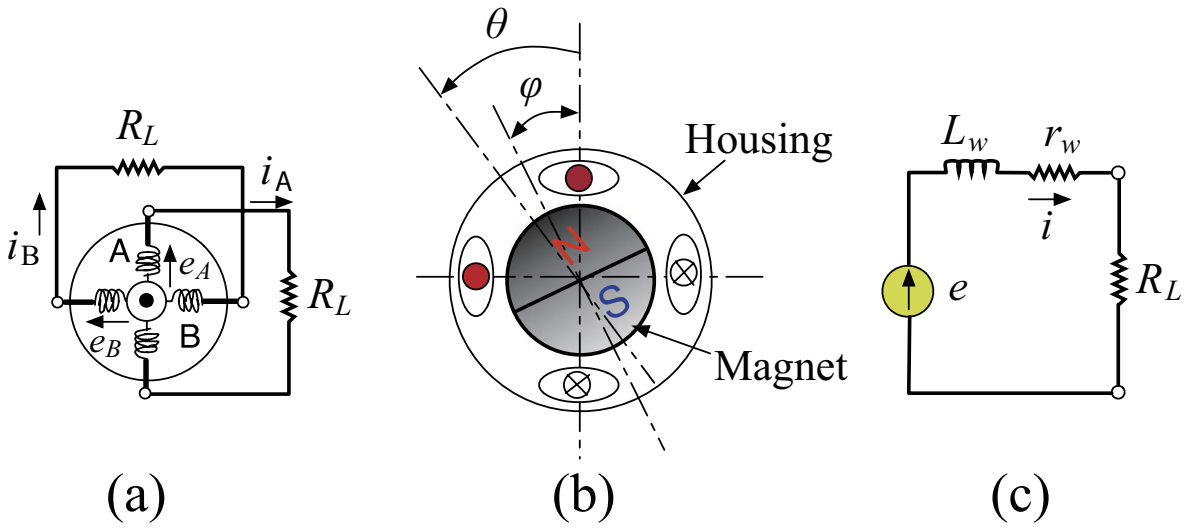

Figure 2.2: Schematic diagram of inductive energy converter and equivalent circuit.

4. No ferro-magnetic material is used as a core of the stator; eddy current and hysteresis loss are thus ignored.

It is noted that the electrical load circuit is assumed to be pure resistive. Such assumption may be violated in real-world applications, in which more complicated circuits may be involved. However, for applications with relatively simple circuits, such as the RLC circuits, the frequencies of which are normally orders of magnitude higher than that of the device, the effects of inductance and capacitance may be ignored due to such significant frequency mismatch. Under these assumptions, the equivalent electrical circuit of each winding is schematically shown in Figure 2.2(c), where r_w and L_w denote the internal resistance and the inductance of the winding, respectively. The resistance of the electrical load is denoted by R_L.

When the magnet rotates, the induced electromotive force across the two terminals of each winding is

$$\begin{cases} e_A = 2K_e\dot{\theta}\sin(\theta+\phi) \\ e_B = 2K_e\dot{\theta}\cos(\theta+\phi) \end{cases} \qquad K_e = WK_wB_{mw}l_R\rho_w \tag{2.2}$$

where W is the total number of turns (in series) of each winding, $K_w \leq 1$ the winding coefficient considering the distribution and short-pitch effects of the coils, l_R the length of the magnet, and B_{mw} is the maximum magnetic flux density at the centroid of the winding in the circumferential direction.

Based on Assumptions 3 and 4 and considering that the inductance of the winding is negligible at low frequencies, the currents in the windings can be approximated as $i_p \approx e_p/(r_w + R_L)$, $p = A$ or B. Using equation (2.2), the tangential electromagnetic force applied to the magnet can be written as

$$\begin{cases} F_{emA} = \hat{C}_e \dot{\theta} \sin^2(\theta + \phi) \\ F_{emB} = \hat{C}_e \dot{\theta} \cos^2(\theta + \phi) \end{cases} \quad \hat{C}_e = \frac{(2K_e)^2}{(r_w + R_L)\rho_w} \tag{2.3}$$

Thus, the total electromagnetic force F_{em} due to the two windings is $F_{em} = F_{emA} + F_{emB} = \hat{C}_e \dot{\theta}$ which is equivalent to a viscous damping force, with a damping coefficient, $\hat{C}_e$. The governing equation of the dynamics of the device can then be rewritten as

$$\left(ML + \frac{J}{L}\right) \ddot{\theta}(t) + CL\dot{\theta}(t) + M\left[g + \ddot{y}_0(t)\right] \sin\theta = 0 \tag{2.4}$$

where $C = C_m + C_e$ and

$$C_e = \frac{K_{Ce}}{r_w + R_L}, \quad K_{Ce} = \left(\frac{2K_e}{L}\right)^2 \tag{2.5}$$

Note that C_m represents the unusable portion of the total energy loss of the system, while C_e represents the portion that can be converted to electricity. As $r_w, R_L > 0$, the maximum achievable value of C_e is

$$C_{e,\max} = \frac{K_{Ce}}{r_w} \tag{2.6}$$

Furthermore, as there is no core loss according to Assumption 4, the total electrical energy is delivered to the electrical load R_L and the internal resistance of the coil, r_w. Denoting the total mechanical power dissipated as P_1, total electrical power generated as P_2, and electrical power delivered to the electrical load as P_L, the following relationships are readily established.

$$P_2 = \frac{C_e}{C_m + C_e} P_1, \quad P_L = \frac{R_L}{r_w + R_L} P_2 \tag{2.7}$$

The energy transfer efficiency of the system can be defined as

$$\eta_{tr} = \frac{P_L}{P_1} = \frac{\gamma_{Rr}}{(1+\gamma_{Rr})[1+(1+\gamma_{Rr})\gamma_{rC}]}, \quad \gamma_{Rr} = \frac{R_L}{r_w}, \quad \gamma_{rC} = \frac{r_w C_m}{K_{Ce}} \tag{2.8}$$

Note that the efficiency defined in (2.8) is related to the device property and the electrical load connected; it is independent of the level of external vibration.

2.2 Theoretical Analysis

2.2.1 Dynamics Response

In this study, harmonic excitations, i.e. $y_0(t) = A\cos\Omega t$, were considered. Under low-level excitations, equation (2.4) can be simplified as

$$\ddot{\theta}(t) + 2\beta\omega_n\dot{\theta}(t) + \left[\omega_n^2 - q\Omega^2\cos\Omega t\right]\left[\theta(t) + \gamma\theta^3(t)\right] = 0 \tag{2.9}$$

where $\omega_n = \sqrt{g/(L\lambda)}$, $\beta = C/(2\omega_n M\lambda)$, $\lambda = 1 + J/(ML^2)$ and $\gamma = -1/6$. Note that $\lambda \geq 1$ represents the effect of moment inertia of the magnet, which is equivalent to increasing the mass and length of the pendulum. The level of vibration of the source is represented by the normalized amplitude, $q = A/(L\lambda)$. When the excitation is

characterized by acceleration with amplitude of $A_e = A\Omega^2$, the normalized amplitude of the excitation becomes $q = A_e/[g(\Omega/\omega_n)^2]$.

For low-level excitation and damping, i.e. $\beta, q << 1$, it is convenient to introduce a scaling factor $\epsilon << 1$ such that $\beta = \epsilon\bar{\beta}$, $q = \epsilon\bar{q}$, $\gamma = \epsilon\bar{\gamma}$. Ignoring the terms associated with ϵ^2, Equation (2.9) can be written as [70]

$$\ddot{\theta}(t) + 2\epsilon\bar{\beta}\omega_n\dot{\theta}(t) + \left[1 - \epsilon\bar{q}\left(\frac{\Omega}{\omega_n}\right)^2 \cos\Omega t\right]\omega_n^2\theta(t) + \epsilon\bar{\gamma}\omega_n^2\theta^3(t) = 0 \tag{2.10}$$

Equation (2.10) represents a general form of a parametrically excited oscillator with cubic nonlinear stiffness and viscous damping. It has been shown that the condition for a stable 2:1 subharmonic oscillation to exist is [71]

$$\mu \leq 1, \quad \mu = \frac{\beta}{q} \tag{2.11}$$

which indicates that the maximum level of total viscous damping allowed for a stable response is $C_{\max} = 2\omega_n M\lambda q$. For a device with a certain level of intrinsic damping, C_m, (2.11) defines the minimum level of excitation required as $q_{\min} = C_m/(2\omega_n M\lambda)$.

Considering the case of near-resonant excitation, i.e.

$$\Omega = 2\omega_n + \epsilon\sigma\omega_n \tag{2.12}$$

where σ is the so-called detuning parameter and using the multi-scale method, the system response in steady state can be approximately obtained as [70]

$$\theta(t) \approx a\left\{\cos\left[\frac{1}{2}(\Omega t - \psi)\right] + \frac{1}{24}\Gamma\cos\left[\frac{3}{2}(\Omega t - \psi)\right] - \frac{1}{4}q\left(\frac{\Omega}{2\omega_n}\right)^2\cos\left[\frac{3}{2}(\Omega t - \frac{1}{3}\psi)\right]\right\} \tag{2.13}$$

where $\Gamma \equiv \frac{3}{4}\gamma a^2$. Mathematically, there are two solution sets: Set 1 (a_+^2, ψ_+) and Set

2 (a_-^2, ψ_-), where

$$a_\pm^2 = \frac{4\epsilon}{3\gamma}\left(\sigma \pm \sqrt{S}\right), \quad \tan\psi_\pm = \frac{2\beta}{\pm\epsilon\sqrt{(}S)}, \quad \sqrt{S} = \frac{2q}{\epsilon}\sqrt{\left(1+\frac{\epsilon\sigma}{2}\right)^4 - \mu^2} \tag{2.14}$$

It is clear that the necessary condition for the above solutions to exist is $S \geq 0$, i.e. $1 + \frac{\epsilon\sigma}{2} \geq \sqrt{\mu}$. Such condition renders, mathematically, two conditions, one of which is

$$\epsilon\sigma \geq \nu_0, \quad \nu_0 = -2(1-\sqrt{\mu}) \tag{2.15}$$

and the other, $\epsilon\sigma \leq -2(1-\sqrt{\mu})$, which corresponds to excitations with negative frequencies; it is thus ignored in this study.

Using the results in [70], it can be shown that the solutions indicated in (2.14) are unstable under the following condition

$$\frac{3}{4}\gamma a_\pm^2\left(\frac{3}{4}\gamma a_\pm^2 - \sigma\right) < 0 \tag{2.16}$$

More specifically, for a system with softening type nonlinearity ($\gamma < 0$), e.g. for the case of a pendulum, $\gamma = -\frac{1}{6}$, the above condition indicates that the solution Set 1 (a_+^2, ψ_+) is unstable whereas solution Set 2 (a_-^2, ψ_-) is stable. For the case of hardening type nonlinearity, reverse conclusion can be obtained. Only the stable solution is physically observable. Particularly, for the softening type, as $a^2 \geq 0$, it is necessary that $\sigma \leq \pm\sqrt{S}$ for a solution to exist. Ignoring the unstable solution as well as the terms with orders higher than ϵ, such condition, in combination with (2.15), defines the bandwidth of the system to be

$$\nu_0 \leq \epsilon\sigma \leq \nu, \quad \nu = \frac{1-\mu^2}{\sqrt{1-\mu^2}/(2q) - 1} \tag{2.17}$$

Note that for the unstable solution, a_+^2 defines another critical frequency and to the

first order approximation with regard to ϵ, that is

$$\nu = -\frac{1-\mu^2}{\sqrt{1-\mu^2}/(2q)+1} \tag{2.18}$$

For low-level excitations, $\nu > \nu_1 > \nu_0$. When $\nu_1 < \epsilon\sigma < \nu$, the system will bound to have a nonzero response, whereas, when $\nu_0 < \epsilon\sigma < \nu_1$, whether the system has a nonzero response depends on the initial condition of the system [71]. Thus the system bandwidth is at least $\nu - \nu_1 \approx 4q\sqrt{1-\mu^2}$, with the possibility of expanding to $\nu - \nu_0 \approx 2(1-\sqrt{\mu}) - 2q\sqrt{1-\mu^2}$. Clearly, lower damping level corresponds to larger bandwidth, which is opposite to the case of linear oscillator where a higher damping level enlarges bandwidth. It is noted, however, (2.17) may overestimate the bandwidth of the system, especially for systems with very low damping levels as the approximate solution is only valid in the vicinity of resonance, i.e. $\epsilon\sigma << 1$.

2.2.2 Power Output

Mechanical energy from a vibrating source is harvested through the damping mechanism of the system. The total instantaneous power dissipated is

$$p_1(t) = C\left[L\dot{\theta}(t)\right]^2 \tag{2.19}$$

Using the approximate analytical expression of the system response (2.13) and the definition of μ in (2.11), the average power P_1 over one period can be written approximately as

$$P_1 = k\mu\alpha^2\left(q\sqrt{\alpha^4-\mu^2} - \alpha + 1\right)\Lambda \tag{2.20}$$

where $\alpha = 1 + \epsilon\sigma/2$, $k = 8C_{\max}gL/\lambda$ and

$$\Lambda = 1 + \left(\frac{1}{8}\Gamma\right)^2 + \left(\frac{3}{4}q\right)^2\alpha^4 + \frac{1}{32}\Gamma q\sqrt{\alpha^4-\mu^2} \tag{2.21}$$

2.2.2.1 Optimal damping level

For the case of low-level and near-resonant excitation ($q, (1-\alpha) << 1$), the average total power, P_1 can be simplified as

$$P_1 = k\mu\left(q\sqrt{1-\mu^2} + 1 - \alpha\right) \tag{2.22}$$

There exists an optimal value of the normalized damping coefficient, μ, such that the dissipated power is maximized. Differentiating P_1 with respect to μ, to the first order approximation, the optimal damping can be obtained as

$$\mu_{opt} = \frac{1}{\sqrt{2}}\sqrt{1 - \delta^2 + \delta\sqrt{\delta^2+2}}, \quad \delta = \frac{1-\alpha}{2q} \tag{2.23}$$

The maximal power, P_1 can be written as

$$P_{1\max} = kq\left(1 + 2\sqrt{2}\delta\right) \tag{2.24}$$

Using (2.23) and (2.24), the maximum power can be written as

$$P_{1\max} = \frac{1}{2}k(1-\alpha)\left(\frac{\sqrt{1-\mu_{opt}^2}}{2\mu_{opt}^2 - 1} + \sqrt{2}\right) \tag{2.25}$$

At exact resonance, i.e. $\alpha = 1$, $\mu_{opt} = 1/\sqrt{2}$, the maximum power becomes $P_{1\max} = \frac{1}{2}kq$.

2.2.2.2 Power delivered to electrical load

The optimal power (P_1) discussed previously represents the maximum capacity of the device to dissipate energy from the source, which includes the power dissipated by the

mechanical damping, power dissipated by the internal resistance of the windings and the electrical load. Thus, the actual power delivered to the load, P_L, can be written as

$$P_L = \frac{R_L}{r_w + R_L} \frac{C_e}{C_m + C_e} P_1 \tag{2.26}$$

Due to the intrinsic damping of the device, C_m and the condition in (2.11), there is an upper limit of the allowable level of electrical damping, i.e. $C_e < C_{Me}$, where $C_{Me} = C_{\max} - C_m$. Therefore, the maximum electrical load (with minimal resistance) the device can power is

$$R_{L,\min} = \frac{K_{Ce}}{C_{le}} - r_w, \quad C_{le} = \min\{C_{Me}, C_{e,\max}\} \tag{2.27}$$

In an ideal case where there is no internal loss, i.e. $r_w = 0$ and $C_m = 0$, the optimal damping level in (2.23) corresponds to the optimal electrical load that maximizes the electrical power output, $P_L = P_1$. In reality, as $r_w, C_m \neq 0$, $P_L < P_1$, the damping level, denoted as μ_{optR}, that maximizes the electrical power, P_L is generally lower than μ_{optR} in (15). However, an analytical expression of the optimal damping level, μ_{optR} cannot be obtained.

Two cases should be noted where the optimal condition cannot be achieved: Case 1 where the internal resistance, r_w, is such that $r_w > \frac{K_{Ce}}{C_{optR} - C_m}$ where C_{optR} is the optimal total damping coefficient and Case 2 where $C_m > C_{optR}$. In both cases, the power delivered to the electrical load monotonically increases as R_L decreases and it reaches the maximum value when $R_L = R_{L,\min}$. In general, if $C_m < C_{optR} < C_{Me} < C_{e,\max}$, the optimal conditions can be satisfied. As C_{Me} is proportional to the excitation level, i.e. A_e or q, devices with low intrinsic damping and low internal resistance are particularly desired for strong excitations so that the capacity of the device can be fully achieved.

2.2.3 Electromotive Forces and Voltages

In this section, the analytical approximations of the electromotive force of each winding and the voltage across the load are presented.

Equation (2.13) can be rewritten as

$$\theta(t) = a\cos\left(\omega_n t - \frac{1}{2}\psi\right) + a_3\cos\left(3\omega_n t - \psi_3\right) \tag{2.28}$$

where

$$\begin{aligned} a_3 &= \frac{aq}{12}\sqrt{4 + 5\mu^2 + \chi\left(\chi - 4\sqrt{\alpha^4 - \mu^2}\right)} \\ \tan\psi_3 &= \frac{\left(\chi + \sqrt{\alpha^4 - \mu^2}\right)\sin\left(\frac{3}{2}\psi\right) + 3\alpha^2\sin\frac{\psi}{2}}{\left(\chi + \sqrt{\alpha^4 - \mu^2}\right)\cos\left(\frac{3}{2}\psi\right) + 3\alpha^2\cos\frac{\psi}{2}} \\ \chi &= \frac{1-\alpha}{q} \end{aligned} \tag{2.29}$$

In this study, low-level vibrations was of interest, thus, it was assumed that $a < 1$. Using fact that $\sin\theta = \theta - \theta^3/6 + O(\theta^5)$ and $\cos\theta = 1 - \theta^2/2 + \theta^4/24 + O(\theta^6)$, (2.2) can be approximately written as

$$\begin{aligned} e_A =& -K_e\omega_n\left\{\left[G_1\sin\left(\omega_n t - \frac{\psi}{2}\right) + G_3\sin\left(\omega_n t - \nu_3\right)\right]\sin\phi\right. \\ &\left. + \left[G_2\sin\left(2\omega_n t - \psi\right) + G_4\sin\left(4\omega_n t - \nu_4\right)\right]\cos\phi\right\} \\ e_B =& -K_e\omega_n\left\{\left[G_1\sin\left(\omega_n t - \frac{\psi}{2}\right) + G_3\sin\left(\omega_n t - \nu_3\right)\right]\cos\phi\right. \\ &\left. + \left[G_2\sin\left(2\omega_n t - \psi\right) + G_4\sin\left(4\omega_n t - \nu_4\right)\right]\sin\phi\right\} \end{aligned} \tag{2.30}$$

where

$$G_1 = a\left(2 - \frac{a^2}{4}\right), \quad G_2 = a^2\left(1 - \frac{a^2}{12}\right) \tag{2.31}$$

and

$$G_3 = \sqrt{g_{31}^2 + g_{32}^2 + 2g_{31}g_{32}\cos(\psi_3 - 3\psi/2)}, \quad G_4 = \sqrt{g_{41}^2 + g_{42}^2 + 2g_{41}g_{42}\cos(\psi_3 - 3\psi/2)}$$
$$\tan\nu_3 = \frac{g_{31}\sin\psi_3 + g_{32}\sin(3\psi/2)}{g_{31}\cos\psi_3 + g_{32}\cos(3\psi/2)}, \quad \tan\nu_4 = \frac{g_{41}\sin 2\psi + g_{42}\sin(\psi_3 + \psi/2)}{g_{41}\cos 2\psi + g_{42}\cos(\psi_3 + \psi/2)}$$
$$g_{31} = 6a_3\left(1 - \frac{a^2}{4}\right), \quad g_{32} = -\frac{a^3}{4}, \quad g_{41} = -\frac{a^4}{24}, \quad g_{42} = aa_3\left(4 - \frac{5}{8}a^2\right) \tag{2.32}$$

In the cases where $a << 1$, to the first approximation, $G_1 = 2a$ and $G_2 = G_3 = G_4 = 0$, the electromotive forces are dominated by the oscillation with the natural frequency of the system.

Using (2.30), (2.31), and (2.32), the effective values of the electromotive forces can be determined approximately as

$$\begin{aligned} E_A &= \frac{1}{\sqrt{2}}K_e\omega_n H_{gA}, \quad H_{gA}^2 = \left(G_1^2 + G_3^2\right)\sin^2\phi + \left(G_2^2 + G_4^2\right)\cos^2\phi \\ E_B &= \frac{1}{\sqrt{2}}K_e\omega_n H_{gB}, \quad H_{gB}^2 = \left(G_1^2 + G_3^2\right)\cos^2\phi + \left(G_2^2 + G_4^2\right)\sin^2\phi \end{aligned} \tag{2.33}$$

Note that

$$H_{gA}^2 + H_{gB}^2 = G_1^2 + G_2^2 + G_3^2 + G_4^2 = H_g^2 \tag{2.34}$$

which indicates that total energy harvested via the two windings is invariant with the initial orientation of the magnet, i.e. ϕ.

For the case of $\phi = 45^o$, the two windings are symmetric about the magnetic axis. Thus,

$$E_A = E_B = \frac{1}{\sqrt{2}}K_e\omega_n H_g \tag{2.35}$$

If the third harmonic is so small that $a_3 << a$, it can be ignored and thus, the effective values can be simplified as

$$E_A = E_B = K_e\omega_n a \tag{2.36}$$

The voltages across the windings can be obtained as

$$V_A = V_B = K_e \omega_n a \frac{R_L}{r_w + R_L} \tag{2.37}$$

2.3 Experiments

2.3.1 Prototype Device

A prototype device was fabricated based on the design described previously (Figures 1 and 2). The pendulum consisted of a plastic arm with mass measured at 5.6 g and copper screws as the tip mass, measured at $M_b = 9.9$ g. A cylindrical rare-earth magnet with a mass of 0.0241 kg, a radius of $\rho_R = 6.35$ mm and a length of $l_R = 2.54$ cm was used as the rotor of the generator. The volume of the device was approximately 13 cm^3 (roughly 0.8 $in.^3$).

Considering the mass and the overhanging portion of the pendulum arm, the equivalent length and mass of the pendulum were found to be 5.95 cm and 12.9 g, respectively. The moment inertia of the device was calculated to be $J = \frac{1}{2} M_R^2 \rho_R^2 = 4.86 \times 10^{-7}$ Kg-m^2 and $\lambda = 1.011$. The natural frequency of the device was calculated to be 2.04 Hz.

The magnet was diametrically magnetized with the maximum surface magnetic flux density measured at 0.549 T. The distribution of the magnetic flux density in both the radial and perimetrical directions was measured with a DC Magnetometer (AlphaLab Inc., measurement range: $\pm 19,999$ gauss $\pm 2\%$ in $30\tilde{1}10$ ^{o}F). The results are shown in Figure 2.3. It is seen that the magnetic flux density is inversely proportional to the third power of the distance away from the surface, whereas in the perimetrical direction, it fluctuates in a pattern close to a sinusoidal function. Such measurements confirmed Assumption 2.

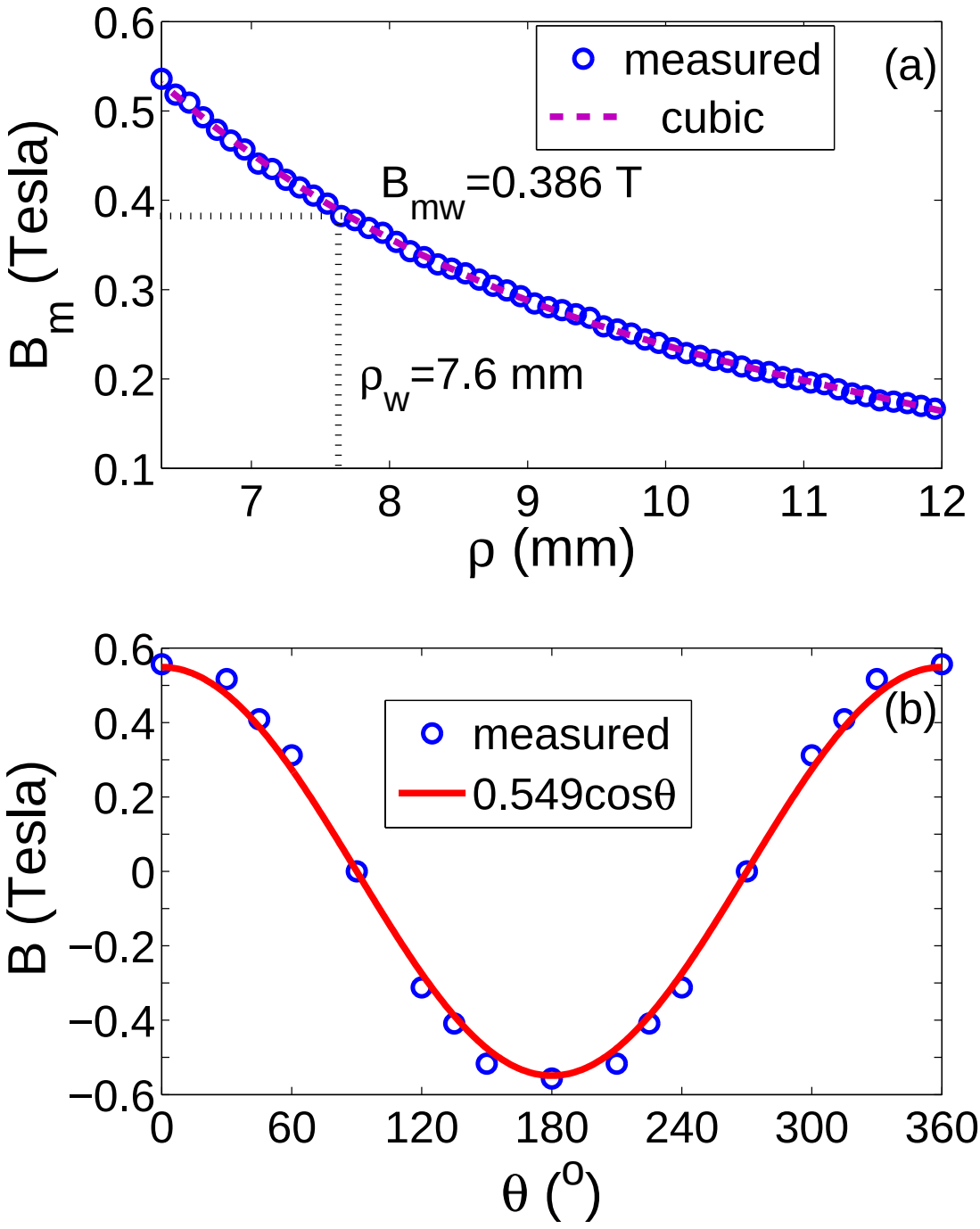

Figure 2.3: Magnetic flux density

The two windings were fabricated using AWG #44 copper wire. Each winding had $W = 2400$ turns and the resistances were measured at 1380 ohms and 1420 ohms, respectively. The winding coefficient was calculated to be $K_w = 0.758$ [72, 73]. The windings covered the entire surface of the magnet and the centroid of the windings in the radial direction was measured at $\rho_w = 7.6$ mm from the magnet surface, giving the equivalent magnetic flux density of $B_{mw} = 0.386$ T. The coefficient, K_e, defined in (2.2) was then obtained as $K_e = 0.1328$ T-m^2.

2.3.2 Experiment Setup

Figure 2.4 shows the experiment setup. The equipment and instruments included a shaker (Model LW-126-13, Labworks Inc.), a video camera (Model DCR-TRV30 NTSC, Sony Inc.) for recording the swinging motion of the pendulum against an angular scale mounted on the device, a digital phosphor oscilloscope (Model DPO3040, Tektronix) for measuring the output voltage, and an electrical load circuit. In experiments, initial orientation of the magnet in the device was fixed 45^o.

2.3.3 Results

2.3.3.1 Device characterization

Free vibration test was first performed to identify the dynamic properties of the device. The natural frequency of the device was identified to be 2.03 Hz; the viscous damping ratio was identified to be $\xi = 0.55\%$.

2.3.3.2 Device performance

The frequency response of the device was first investigated. The electrical load was fixed at 15 kohm and the excitation amplitude was fixed at $0.14g$. The results are sum-

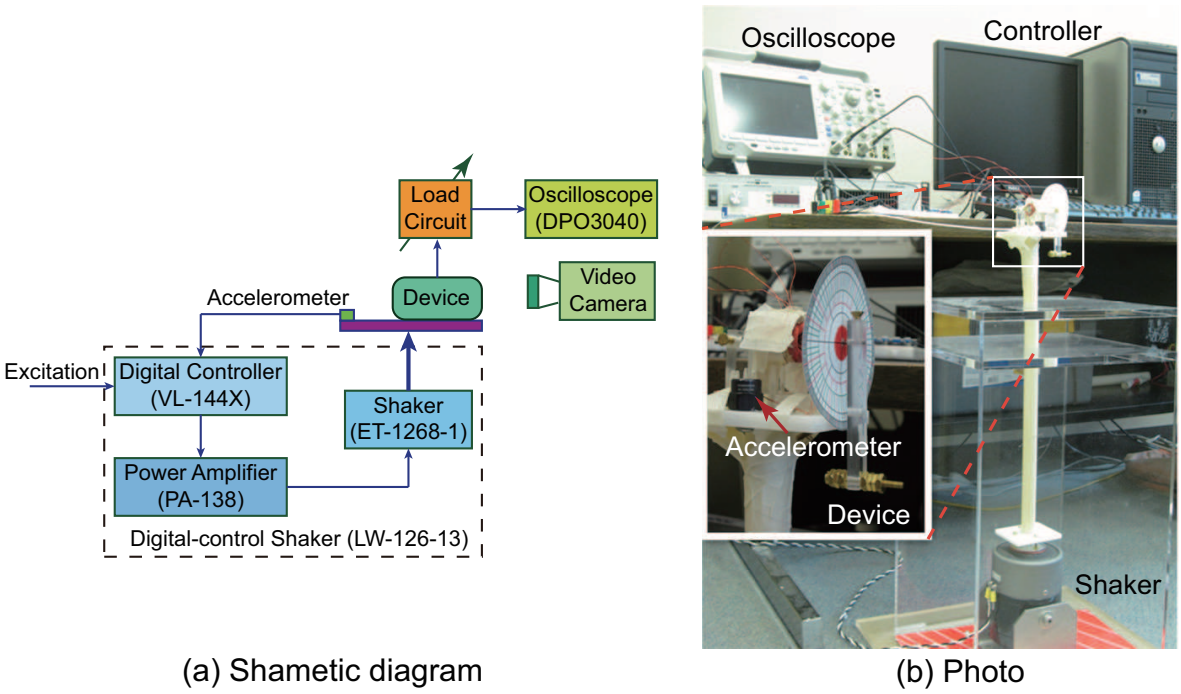

Figure 2.4: Experiment setup

marized in Figure 2.5. The effective values of the power delivered to the electrical load, PL, were calculated based on the measured waveform of the voltage across the electrical load of each winding. The results from numerical simulation using MATLAB© (solver ODE45) and theoretical approximations are both shown for comparison. The results from the experiments are in excellent agreement with those from numerical simulation. While the simulation demonstrated that the cut-off frequency was approximately 2.2 Hz with the effective value of electrical power being approximately 1.2 mW, due to the limitation on the capacity of the shaker, frequencies lower than 3 Hz could not be achieved experimentally. Theoretical approximations were quite consistent with simulation and experimental results when the frequency deviation, $\epsilon\sigma$, was small, i.e., smaller than 0.4. For $\epsilon\sigma > 0.4$, larger errors were observed. Such increasing inconsistency may have been due to the violation of the assumption of small $\epsilon\sigma$ that was used in the theoretical approximations. If the system bandwidth is evaluated using half power bandwidth, the results suggest that the bandwidth of the device is approximately 70% the natural

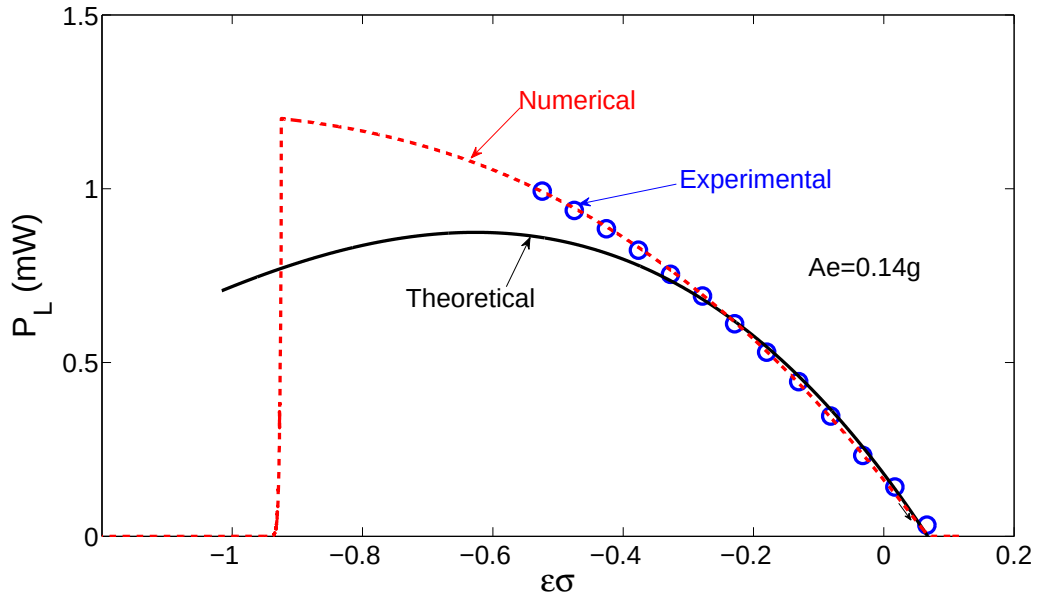

Figure 2.5: Frequency response of the device ($A_e = 0.14g$ and $R_L = 15$ kilohms). Markers: Experimental; Dashed line: Numerically calculated; Solid line: Theoretical

frequency of the device.

The electrical load carrying capacity of the device was then evaluated. Excitations were fixed at 4 Hz, i.e. $\alpha \approx 0.985$. Three levels of excitations, i.e. $0.08g$, $0.14g$, and $0.18g$, were considered. The relationship between the total dissipated power, P_1, and the normalized damping ratio, μ is shown in Figure 2.6. The results from both numerical simulations and theoretical approximation are shown for comparison. The optimal damping level for the three excitations - indicated by the triangular marks - were found to be 0.82, 0.78, and 0.76, respectively, corresponding to the optimal power of 0.65mW, 1.40mW and 2.10mW, respectively. These values were consistent with the theoretical prediction, expressed in (2.25). It is seen that all three results are in good agreement. While the experimental results closely followed those from simulations, theoretical approximations overestimated the power. The relationship between the power delivered to the electrical load, P_L, and the electrical load R_L is shown in Figure 2.7. Due to symmetry, the results of only one of the windings are shown. Once again,

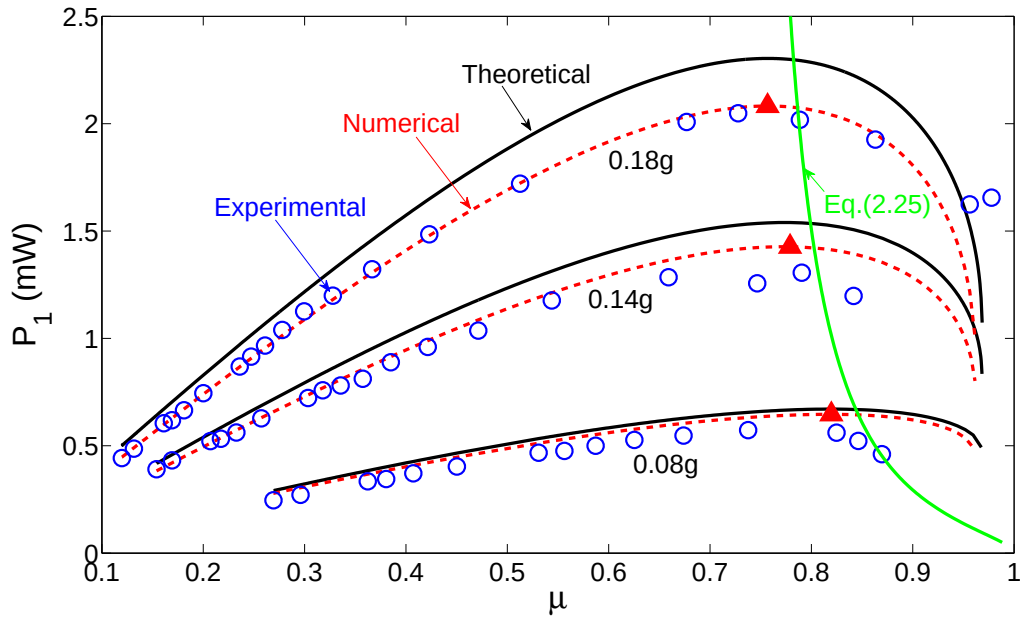

Figure 2.6: Effect of total damping level. Markers: Experimental; Dashed lines: Numerically calculated; Solid lines: Theoretical

the results of theoretical, numerical and experimental studies were consistent, while the theoretical approximations overestimated the power. The optimal electrical loads for the three cases (triangular marks) were found to be 4.10 $k\Omega$, 2.15 $k\Omega$, and 1.80 $k\Omega$, respectively, which corresponding to an optimal electrical power of 0.32 mW, 0.62 mW, and 0.78 mW, respectively. It was observed that a higher excitation level not only increased the power output, it also increased the load carrying capacity of the device.

The effective values of the voltage generated are shown in Figure 2.8. The effective values were calculated using the measured wave forms of the voltages. As the results of the two windings were almost identical, the results of only one winding are shown here. The results from the the numerical simulations were in excellent agreement with those from the experimental measurements. The theoretical approximations, obtained from (2.36) demonstrated the same trend, however, the voltages were overestimated. Such overestimation, as observed in the figures shown previously, may have been due to

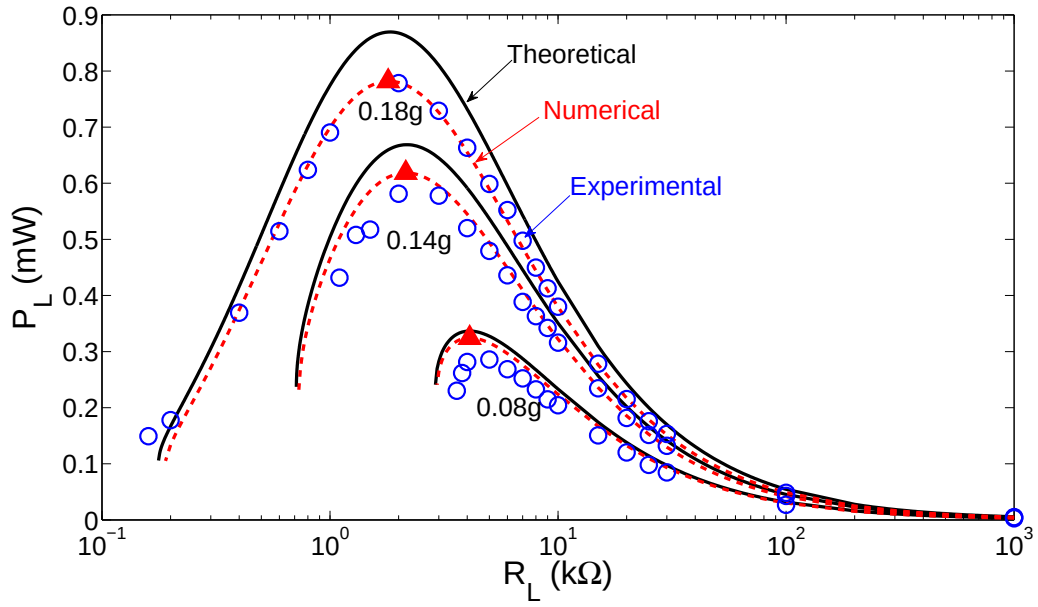

Figure 2.7: Power delivered to the electrical load. Markers: Experimental; Dashed lines: Numerically calculated; Solid lines: Theoretical

the modeling errors introduced in the simplifications of the non-linearity of the system as well as the errors in the multi-scale method that was used to obtain analytically the system response. It is interesting to note that when the electrical load was small, i.e. R_L was far larger than the load capacity of the device, $R_{L\,\min}$, the voltage-current relationship was almost linear. Decreasing load resistance increased the current in the circuit. The device behaved as an electrical voltage source. For large electrical loads, especially those close to $R_{L\,\min}$, the current varied with voltage in a highly non-linear fashion. Such non-linear behavior may have been due to the fact that in the vicinity of the system load capacity, the system response becomes very sensitive to the load resistance - a small increase in the electrical load (or a small decrease in R_L) would result in a significant reduction in the amplitude of the system response, resulting in a dramatic voltage drop, thus the current becomes smaller even when the resistance is lower.

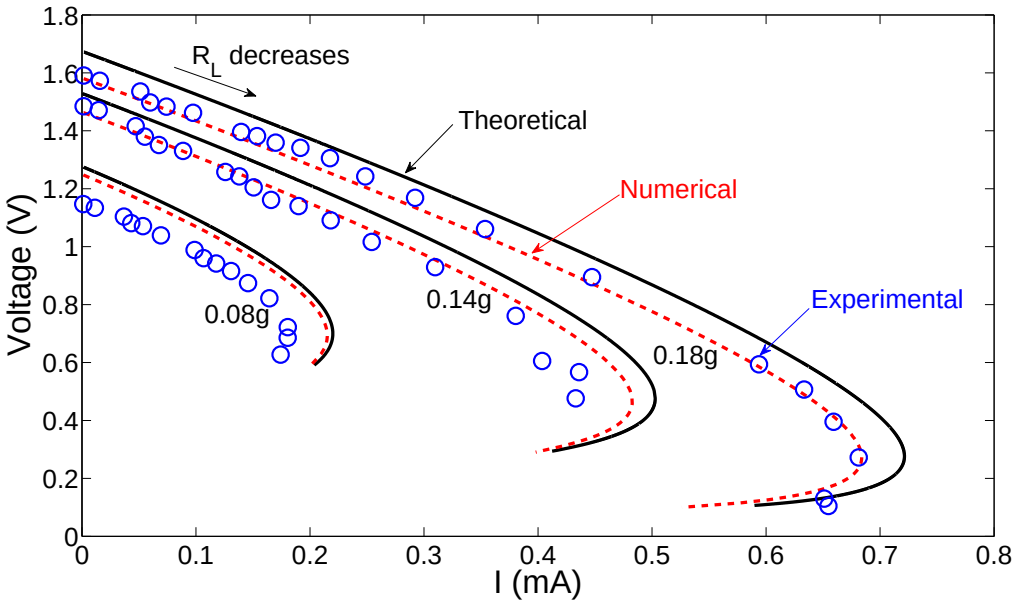

Figure 2.8: Effective value of voltages generated. Markers: Experimental; Dashed lines: Numerically calculated; Solid lines: Theoretical

2.3.4 Comparison with Linear Harvesters

In this section, the performance of the proposed device is compared with that of a conventional energy harvester based on linear resonance. A linear device with identical natural frequency (2.03 Hz) and damping ratio (0.55%) is considered. It is assumed that the magnetic and electrical properties of the linear device are the same as the those of proposed device. Figure 2.9 shows the comparison of the frequency responses of the two devices when connected to an electrical load of 15 kohms. It can be seen that the peak value of the linear device is much higher than that of the proposed device, however, the bandwidth of the linear device is significantly smaller. The half-power bandwidth of the linear device is a about 2% the natural frequency, while that of the proposed device is about 70%. It should be noted that to achieve the peak value of the linear device shown in Figure 2.9 is difficult if not impossible for at least two reasons. Firstly, due to the constraint on the size of the device and the limitations of material

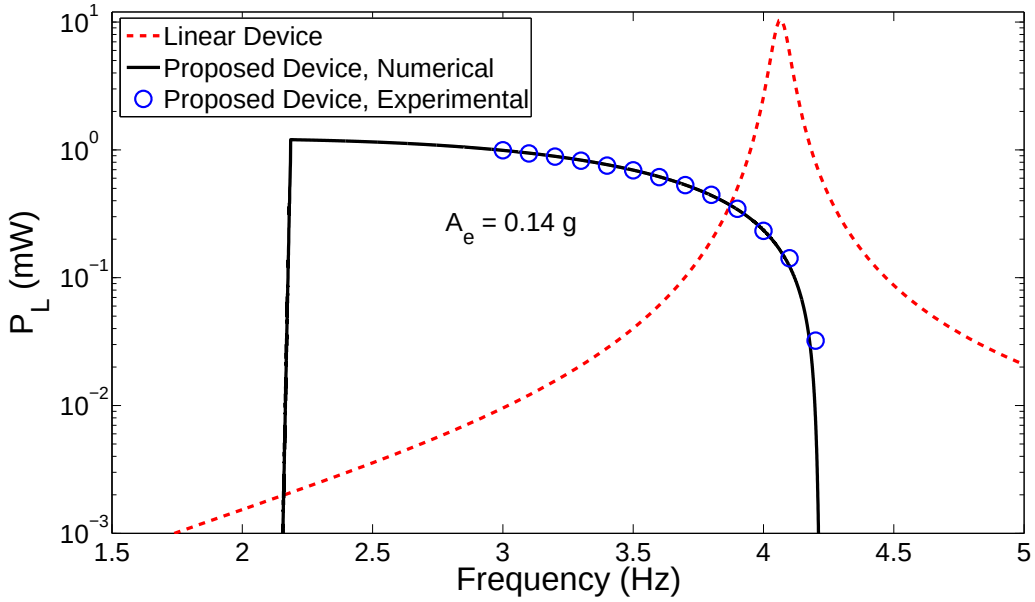

Figure 2.9: Frequency responses of the proposed device and a linear device

property, it is very difficult to achieve low resonant frequency (especially those below 10 Hz) in a linear device, and secondly, even if a device with a low resonant frequency (e.g. 4 Hz) may be realized, the amplitude of the internal vibration of the device at resonance would be so large that the device behavior would already be in the non-linear regime. For the case considered, at a resonant frequency of 4 Hz, the amplitude of the device would be on the order of 100 mm, which would be far beyond the limit for linear behavior considering the length scale of the device (e.g. 10 mm).

2.4 Concluding Remarks

In this chapter, use of parametric resonance to enhance vibration-based energy harvesting, especially at low frequencies was investigated. A device with a pendulum as the moving part and electromagnetic induction as the energy conversion mechanism was proposed and fabricated. Such rigid-body device architecture eliminated the

requirement of material deformation. Low working frequencies - around 4 Hz - were achieved. The behavior and performance the device were studied theoretically based on the multi-scale method and numerically using the Matlab© (solver ODE45). Compared with experimental verification, the results of the numerical simulations were found to be more accurate, while the theoretical analysis in general slightly overestimated the power in the cases considered.

In contrast to the conventional linear energy harvesting method, where power is almost inversely proportional to the damping level, in the proposed method, there exists an optimal damping level (or load resistance) under which the power output is the maximal. Also, the bandwidth of the proposed device is almost inversely proportional to the damping level as opposed to the linear method, where the bandwidth reduces significantly for lower damping levels. Thus, for applications involving low electrical load, the proposed energy harvesting method may offer better performance than the linear method.

It should be noted that in this study, focus was placed upon the investigation of the fundamental aspects of the energy harvesting method based on parametric resonance. The electrical load was simplified as a resistor. In certain energy harvesting circuits, the characteristics of the electrical load may be more complicated. The performance of device under such conditions require further in-depth investigation. However, for applications with simple circuits, such as the RLC circuits, the results obtained may still be valid due to the significant frequency mismatch (e.g. 4 Hz versus 1 kHz).

Chapter 3

FULL POTENTIAL OF NONLINEAR ENERGY HARVESTING WITHIN POTENTIAL WELL - GLOBAL RESONANCE

There has recently been a surge of interest in harvesting energy from vibrations with nonlinear oscillators. This increasing attention is primarily driven by the motivation of taking advantage of the unique features of nonlinear systems for improved performance [9, 26, 27, 30, 74]. The most investigated and attractive feature is the phenomenon of bifurcation. This unique attribute gives rise to orbits with high energy levels under conditions where only low energy levels exist in linear systems. As the majority of existing schemes use the damping mechanism to harvest energy, generating a large response is advantageous. Seeking ways to increase the device response is the dominant trend reported in the literature. In this chapter, we show that, while larger response is beneficial in linear methods, relying only on increasing the device response with nonlinear approaches can be misleading. In linear devices, the optimal performance occurs at resonance, where the response is also a maximum because the condition simultaneously leads to the largest response with a maximum amount of energy dissipation. In nonlinear systems, the conditions are different, particularly in the bifurcation zone. We show that in the high energy orbits, a larger response does not always result in more energy being harvested. In fact, the amount of energy harvested from a large response can

be orders of magnitude lower than that from a lower response. We demonstrate that the condition for the highest energy dissipation (harvesting) is essentially a generalized resonance condition, which relies on the frequency match between the system and the forcing function. In contrast to linear systems, a nonlinear potential well supports a range of fundamental frequencies, which are strongly correlated with the amplitude of the response. Because of the direct correlation between damping and the response amplitude, meeting the resonance condition can be facilitated by variable damping in a nonlinear system. This chapter also shows that parameterization of the excitation [69, 70, 75] provides a cross-frequency energy transfer, which extends the resonance condition to multiple zones of the excitation frequency, dramatically widening the working frequency zone of the system. These unique features are critical in realizing the full potential of nonlinear energy harvesting, and yet, have largely remained unexplored.

3.1 Theoretical Analysis

3.1.1 Global Resonance Condition

Consider a nonlinear system subjected to a periodic excitation. The governing equation can be written as:

$$\ddot{x} + \gamma\dot{x} + k(x) = f(t)g(x), \tag{3.1}$$

where x denotes the displacement, γ is the damping coefficient, $f(t) = f(t + T_f)$ is the excitation with a fundamental period of $T_f = 2\pi/\omega_f$, and $g(x)$ denotes the self-modulation function (parametric excitation). In this study, it was assumed that energy was harvested through damping. Thus, total damping of the system included the intrinsic damping of the system and the equivalent electrical damping. The restoring force, $k(x) = \partial U(x)/\partial x$, where $U(x)$ is the potential well function of the system, determines the amplitude-dependent fundamental frequency of the undisturbed

response, ω_0. Depending on the amplitude, the fundamental frequency supported by the potential well is within the range $\omega_{min} \leq \omega_0 \leq \omega_{max}$. For a periodic excitation with a frequency content of $\omega_f(\geq \omega_{\min}), 2\omega_f, 3\omega_f \cdots$, it is possible to find an ω_0 such that $\omega_f/\omega_0 = n$, where n is a positive integer. The periodic response in the steady-state (if it exists) can be written as: $x(t) = \sum_{i=1}^{\infty} A_{ri} \cos(i\omega_0 t - \phi_i)$. Using $g(x) = g(0)+g'(0)x+g''(0)x^2/2!+\cdots$, it can be shown that if $g^{(n-1)}(0) \neq 0$ or $g^{(n+1)}(0) \neq 0$, the modulated forcing function contains the same fundamental frequency as the response. Thus, $F(t) = f(t)g(x) = \sum_{i=1}^{\infty} A_{fi} \cos(i\omega_0 t - \phi_{fi})$. The average power dissipation per cycle is $P_d = \frac{1}{2}\gamma \sum_{i=1}^{\infty} (iA_{ri}\omega_0)^2$, which must be equal to the input power of the excitation: $P_f = \frac{1}{T}\int_0^T f(t)g(x)\dot{x}dt = \frac{1}{2}\sum_{i=1}^{\infty} i\omega_0 A_{fi}A_{ri}\sin(\phi_i - \phi_{fi})$, where $T = 2\pi/\omega_0$. The energy is dissipated and compensated in multiple frequencies. The efficiency of the external work is indicated by: $\eta_i = \sin(\phi_i - \phi_{fi}) \leq 1$. At the maximum efficiency, $\eta_i = 1$, the velocity and the forcing function are in phase for all participating frequencies. Here, a global resonance condition is defined such that the instantaneous power of the excitation is always non-negative, $p_f(t) = F(t)\dot{x} \geq 0$. The efficiency of the external work $\eta = \frac{\int_0^T p_f(t)dt}{\int_0^T |p_f(t)|dt} = 1$ which indicates $\eta_i = 1$. Under the global resonance condition, thus, $\phi_i - \phi_{fi} = \frac{\pi}{2}$. The modulated forcing function can be expressed in the form of vector product as $F(t) = -\mathbf{y}^T\mathbf{A_f} = -\mathbf{A_f}^T\mathbf{y}$, where $\mathbf{A_f} = \{A_{f1}, A_{f2}, \cdots A_{fn} \cdots\}^T$ and $\mathbf{y} = \{y_1, y_2, \cdots y_n \cdots\}^T$, and $y_i = \sin(i\omega_0 t - \phi_i), i = 1, 2, \cdots$. The velocity of the response can be written as $\dot{x} = -\mathbf{A_r}^T\mathbf{y}$ where $\mathbf{A_r} = \{\omega_0 A_{r1}, 2\omega_0 A_{r2}, \cdots n\omega_0 A_{rn} \cdots\}^T$. The instantaneous power $p_f(t) = \mathbf{y}^T\mathbf{A_f}\mathbf{A_r}^T\mathbf{y}$ which can be written in quadratic form as: $p_f(t) = \mathbf{y}^T\mathbf{A}\mathbf{y}$, where $\mathbf{A}$ is a matrix with elements $a_{ii} = iA_{fi}A_{ri}\omega_0$ and $a_{ij} = \omega_0(jA_{fi}A_{rj} + iA_{fj}A_{ri})/2, i \neq j$. A non-negative power, $p_f(t) \geq 0$, requires $\mathbf{A}$ to be positive-semi-definite. Thus, $a_{ii}a_{jj} \geq a_{ij}^2$ [76]. This inequality, combined with the energy conservation required (i.e. $P_d = P_f$), gives $A_{fi}/(iA_{ri}) = \gamma$ and consequently, $F(t) = \gamma\dot{x}$. Under this condition, Eq. (3.1) is equivalent to the following simultaneous

equations:

$$\ddot{x} + k(x) = 0 \tag{3.2a}$$

$$\gamma\dot{x} = f(t)g(x). \tag{3.2b}$$

The response is the same as an undisturbed response and belongs to the high-energy branch.

3.1.2 Comparison with Sub- and Super-harmonic Oscillations

In a general case, the undisturbed response has the frequencies $\omega_0, 2\omega_0, 3\omega_0 \cdots$. Eq. (3.2b) is the condition that is necessary for a global multi-frequency resonance that requires matching of all of the frequencies. For a linear system, this condition reduces to the linear resonance. For a nonlinear system, the frequency content of an undisturbed response is generally amplitude dependent. As such, damping plays an important role in tuning the system frequencies by changing the amplitude. Conversely, the interactions between the properly designed modulation, $g(x)$, and the excitation facilitates a frequency match by generating frequencies that do not exist in the original excitation, but are necessary for resonance. Thus, resonance can be achieved in the frequency zones that are unmatched with the system, such as the subharmonic oscillation zone, $\omega_f = n\omega_0$, where $n > 1$ and is an integer. Without modulation, $g(x) = 1$, subharmonic oscillations with a large response can occur. However, owing to the frequency mismatch, the energy dissipation and compensation (i.e. the work done by the excitation) have different frequencies, resulting in low performance of the energy harvesting. In the case of a super harmonic oscillation, where $\omega_f = \frac{1}{n}\omega_0$, a periodic steady-state response requires $\omega_f = \frac{\omega_0}{n}$ as the fundamental frequency of the response. Thus, the response contains the frequencies $\frac{1}{n}\omega_0, \frac{2}{n}\omega_0, \cdots \frac{n-1}{n}\omega_0, \omega_0, \frac{n+1}{n}\omega_0 \cdots$. The frequency content of the undisturbed response is $\omega_0, 2\omega_0, \cdots$. The resonance condition in Eq. (3.2b) cannot

be satisfied because of the frequency mismatch. Tuning the damping and modulation of the excitation, $g(x)$, may enable a super harmonic oscillation with a large response. However, the unwanted frequencies in the response cannot be eliminated to satisfy the resonance requirement. In the special case of a linear oscillator with $k(x) = \omega_0^2 x$ and $g(x) = 1$, the natural frequency of the linear system is fixed and Eq. (3.2b) reduces to the linear resonance condition of $\omega_f = \omega_0$. The response that satisfies this condition automatically satisfies Eq. (3.2a). Thus, Eq. (3.2b) becomes the condition for linear resonance. This linear resonance does not depend on damping. A linear device can be at resonance under different damping levels, all of which maximize the efficiency of the energy dissipation, i.e. $\eta = 1$. Among such damping levels, there is an optimal level that provides the maximum electrical power. In the nonlinear case, damping is part of the resonance condition. Thus, maximizing the total dissipated energy by driving the system into resonance leads to the maximum electrical power that can be harvested.

3.2 Demonstration

3.2.1 Device and Experiment Setup

In this investigation, a prototype was designed and fabricated based on its potential for application in powering wireless sensors deployed on a structure for long-term autonomous structural monitoring [77]. With supporting circuitry, the device could be used as a direct power supply or a charging unit for the battery in a sensor. To maximize the efficiency, the device was designed such that the linear natural frequency fell within the frequency range of the normal ambient structural vibrations (Fig. 3.1). The pendulum had an equivalent length of 3.35 cm and an equivalent mass of 0.0124 kg. The generator included a cylindrical rare-earth magnet as the rotor and two identical windings as the stator. The magnet was diametrically magnetized with a length of

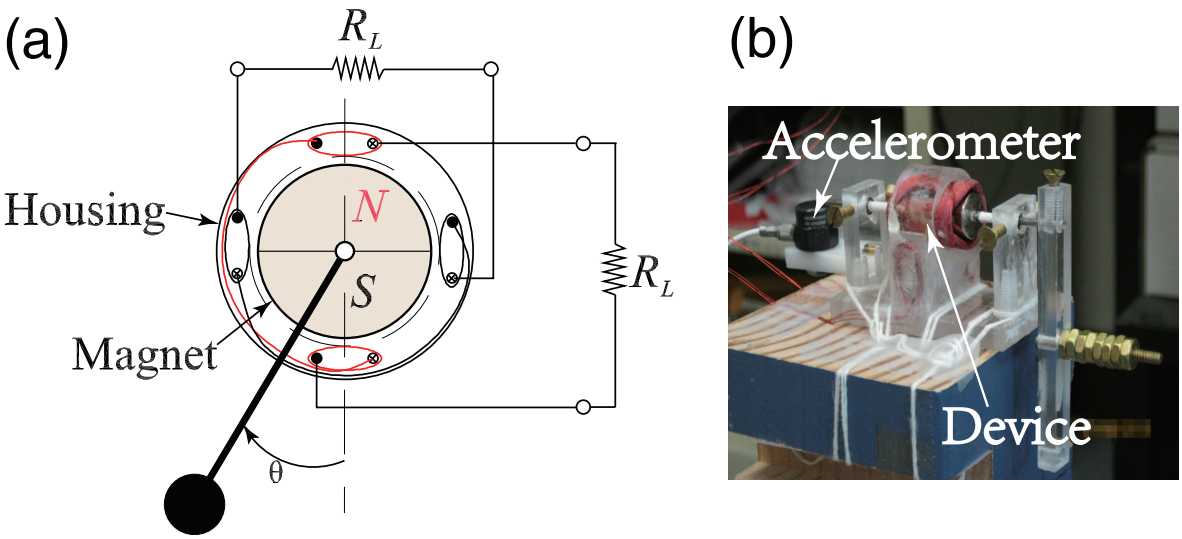

Figure 3.1: Prototype device: (a) a schematic diagram and (b) the experiment apparatus (the shaker, electrical load and the oscilloscope are not shown).

2.54 cm, a circular cross section of 1.27 cm in diameter and a mass of 0.0241 kg. The maximum magnetic flux density was measured at 0.549 T on the surface. The windings were orthogonally oriented and connected to a resistive load, R_L. This configuration ensured that the electromagnetic force induced can be modeled using an equivalent viscous damping force [78, 79]. The windings were fabricated using AWG #44 copper wire, each with 2400 turns. The resistances, R_w, were 1380 ohms and 1420 ohms for the two windings, respectively. The linear fundamental frequency and viscous damping ratio of the device were $\omega_n = 2.68$ Hz and $\zeta_m = 6 \times 10^{-4}$, respectively, measured from free-vibration tests. A shaker (Model LW-126-13, Labworks Inc.) with a real-time acceleration feedback control was used to excite the device. A resistive electrical load was used to evaluate the device's energy harvesting performance. The amount of electrical energy harvested was calculated based on the time histories of the voltage across the load, measured with a digital phosphor oscilloscope (Model DPO3040, Tektronix).

3.2.2 Theoretical Results

Assuming the acceleration of the base excitation took the form of $\ddot{x}_0(t) = A_e \cos \Omega t$, the dynamics of the device could be governed by:

$$\ddot{\theta} + \gamma\dot{\theta} + \sin\theta = p\cos(\omega_f \tau)g(\theta), \tag{3.3}$$

where θ is the angular displacement of the pendulum, ($\ddot{}$) and ($\dot{}$) denote the first and second derivatives with respect to a scaled time variable $\tau = \omega_n t$ and $\omega_f = \Omega/\omega_n$, $p = A_e/g$, $\gamma = 2\zeta$, respectively, where ζ represents the total damping ratio. Parameterization of the excitation is represented by: $g(\theta) = \cos(\theta - \alpha)$, where $\alpha = 0$ and $\alpha = \pi/2$ represent horizontal and vertical excitations, respectively. The frequency range of the normalized undisturbed system is $0 \leq \omega_0 \leq 1$.

The symmetry of the potential well meant that the response only contained odd harmonics [80], which can be written as: $\theta(\tau) = \sum_i A_i \cos(i\hat{\omega}\tau - \phi_i), i = 1, 3, 5\cdots$, where $\hat{\omega}$ is the fundamental characteristic frequency of the response and may or may not be within $[0, 1]$, depending on the excitation.

Modulation caused the forcing function to become $F(\tau) = p\cos\omega_f\tau\cos(\theta - \alpha)$. Using the Maclaurin series, $\cos\theta = 1 - \theta^2/2 + \cdots$, it has been established that for horizontal excitations ($\alpha = 0$), such self-modulation transforms the forcing function from a single-frequency excitation to an excitation with frequencies of $|\omega_f \pm 2m\hat{\omega}|$, where $m = 0, 1, 2, 3\cdots$. Eq. (3.3) can only be satisfied when $\omega_f = n\hat{\omega}, n = 1, 3, 5\cdots$. Similarly, for vertical excitations ($\alpha = \pi/2$) the modulation of $\sin\theta$ generates a spectrum where $|\omega_f \pm (2m+1)\hat{\omega}|$, and requires $\omega_f = n\hat{\omega}$ and $n = 2, 4, 6\cdots$. For both cases, $0 \leq \hat{\omega} \leq 1$ is necessary for the response to remain in the high-energy branch. The

modulated forcing function decomposes to:

$$F(\tau) = \sum_{i}^{\infty} A_{fi} \cos\left(i\hat{\omega}\tau - \phi_{fi}\right), \quad i = 1, 3, 5 \cdots . \tag{3.4}$$

For a pendulum, the response is dominated by the lowest harmonics, $A_1 >> A_3 >> \cdots$, thus $\theta \approx A_1 \cos(\hat{\omega}\tau - \phi_1)$. The average power dissipated per cycle is $P_d \approx \frac{1}{2}\gamma(\hat{\omega}A_1)^2$. The average input power is:

$$P_f = \frac{1}{2} p\hat{\omega} A_1 \left[J_{n-1}(A_1) + J_{n+1}(A_1)\right] \sin(\phi_1 - \phi_{f1}), \tag{3.5}$$

where $J_i(\cdot)$ is the ith Bessel function of the first kind. For a horizontal excitation, $n = 1, 3, 5 \cdots$. For a vertical excitation, $n = 2, 4 \cdots$. The maximum power is achieved when $\phi_1 - \phi_{f1} = \frac{\pi}{2}$, which determines the damping level required for resonance,

$$\gamma_{\text{res}} = \frac{p}{\hat{\omega} A_1} \left[J_{n-1}(A_1) + J_{n+1}(A_1)\right]. \tag{3.6}$$

Modulation of the excitation provides a cross-frequency energy transfer where the actual forcing function contains the same frequencies as the response. As long as these frequencies are supported by the potential well, the above resonance condition can be met for higher order subharmonic oscillations. However, for a torque excitation or a standard Duffing oscillator, where $g(x) = 1$, while the requirement of $\omega_f = n\hat{\omega}, n = 1, 3, 5 \cdots$ is still valid for steady-state response, the dissipated energy can only be compensated by the external work for a single frequency, ω_f. The response is dominated by the first harmonics, thus, the resonance condition can only be met in the primary zone where $n = 1$. A subharmonic oscillation ($n > 1$) can occur when the system cannot be driven to resonance because of the frequency mismatch between the response ($\hat{\omega}$) and the forcing function ($\omega_f = n\hat{\omega}$). The response can be large, but has a significantly low harvested power. When $n = 1$ and $\omega_f = \hat{\omega} > 1$, the frequencies are not supported by the

potential well. Here, bifurcation does not occur and the response is on the low-energy orbit. When $\omega_f = \hat{\omega} < 1$, super harmonic oscillations with a large response are possible. However, the resonance condition cannot be met because of the additional unwanted frequencies in the response. Super harmonic oscillations require strong excitations to maintain, but do not improve the energy harvesting efficiency.

3.3 Results and Discussion

Fig. 3.2 shows the results from theoretical and numerical studies. The numerical results were obtained using the Dormand-Prince method (MATLAB© ode45). The torque, horizontal and vertical excitations were considered. For all cases, the excitation level was maintained at $p = 0.3$, i.e. $A_e = 0.3g$. The damping level used in the non-resonance cases was kept at $\gamma = 4 \times 10^{-3}$, corresponding to an electrical load of approximately 100 kΩ. The damping levels required for resonance were obtained using Eq. (3.6). Fig. 3.2a shows that the amplitudes obtained numerically agreed with the theoretical predictions, which are the undisturbed amplitudes. The amplitudes of the non-resonance responses were generally higher than those at resonance. For higher excitation frequencies, particularly in the subharmonic regions, the differences in the amplitudes for the non-resonant and resonant responses were small. This reduced discrepancy does not automatically indicate that the non-resonant responses were close to resonance. The proximity to resonance is better illustrated using the phase difference between the response and the modulated forcing function, $\Delta\phi = \phi_1 - \phi_{f1}$, as shown in Fig. 3.2b. The phase differences between the non-resonant responses were far from $\pi/2$. The dissipated power is shown in Fig. 3.2c. While the responses were lower at resonance, significantly more energy was dissipated than elsewhere. As shown in Fig. 3.2d, the damping levels under the resonance condition were much higher than those for the non-resonant responses, especially at lower frequencies. As higher damping

levels indicate that larger electrical loads are allowed without sacrificing the power output, this feature is beneficial for applications that require large electrical loads. The experimental results are outlined in Fig. 3.3. Because of the limitations of the experiment apparatus, three excitation levels were used: $p = 0.05, 0.1, 0.3$, for the different dynamic zones. The results obtained both theoretically and numerically are also shown for comparison. The actual power delivered to the electrical load was on the order of mW for the relatively low excitation levels. The phase difference, $\Delta\phi$, was found numerically to be mainly around $\pi/2$, indicating resonance. For very low frequencies, i.e. below 2 Hz, the phase difference deviated from the theoretically predicted $\pi/2$. This was because at lower frequencies, the 3rd harmonic component had a sufficiently large contribution to the total amount of external work (Fig. 3.3d) and cannot be ignored in the resonance condition. In this case, Eq. (3.6) is not valid. Resonance requires matching of both frequencies, i.e. $\omega_0, 3\omega_0$, as predicted by Eq. (3.2b).

3.4 Concluding Remarks

In summary, the potential benefits of nonlinear oscillators in energy harvesting arise primarily from the fact that a range of "natural"frequencies are supported in the potential well, as indicated by the bent response curve of an undisturbed system. As a fundamental frequency and its higher order counterparts represent the inherent conversion rate of the kinetic and potential energies of a system, it was demonstrated that when external forces were in pace with the rate (i.e. the frequencies were matched), multi-frequency resonance could occur. The dissipated energy was compensated instantaneously without distorting the system energy. Thus, the energy harvesting efficiency was maximized. Such a multi-frequency resonance is beneficial for energy harvesting, particularly for periodic broadband vibrations in which steady state responses exist. Linear resonance is a special case of the generalized global resonance condition. Be-

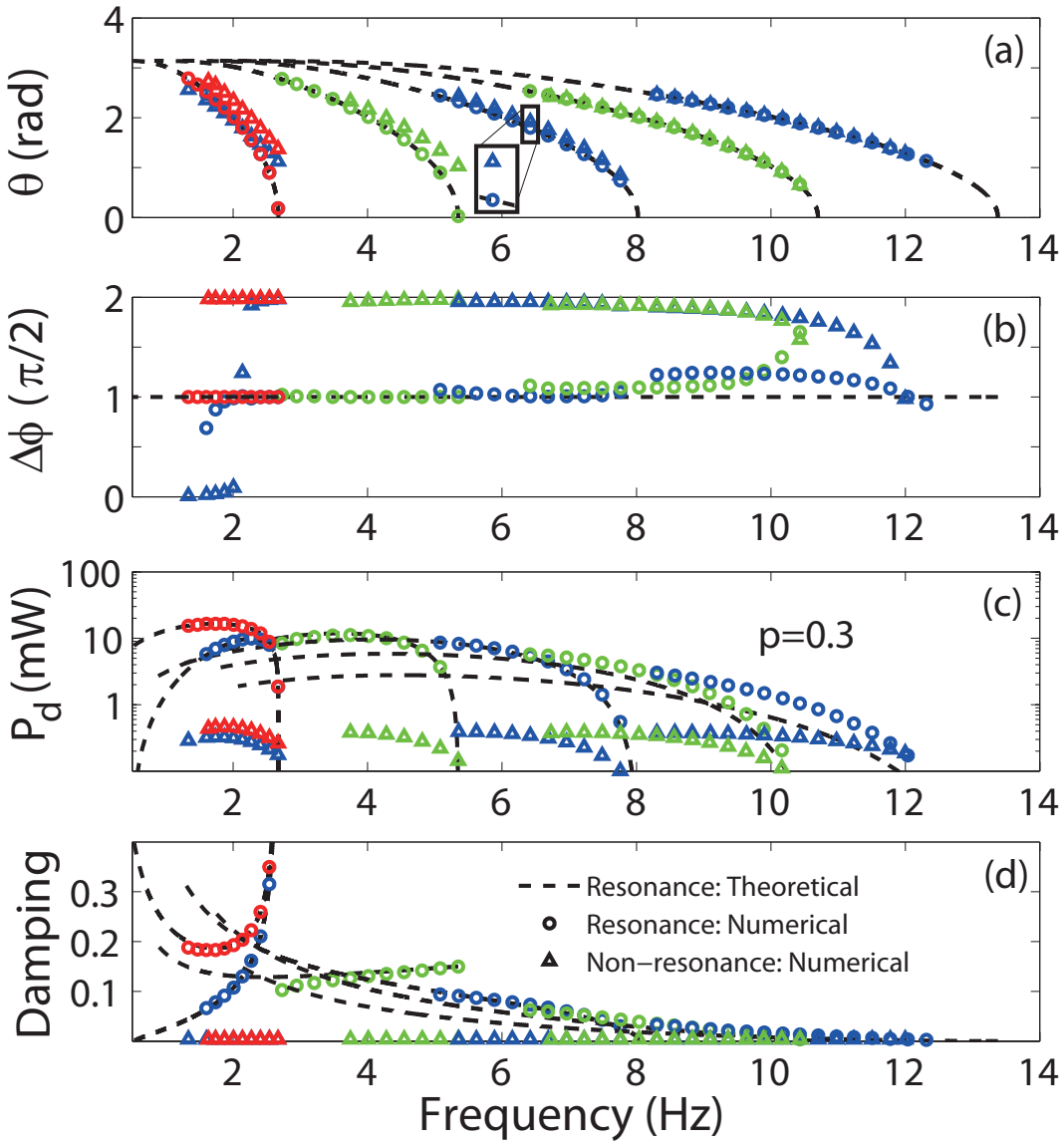

Figure 3.2: Results of theoretical and numerical studies for the resonance and non-resonance cases under three types of excitations (torque, vertical and horizontal) with the same amplitude of $p = 0.3$. (a) A response curve of the angular displacement, (b) the phase angle between the response and forcing function, (c) the dissipated power and (d) the damping levels. Red: torque excitation, green: vertical excitation, and blue: horizontal excitation.

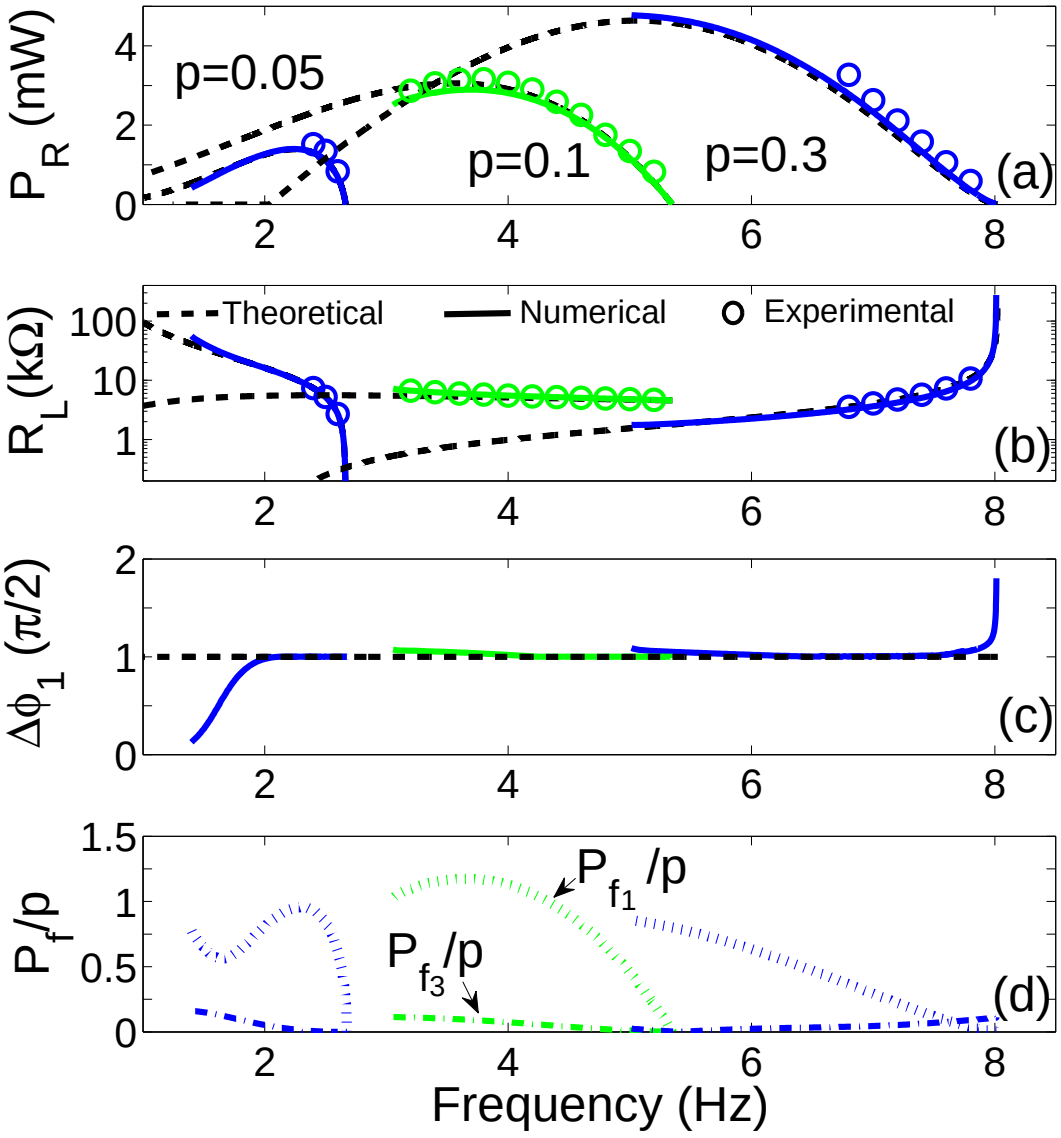

Figure 3.3: Experimental results of the device performance at resonance under horizontal excitations ($1:1$ and $3:1$ subharmonic oscillations) and a vertical excitation ($2:1$ subharmonic oscillations). (a) The power delivered to the electrical load, (b) the load resistance, (c) the phase between response and forcing function and (d) the scaled amplitude of the power of forcing function ($P_{fi} = i\hat{\omega}A_iA_{fi}$). Horizontal excitations: blue, vertical excitation: green.

cause of the principle of superposition, in a linear system, the response from the linear resonance coexists with the non-resonant response, as long as the correct frequency is provided in the excitation. In a nonlinear system, the principle of superposition is generally not applicable. The condition of global resonance is more stringent and may be difficult to achieve and maintain in a passive system. Thus, the effectiveness of the commonly adopted passive nonlinear energy harvesting methodology is limited. The fact that this condition involves more system parameters offers more opportunities in tuning the system to stay at resonance. As demonstrated, achieving nonlinear resonance can be facilitated by tuning the damping and modulation of the excitation. A paradigm shift towards active approaches appears to be necessary for reaping the full potential offered by the richness and versatility of nonlinear dynamics.

Chapter 4

POTENTIAL OF USING GLOBAL RESONANCE TO ENHANCE ENERGY HARVESTING PERFORMANCE

In vibration energy harvesting, frequency response of the harvesting device has been used as the primary metric in performance evaluation. For linear approaches, the frequency response curve shows that devices can perform well (i.e. efficiently) when the excitation is only within a frequency range defined by the half-power bandwidth of the device's fundamental frequency. For ambient vibrations in which energy is distributed over a wide spectrum of frequencies or the dominating frequency is time-varying, linear devices become less efficient. Seeking ways to broaden the device bandwidth is the dominant trend as reported in the literature. Motivated by the unique characteristics of nonlinear systems, which seem intuitively beneficial for widening the bandwidth, nonlinearity has been intentionally introduced to vibration energy harvesting devices in recent decades ([9, 10]). The frequency response curve shows that a nonlinear device has a broader bandwidth than its linear counterpart ([47, 50, 78, 79, 81, 82]). However, it is noted that the principle of superposition does not apply to nonlinear systems. Thus, the "broadband" performance does not indicate that the nonlinear device will have improved performance under multi-frequency excitation. On the contrary, it has been shown that nonlinear devices may not offer any benefit under multi-frequency

excitation ([59–62]).

In addition, since mechanical energy is mostly harvested through damping ([63]), generating a large-amplitude response is intuitively beneficial for vibration energy harvesting. Seeking ways to increase device response is thus the essential manner to enhance device performance in the majority of existing schemes. However, while increasing the device response amplitude is advantageous to linear approaches, it may not improve performance for nonlinear devices. In linear devices, the optimal performance occurs at resonance. The largest-amplitude response and the maximum amount of energy harvested are simultaneously achieved at the resonant condition. In nonlinear devices, the conditions for optimal performance are different. A recent study has shown that a nonlinear device can obtain optimal performance only at global resonance, where the corresponding response amplitude is not at a maximum ([83]).

In this chapter, therefore, fundamental issues are addressed with respect to bandwidth and nonlinear resonance to enhance energy harvesting performance. It is shown that using bandwidth as a performance criterion may be problematic for linear devices, and it may be misleading when extended to nonlinear devices. To address the use of a large-amplitude response to enhance nonlinear energy harvesting, this study compares the device performance at the global resonance to that at the so-called nonlinear resonance, and thus reveal the real potential of nonlinear approaches in vibration energy harvesting.

4.1 Governing Equation

Consider an electromechanical energy harvesting device driven by a periodic excitation and assume that the electrical load of the device is purely resistive. The governing

equation of the device dynamics can be generally written as

$$m\ddot{x} + c_m\dot{x} + \frac{\partial V(x)}{\partial x} + \kappa y = f(x,t)\,, \tag{4.1a}$$

$$\alpha\dot{y} + \beta y = \kappa\dot{x}\,, \tag{4.1b}$$

where x denotes the displacement of the seismic mass m, ($\dot{}$) and ($\ddot{}$), respectively, represent the first and second derivatives of x with respect to the time t, c_m is the mechanical damping coefficient, $V(x)$ is the potential well function of the system, κ is the linear electromechanical coupling coefficient, and $f(x,t) = f(x,t+T)$ denotes the general external force with a fundamental period of T, including parametrical excitations (e.g. $f(x,t) = p(t)\sin x$ where $p(t)$ is the external excitation). For inductive devices, y, α and β represent the induced current, the inductance of the winding, and the total resistance, respectively. For capacitive ones, they represent the induced voltage, the capacitance of the piezoelectric element, and the load conductance, respectively. In this study, assuming $\alpha << \beta$ and considering low-frequency excitations, the electromechanical coupling, Equation (4.1b), can be approximated as an algebraic relationship, i.e. $\beta y = \kappa\dot{x}$. The governing equation is thus simplified as

$$\ddot{x} + \gamma\dot{x} + \frac{\partial U(x)}{\partial x} = F(x,t)\,, \tag{4.2}$$

in which the total system damping coefficient is defined as $\gamma = \frac{c_m+\kappa^2/\beta}{m}$, and $U(x) = \frac{V(x)}{m}$, $F(x,t) = \frac{f(x,t)}{m}$.

4.2 Bandwidth

4.2.1 Linear System

Considering a linear device (i.e. $U(x) = \frac{1}{2}\omega_n^2 x^2$ where ω_n is the natural frequency) driven by a single-frequency excitation (e.g. $F(x,t) = A_e \cos \omega t$), the average power dissipated by damping within the period of $T = \frac{2\pi}{\omega}$ is calculated to be

$$P_d = \frac{1}{T}\int_0^T \gamma \dot{x}^2 \mathrm{dt} = \frac{\frac{A_e^2}{2}\frac{\gamma}{\omega_n^2} r^2}{\left(1-r^2\right)^2 + \left(\frac{\gamma}{\omega_n} r\right)^2}\,, \tag{4.3}$$

where $r = \frac{\omega}{\omega_n}$. From Equation (4.3), dividing by $\frac{A_e^2}{2}$ normalizes the average power P_d, as

$$\bar{P}_d = \frac{\frac{\gamma}{\omega_n^2} r^2}{\left(1-r^2\right)^2 + \left(\frac{\gamma}{\omega_n} r\right)^2}\,. \tag{4.4}$$

The response amplitude is calculated as

$$X_A = \frac{\frac{A_e}{\omega_n^2}}{\sqrt{\left(1-r^2\right)^2 + \left(\frac{\gamma}{\omega_n} r\right)^2}}\,. \tag{4.5}$$

According to Equations (4.4) and (4.5), it can be seen that when $r = 1$ (i.e. $\omega = \omega_n$), the normalized average power $\bar{P}_d$ and the response amplitude X_A are simultaneously maximized:

$$\bar{P}_{d_{\max}} = \frac{1}{\gamma}\,, \tag{4.6a}$$

$$X_{A_{\max}} = \frac{A_e}{\gamma \omega_n}\,. \tag{4.6b}$$

It can be seen that the maximum normalized average power $\bar{P}_{d_{\max}}$ and the maximum response amplitude $X_{A_{\max}}$ are inversely proportional to the total damping γ. Equations (4.6a) and (4.6b) also confirm that increasing the device response amplitude by

decreasing the total damping is beneficial for energy harvesting performance.

Based on the definition of the half-power bandwidth, the cutoff frequencies (see Figure 4.1) satisfy the condition $\frac{\bar{P}_d}{\bar{P}_{d_{\max}}} = \frac{1}{2}$, and thus can be derived as

$$r_{1,2} = \sqrt{1 + 2\left(\frac{\gamma}{2\omega_n}\right)^2 \pm 2\left(\frac{\gamma}{2\omega_n}\right)\sqrt{1 + \left(\frac{\gamma}{2\omega_n}\right)^2}}\,. \tag{4.7}$$

Then, the half-power bandwidth of a linear device is obtained as

$$BW = \omega_n\,(r_1 - r_2) = \gamma\,. \tag{4.8}$$

Equation (4.8) shows that the half-power bandwidth of a linear device is proportional to the total damping coefficient γ and is independent of the excitation level A_e.

A linear device with a natural frequency of $\omega_n = 1$ rad·s^{-1} was used as an illustrative example. Three damping levels were considered: $\gamma = 0.2$, 0.5, and 1 N·s·m^{-1}·kg^{-1}. The excitation level was fixed at the same level. Figure 4.1 shows the frequency response curve for the normalized average power. It can be seen that $\gamma = 1$ N·s·m^{-1}·kg^{-1} gives the largest bandwidth in the three cases considered, as theoretically predicted by Equation (4.8). If the bandwidth is used as the criterion to measure device performance, for this example a linear device with $\gamma = 1$ N·s·m^{-1}·kg^{-1} would be the best design. However, the objective of vibration energy harvesting is to harvest as much energy as possible from the excitation. Assuming multi-frequency excitation, the design with $\gamma = 1$ N·s·m^{-1}·kg^{-1} would provide the best performance only when the excitation frequencies are outside of the range defined by EF. When the excitation frequencies are within the range defined by CD, the design with the largest bandwidth becomes the worst among the three cases considered. As theoretically predicted by Equation (4.6a), the broadened bandwidth is achieved at the cost of significant reduction of energy harvested at resonance. Therefore, when using a linear device to harvest energy from

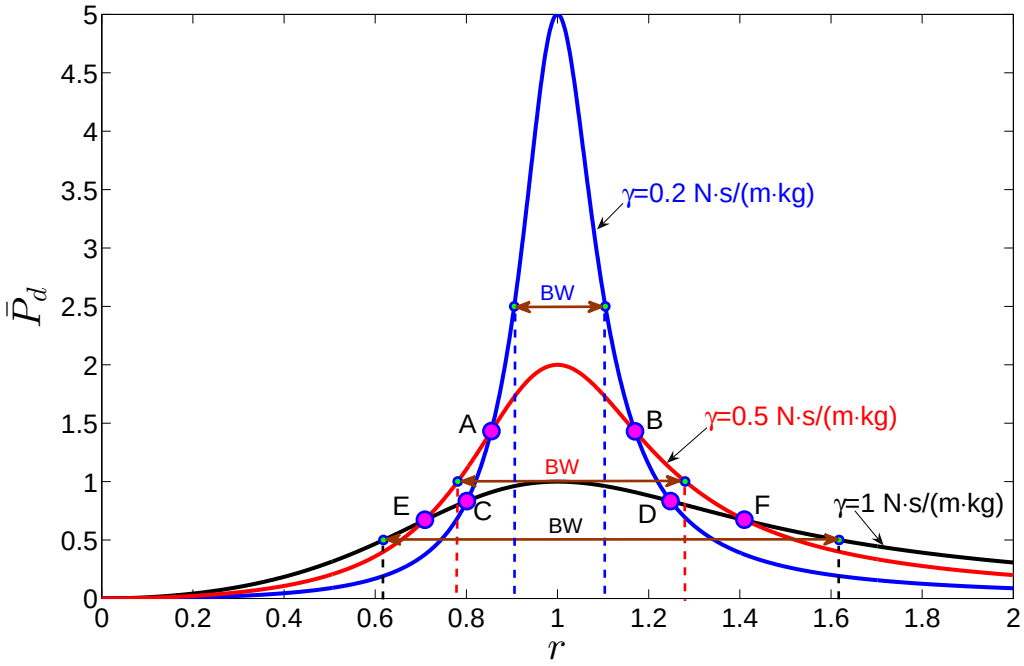

Figure 4.1: Frequency response curve for the normalized average power dissipated of a linear system.

multi-frequency excitation, achieving resonance is more beneficial for enhanced energy harvesting performance than broadening device bandwidth.

4.2.2 Nonlinear System

For a nonlinear device, a single-frequency response curve for its average power dissipated depends not only on the system parameters, but also on the excitation level, and thus the half-power bandwidth. Since closed-form solutions for nonlinear systems shown in Equation (4.2) do not exist, it is impossible to theoretically obtain the relation of the half-power bandwidth with respect to the system parameters of a nonlinear device and the excitation level. In this study, the half-power bandwidth of a nonlinear device is numerically investigated through the Dormand-Prince method (ode45 in MATLAB®), and is defined by the frequency range between the half-power cut-off frequency and

the jump-off frequency. Two nonlinear systems were considered: one with a softening nonlinearity, i.e. $U(x) = \frac{1}{2}x^2 - \frac{1}{24}x^4$, and the other one with a hardening nonlinearity, i.e. $U(x) = \frac{1}{2}x^2 + \frac{1}{24}x^4$. The effects of the system damping and the excitation level on the device bandwidth were investigated respectively. The numerical results for the two nonlinear systems under single-frequency excitation (i.e. $F(x,t) = A_e \cos \omega t$) are summarized in Figure 4.2. Figure 4.2 (a) and (b) describe the effects of the system damping on the single-frequency response curve for the average power dissipated (i.e. $P_d = \frac{1}{T}\int_0^T \gamma \dot{x}^2 \mathrm{dt}$ where $T = \frac{2\pi}{\omega}$) of the two nonlinear systems, respectively. The excitation level was fixed at $A_e = 0.2$ m·s^{-2}, and three damping levels of $\gamma = 0.1$, 0.2, and 0.3 N·s·m^{-1}·kg^{-1} were considered. When the effect of nonlinearity on device dymanics could not be ignored (e.g. $\gamma < 0.3$ N·s·m^{-1}·kg^{-1}), the half-power bandwidth and maximum average power dissipated were reduced as the damping level increased. However, when the response was small enough (e.g. $\gamma \geq 0.3$ N·s·m^{-1}·kg^{-1}) so that the effect of nonlinearity on device dynamics could be ignored, the nonlinear systems were equivalent to linear systems, and thus, the half-power bandwidth could be estimated by Equation (4.8). Figure 4.2 (c) and (d) show the relation of the device performance to the excitation level. The damping level was maintained at $\gamma = 0.2$ N·s·m^{-1}·kg^{-1}, and three excitation levels were used: $A_e = 0.2$, 0.3, and 0.4 m·s^{-2}. It can be seen that a higher excitation level corresponded to a larger half-power bandwidth and average power dissipated. For the device with a soften nonlinearity, increasing excitation level could reduce the half-power bandwidth due to system stability limitations (see Figure 4.2 (c)).

According to the single-frequency response curves, nonlinear systems may perform well over a broad spectrum of frequencies. Since the principle of superposition does not apply, however, such "broadband" performance cannot be used to predict the performance of nonlinear systems under multi-frequency excitation. As shown in Figure 4.3, for example, the average power dissipated by the first nonlinear system under exci-

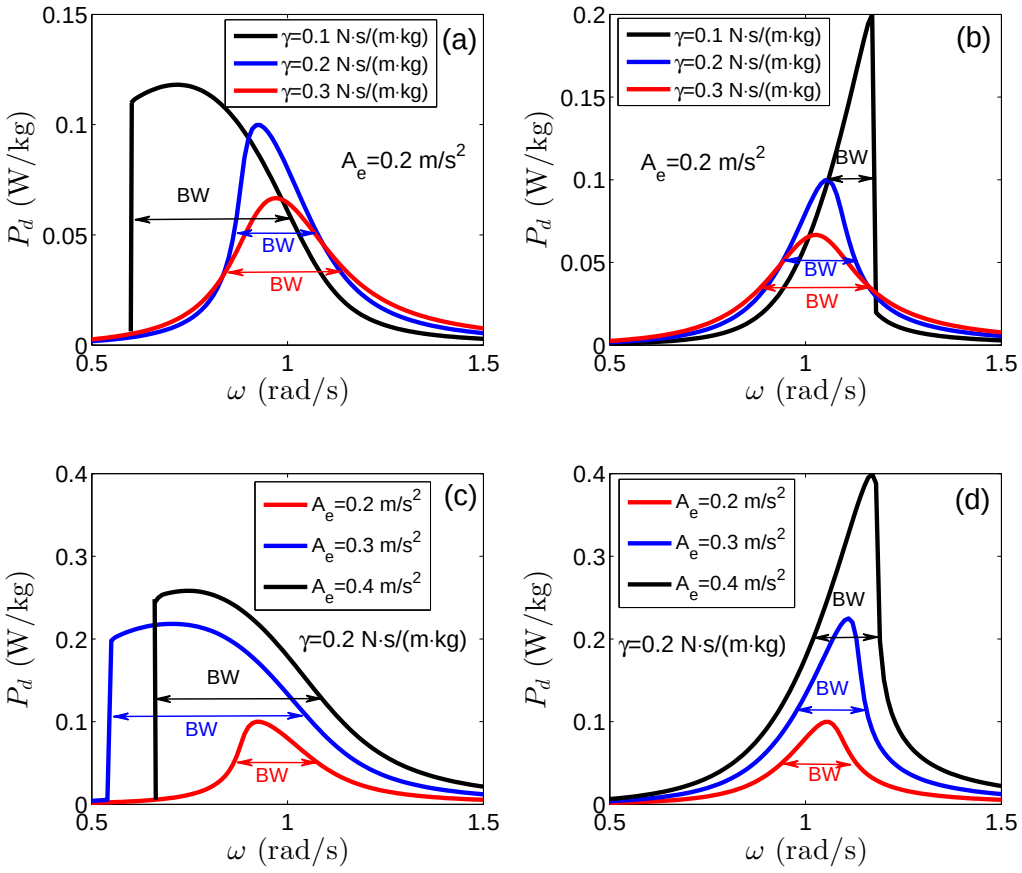

Figure 4.2: Frequency response curves for average power dissipated in two nonlinear systems, i.e. $P_d = \frac{1}{T}\int_0^T \gamma \dot{x}^2 \mathrm{dt}$ where $T = \frac{2\pi}{\omega}$. (a) and (c): $U(x) = \frac{1}{2}x^2 - \frac{1}{24}x^4$; (b) and (d): $U(x) = \frac{1}{2}x^2 + \frac{1}{24}x^4$.

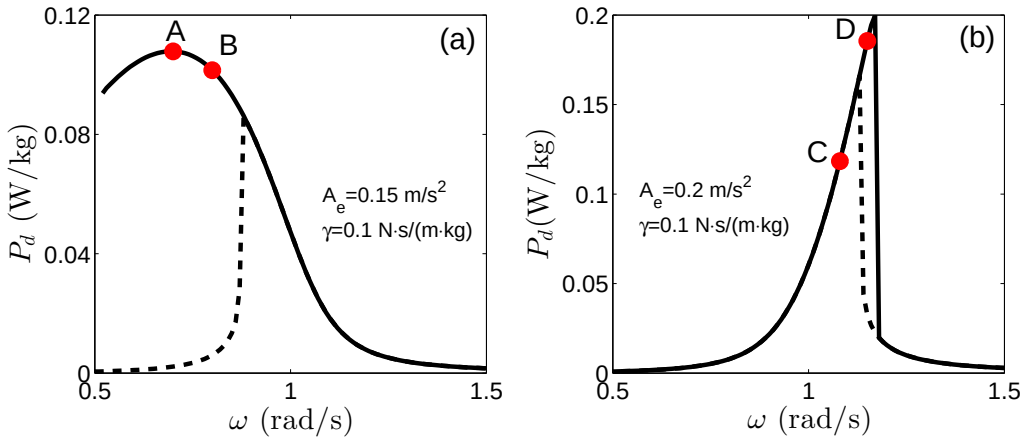

Figure 4.3: Frequency response curves for average power dissipated P_d in two nonlinear systems: (a) $U(x) = \frac{1}{2}x^2 - \frac{1}{24}x^4$, $\gamma = 0.1$ N·s·m^{-1}·kg^{-1}, and $A_e = 0.15$ m·s^{-2}; (b) $U(x) = \frac{1}{2}x^2 + \frac{1}{24}x^4$, $\gamma = 0.1$ N·s·m^{-1}·kg^{-1}, and $A_e = 0.2$ m·s^{-2}.

tations A and B was $P_d(A) = 0.1078$ W·kg^{-1} and $P_d(B) = 0.1015$ W·kg^{-1}, respectively; the average power dissipated by the second one under excitations C and D was $P_d(C) = 0.1184$ W·kg^{-1} and $P_d(D) = 0.1855$ W·kg^{-1}, respectively. When the excitation contained the two frequencies, however, the average power dissipated through the first system was $P_d(A + B) = 0.0109$ W·kg^{-1}, while the average power dissipated by the second device was $P_d(C + D) = 0.1405$ W·kg^{-1}. It can be seen that the average power dissipated under multi-frequency excitation was smaller than the sum of the average power dissipated under the single-frequency excitations. For the device with a softening nonlinearity shown in Figure 4.3(a), the average power dissipated under multi-frequency excitation (i.e. $P_d(A + B)$) was even orders of magnitude smaller than that from either of the single-frequency excitations. The time histories of power dissipation of the two nonlinear systems under multi-frequency excitation are shown in Figure 4.4 (a) and (b), respectively.

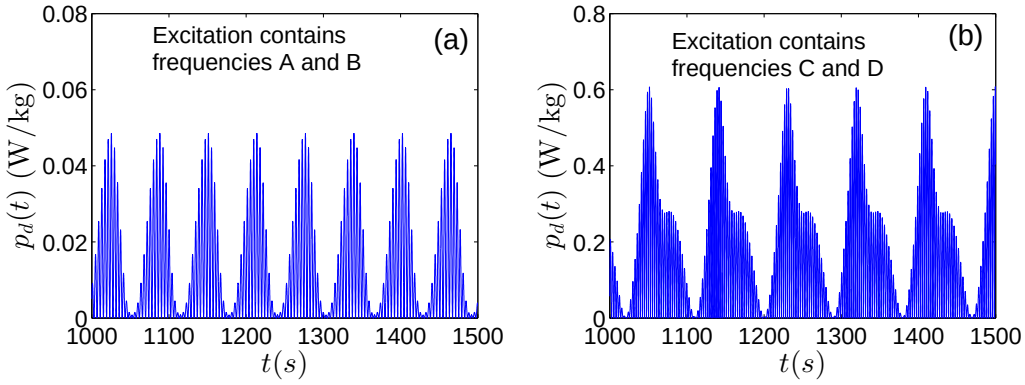

Figure 4.4: Time histories for instantaneous power dissipated (i.e. $p_d(t) = \gamma\dot{x}^2$ in two nonlinear systems: (a) $U(x) = \frac{1}{2}x^2 - \frac{1}{24}x^4$, $\gamma = 0.1$ N·s·m^{-1}·kg^{-1}, and $A_e = 0.15$ m·s^{-2}; (b) $U(x) = \frac{1}{2}x^2 + \frac{1}{24}x^4$, $\gamma = 0.1$ N·s·m^{-1}·kg^{-1}, and $A_e = 0.2$ m·s^{-2}.

4.3 Large-Amplitude Response and Nonlinear Resonance

For a dynamic system (as shown in Equation (4.2)), it has shown that the system can be at global resonance with the excitation only when the following condition is satisfied ([83]),

$$\gamma\dot{x}_u = F(x,t)\,, \tag{4.9}$$

where the undisturbed response x_u is a response of the conservative system underlying Equation (4.2) (i.e. $\gamma = 0$ and $F(x,t) = 0$) with an initial displacement. For a linear system, the global resonance condition (i.e. Equation (4.9)) reduces to the linear resonance condition, $\omega = \omega_n$. For a nonlinear system, Equation (4.9) shows that except for the requirement of a frequency match between the excitation and the system, damping also plays a significant role in the global resonance condition. When the system is at global resonance, it is easy to derive the system energy $E(t) = \frac{\dot{x}_u^2}{2} + U(x_u) = \text{Constant}$, while the instantaneous power of the excitation is $p_f(t) = F(x,t)\dot{x}_u = \gamma\dot{x}_u^2 = p_d(t) \geq 0$, which shows that the instantaneous power dissipated equals to the instantaneous power

of the excitation, and the instantaneous power of the excitation is always non-negative, resulting in the maximum efficiency of the excitation work.

Different from the global resonance condition, however, resonance is conventionally regarded as the phenomenon that under specific excitations, the system can generate response with greater amplitude. For nonlinear systems, therefore, the responses with high energy levels in the bifurcation zone are traditionally defined as the nonlinear resonance responses. A branch with high-energy orbits in the bifurcation zone is the traditional "resonant" branch, as shown in Figure 4.5(a), which shows that response A corresponding to the traditional nonlinear "resonance" had a larger amplitude than response B near the undisturbed response curve. Conventionally, a larger response always results in more energy harvested. However, it is shown that the energy dissipated at response A is much lower than that at response B. According to Figure 4.5(b), it can be seen that the system energy at response A had a larger fluctuation than that at response B. It is implied that the energy dissipated through response A was much less than the available energy provided by the excitation source, leading to the extra available energy being temporarily stored in the system and then transferred back to the excitation source, and thus a lower efficiency of the excitation work. Figure 4.5(c) and (d) shows that although the amplitude of response A was larger than that of response B, the power dissipated at response A was seven-fold lower.

4.4 Potential of Nonlinear Energy Harvesting

For a nonlinear device, its undisturbed response contains multiple frequencies, which are determined by the potential function. Note that the potential functions of nonlinear systems can be generally classified as two categories, i.e. symmetric and asymmetric. For a nonlinear system with a symmetric potential function shown in Figure 4.6(a), for instance, the undisturbed response x_u only has the odd harmonics, i.e. ω_0, $3\omega_0$,

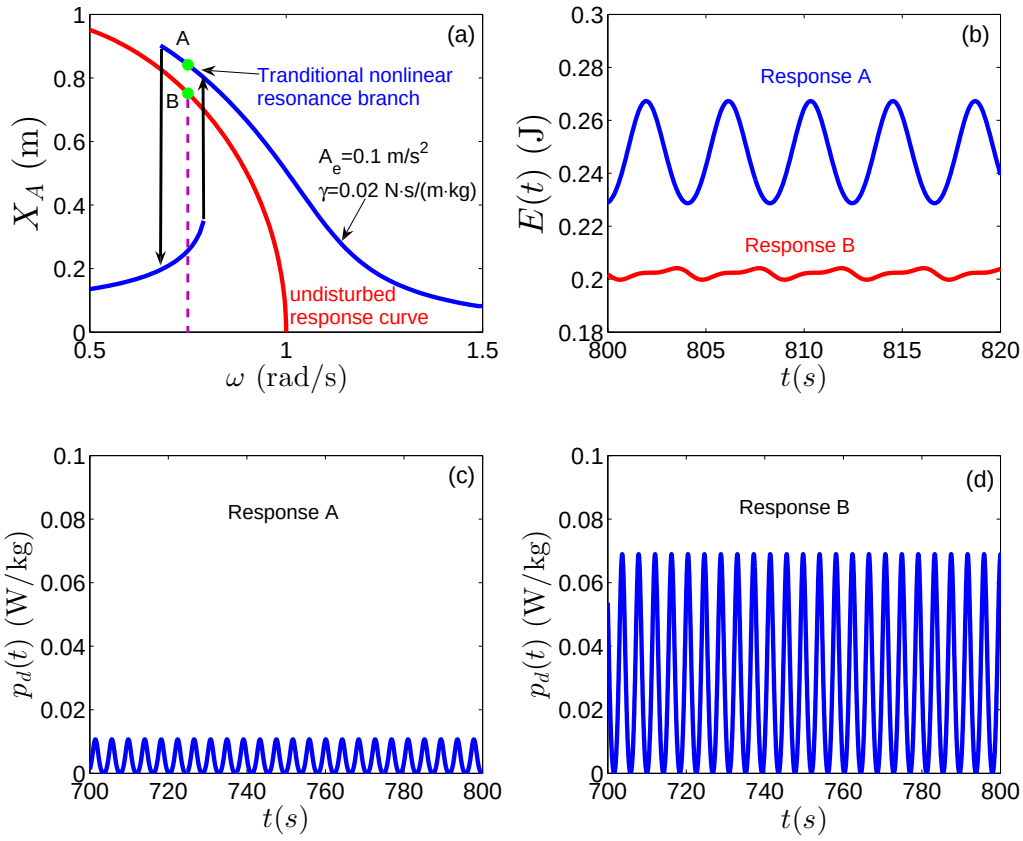

Figure 4.5: Performance comparison between the traditional nonlinear response and the response closed to global resonance: (a) Single-frequency response curve and undisturbed response curve for response amplitude of the nonlinear system with $U(x) = \frac{1}{2}x^2 - \frac{1}{4}x^4$, (b) system energy $E(t) = \frac{1}{2}\dot{x}^2 + U(x)$, (c) instantaneous power dissipated at response A, and (d) instantaneous power dissipated at response B.

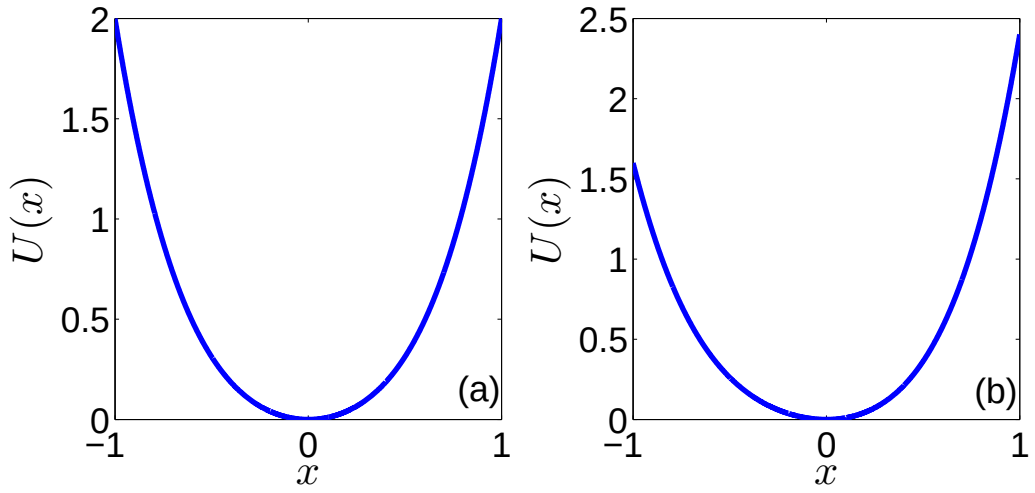

Figure 4.6: Potential functions of nonlinear systems $U(x)$: (a) symmetric and (b) asymmetric.

$5\omega_0, \cdots$, where ω_0 is the amplitude-dependent fundamental frequency. For a nonlinear system with an asymmetric potential function shown in Figure 4.6(b), however, the undisturbed response x_u contains both the odd and even harmonics, i.e. ω_0, $2\omega_0$, $3\omega_0$, $4\omega_0$, $\cdots$. Since the frequency content of the undisturbed response depend on the potential function and response amplitude, it is possible to achieve frequency matching between the undisturbed response and the multi-frequency excitation if the potential well of a nonlinear device can be properly designed, resulting in the satisfaction of the global resonance condition. Therefore, it is possible for nonlinear energy harvesting to harvest energy from multi-frequency excitation simultaneously, regardless of the broadband performance.

To demonstrate the potential of using global resonance to harvest energy from multi-frequency excitation, two numerical examples were considered. In the first example, the excitation only contained odd harmonics, and its frequency content and time history are shown in Figure 4.7(a) and (c), respectively. In the second example, the excitation had both odd and even harmonics, as shown in Figure 4.7(b) and (d). To match

the characteristics of the excitations such that the global resonance condition can be achieved, a symmetric potential well was designed as $U(x) = 30x^2 - 180x^4 + 123x^6$ in the first example, as shown in Figure 4.8(a) and (c); and an asymmetric potential well was designed as $U(x) = 50x^2 + 16.5x^3$ in the second example, as shown in Figure 4.8(b) and (d). To satisfy the requirement of Equation (4.9), the total system damping coefficient also needs to be matched, thus $\gamma = 0.4$ N·s·m^{-1}·kg^{-1} was designed. For comparison with linear resonance and traditional "nonlinear resonance", the linear, monostable, and bistable devices were also considered in the two examples. To maximize the performance of the device based on the linear method, the linear device was designed to be at resonance with the most dominant frequency of the excitation in each example. In the first example, thus, the natural frequency of the linear device was $f_n = 1.144$ Hz; while in the second example, the natural frequency of the linear device was $f_n = 1.013$ Hz. For the designed monostable and bistable devices, their responses at the most dominating frequency were located in the higher-energy orbits in the bifurcation zone. Figure 4.9(a) and (b) show the single-frequency response curves of the designed monostable and bistable devices, respectively. The energy harvesting performance of the devices considered in the two examples are summarized in Figures 4.10 and 4.11, respectively. It can be seen that in the devices considered, the nonlinear devices based on the global resonance provided the best performance, i.e. the highest energy efficiency and the largest energy dissipation. To the contrary, the device based on linear resonance only effectively and efficiently harvested the energy of the excitation distributed over the dominant natural frequency. For the monostable and bistable devices, however, their operations were much less efficient. The performance of the devices based on the traditional "nonlinear resonance", i.e. the monostable and bistable devices, was even lower than that of the device based on linear resonance.

The robustness of using global resonance to harvesting energy was then investigated. Noise of higher order harmonics was added to the excitations. The frequency content of

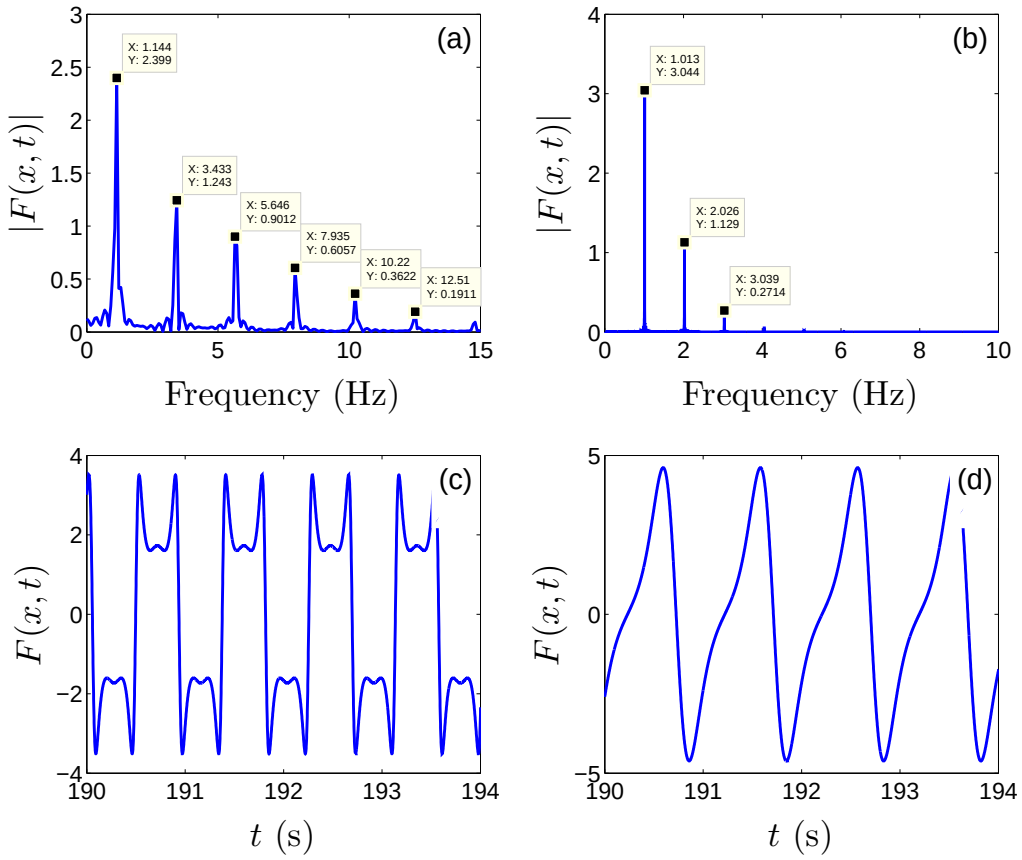

Figure 4.7: Frequency content and time history of excitations: (a) and (c) excitation for the first example; (b) and (d) excitation for the second example.

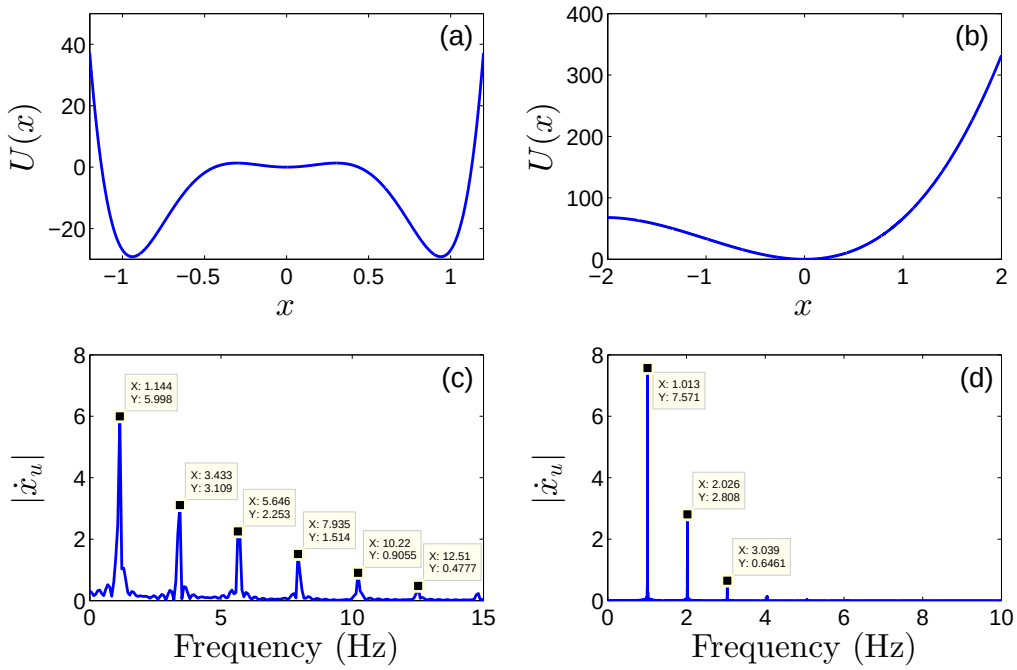

Figure 4.8: Potential function and the frequency content of an undisturbed response: (a) and (c) proposed device for the first example ($U(x) = 30x^2 - 180x^4 + 123x^6$); (b) and (d) proposed device for the second example ($U(x) = 50x^2 + 16.5x^3$).

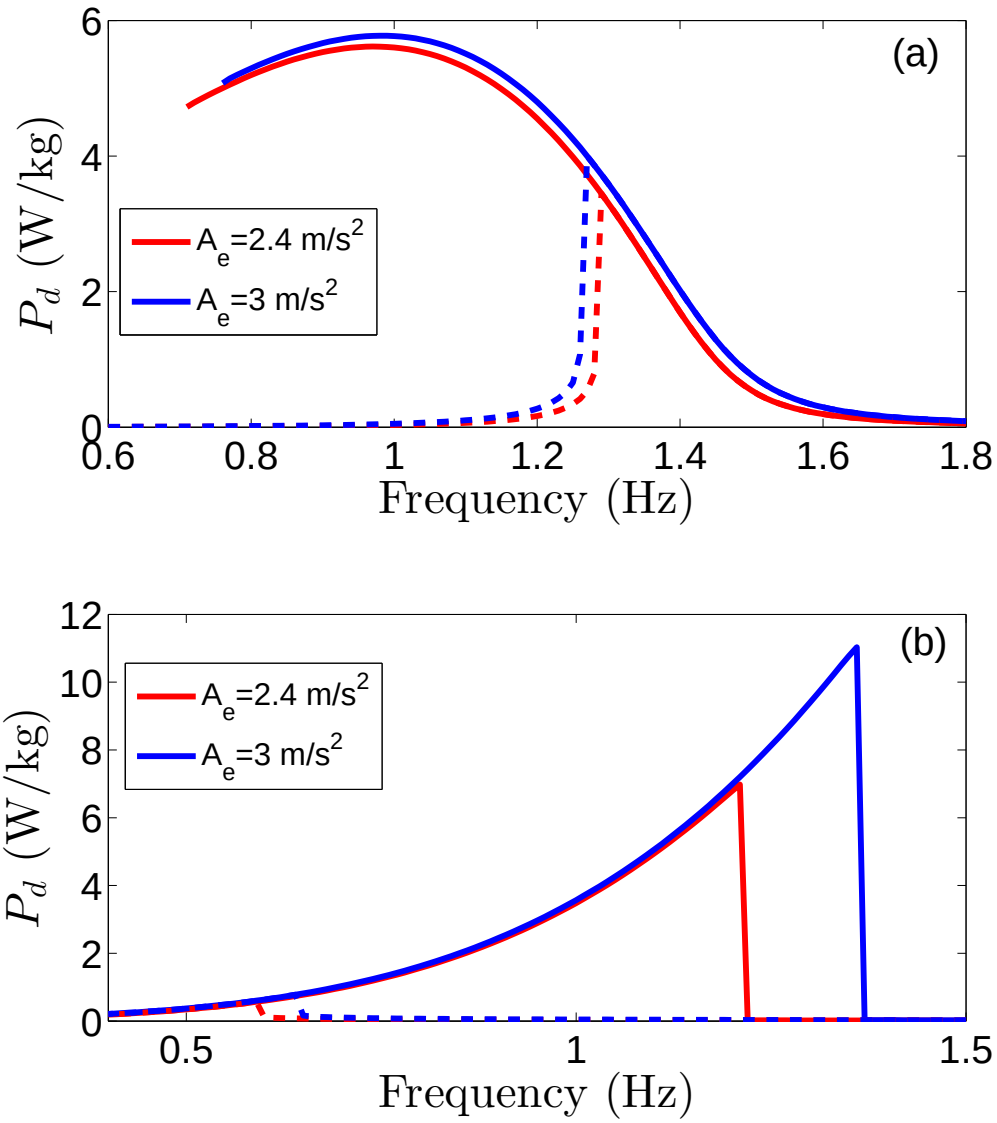

Figure 4.9: Frequency response under single-frequency excitation: (a) average dissipated power of monostable duffing device and (b) average dissipated power of bistable device. A_e is the excitation level.

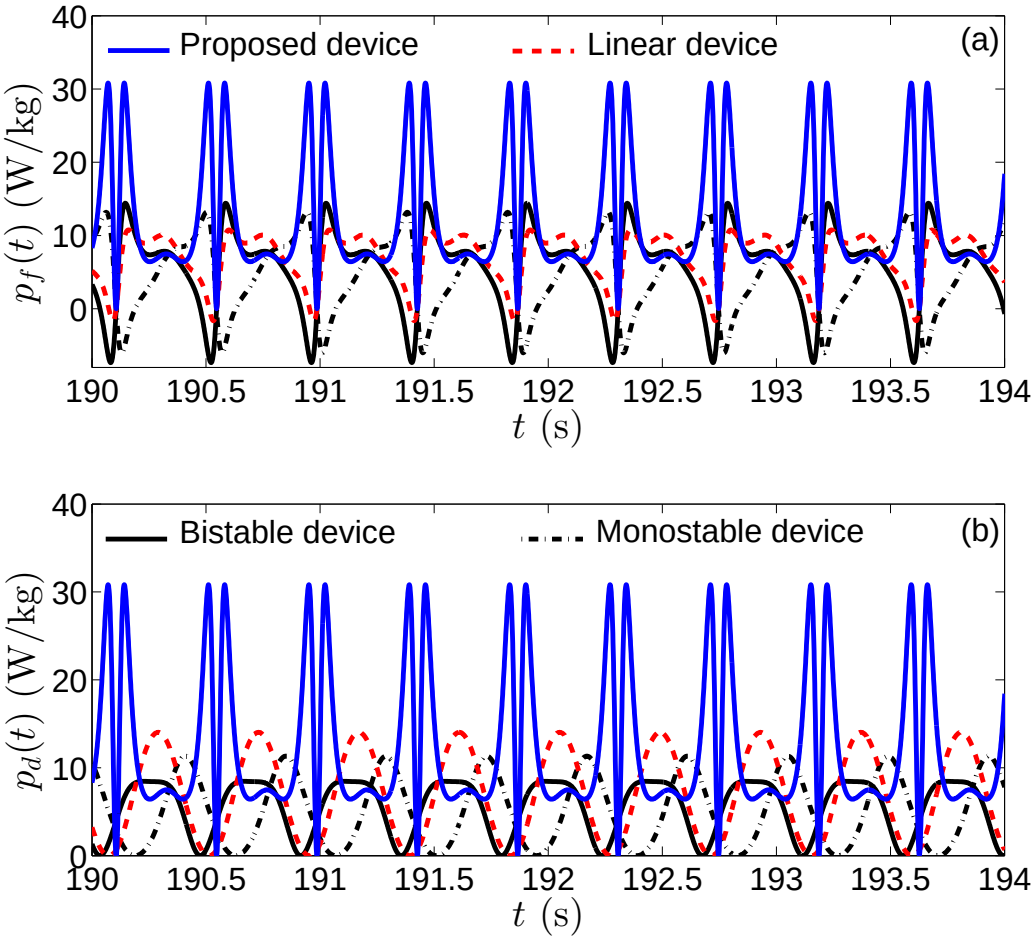

Figure 4.10: Time histories of (a) the instantaneous power of the excitation $p_f(t)$ and (b) the dissipated power $p_d(t)$ in the first example. Proposed device: $U(x) = 30x^2 - 180x^4 + 123x^6$; Linear device: $U(x) = 2(1.144\pi)^2 x^2$.

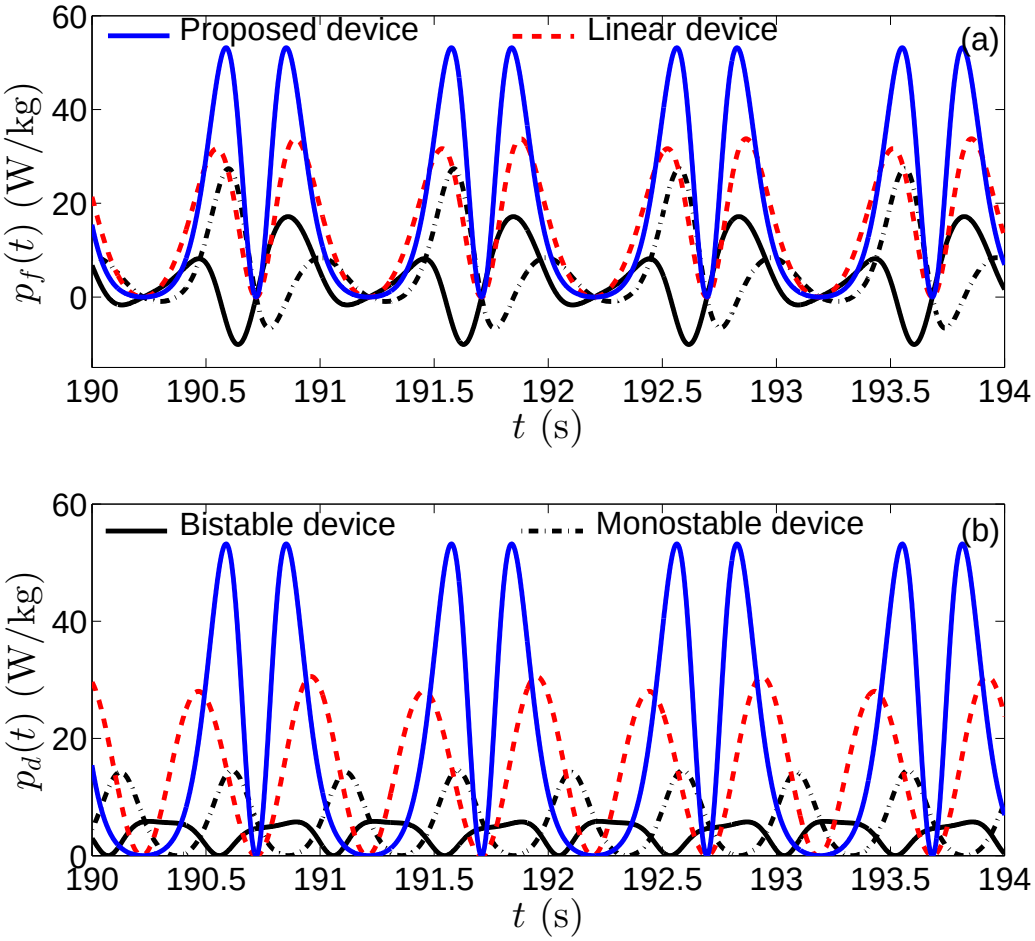

Figure 4.11: Time histories of (a) the instantaneous power of the excitation $p_f(t)$ and (b) the dissipated power $p_d(t)$ in the second example. Proposed device: $U(x) = 50x^2 + 16.5x^3$; Linear device: $U(x) = 2(1.013\pi)^2x^2$.

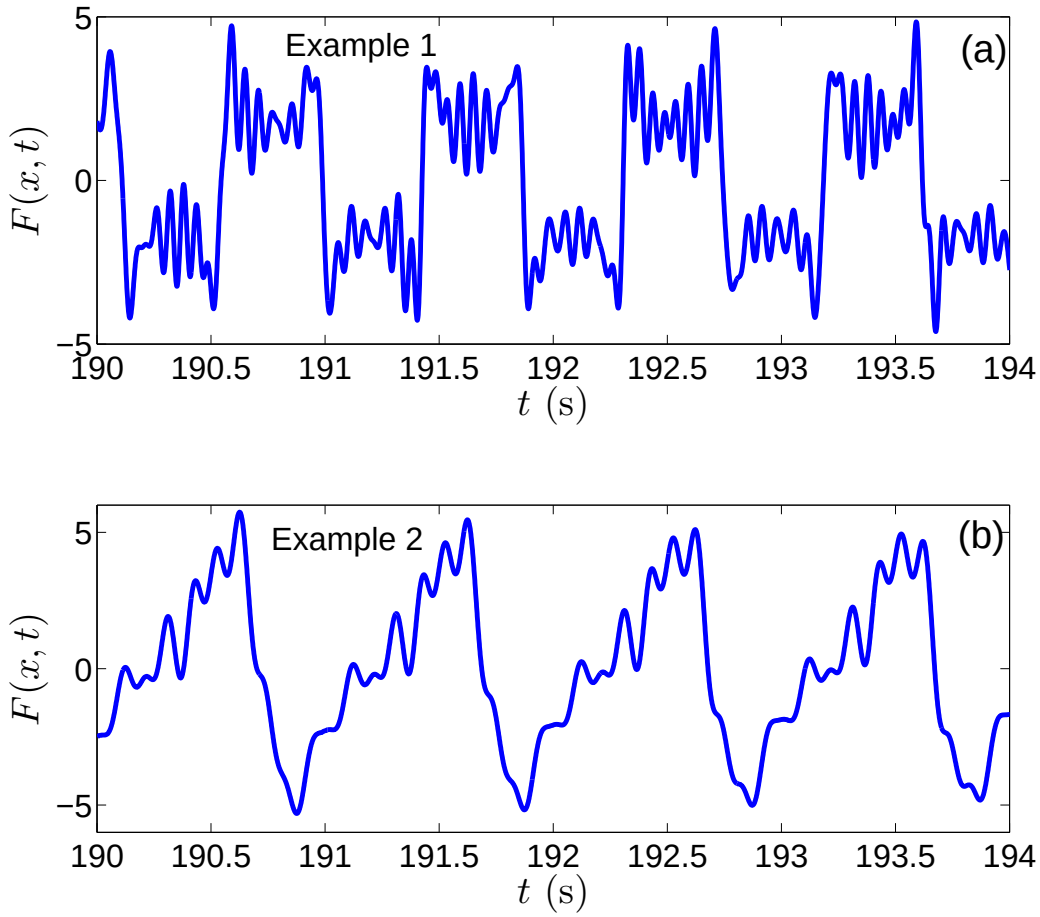

Figure 4.12: Time history of excitations which contain high-order harmonic noise for: (a) the first example and (b) the second example.

the noise-polluted excitations used in the two examples are shown in Figure 4.12(a) and (b), respectively. Since the monostable and bistable device exhibit lower performance than the linear device, only the device based on global resonance and the linear resonance device were considered. The performance of the devices under the noise-polluted excitations in the two examples is summarized in Figures 4.13 and 4.14, respectively. It can be seen that while the excitation contains high-order harmonics, which are not part of the frequencies supported by the potential well of the designed nonlinear devices, the improvement over the devices based on linear resonance is apparent.

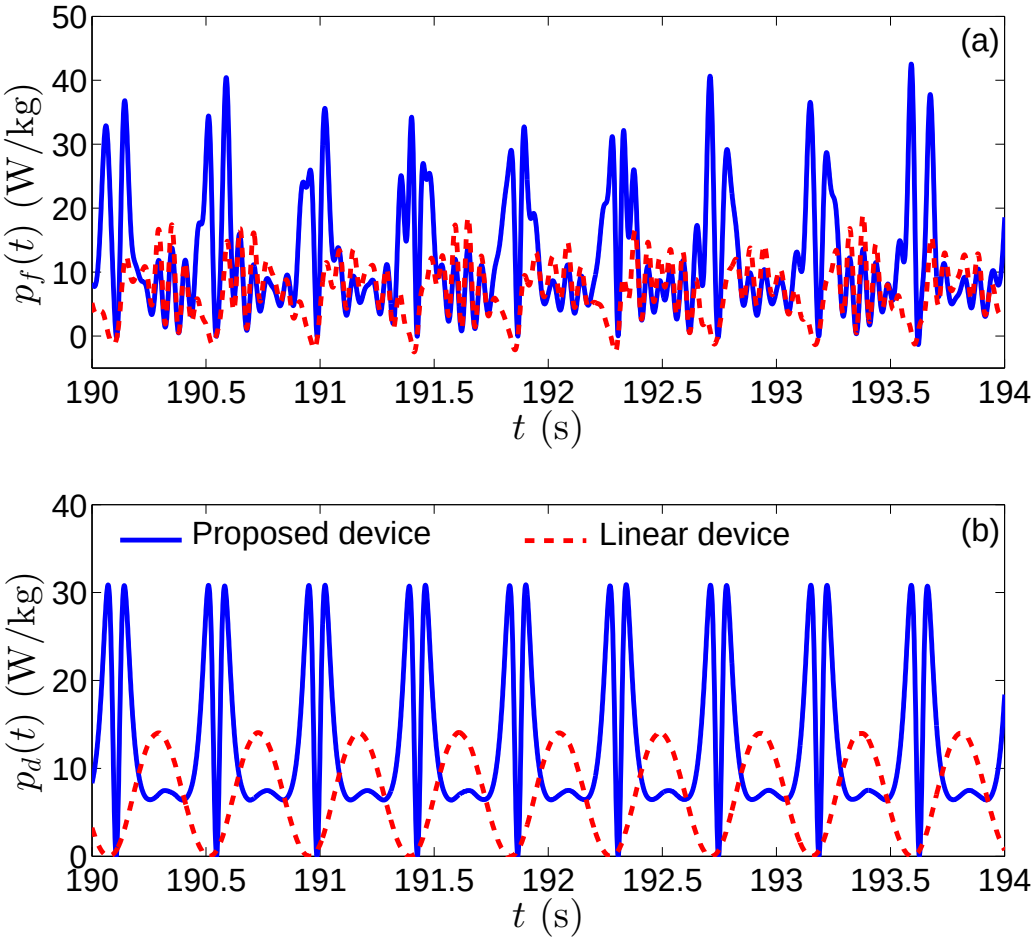

Figure 4.13: When the excitation contains high-order harmonic noise, time histories of (a) the instantaneous power of the excitation $p_f(t)$ and (b) the dissipated power $p_d(t)$ in the first example. Proposed device: $U(x) = 30x^2 - 180x^4 + 123x^6$; Linear device: $U(x) = 2(1.144\pi)^2x^2$.

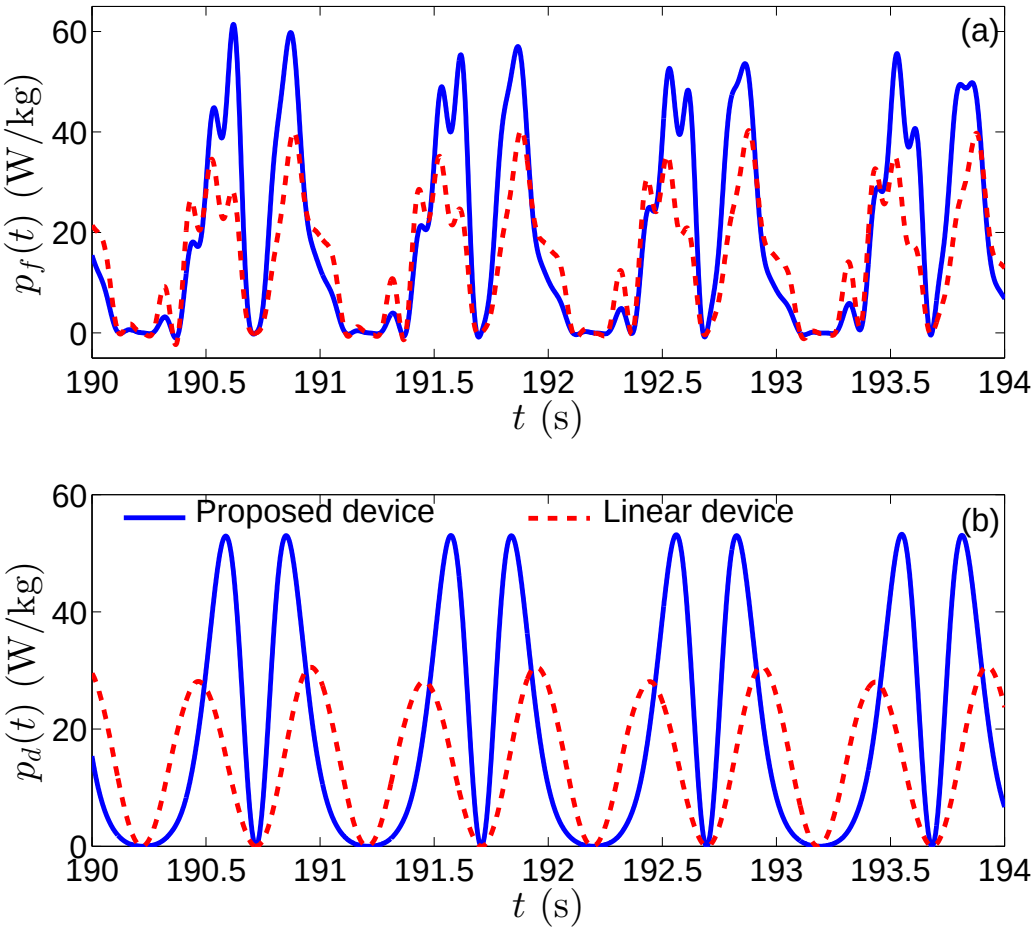

Figure 4.14: When the excitation contains high-order harmonic noise, time histories of (a) the instantaneous power of the excitation $p_f(t)$ and (b) the dissipated power $p_d(t)$ in the second example. Proposed device: $U(x) = 50x^2 + 16.5x^3$; Linear device: $U(x) = 2(1.013\pi)^2x^2$.

4.5 Concluding Remarks

In this chapter, the issues derived from the use of bandwidth and traditional "nonlinear resonance" in vibration energy harvesting have been addressed. It is noted that bandwidth is a relative parameter, and does not show the amount of energy harvested. It is thus not appropriate to use bandwidth to evaluate the performance of a device in vibration energy harvesting. In linear devices, as demonstrated, the broadened bandwidth is achieved by sacrificing the energy dissipation at the frequencies near resonance. The results have shown that widening the bandwidth of a linear device would offer benefits only when the natural frequency of the device cannot be designed around the dominating frequencies of an excitation. In nonlinear energy harvesting, relying on nonlinear approaches to obtain broadband performance may be misleading. Single frequency response curve shows that a nonlinear device can exhibit "broadband" performance. However, such "broadband" performance does not indicate that under multi-frequency excitation, the nonlinear device still has satisfactory performance because the principle of superposition does not apply. For the traditional "nonlinear resonance," the corresponding response usually has a large amplitude. Thus, the traditional "nonlinear resonance" is conventionally regarded as performing effectively and efficiently in energy harvesting. However, the results have shown that there exists a generalized resonance condition for linear and nonlinear systems, i.e. the global resonance condition, which sets the upper-bound device performance. For linear devices, the global resonance condition is simplified to be the linear resonance condition. For nonlinear systems, it has been shown that a device based on global resonance performs better than devices based on traditional "nonlinear resonance." However, it is noted that for nonlinear approaches, the resonance condition is more stringent. For passive methods, however, it may be impossible to design a nonlinear device matching a multi-frequency excitation such that the nonlinear global resonance condition is achieved. In practice,

active approaches may be required to reap the full potential offered by nonlinear global resonance.

Chapter 5

INVESTIGATION OF USING DYNAMICS ESCAPED FROM POTENTIAL WELL TO ENHANCE VIBRATIONAL ENERGY HARVESTING

It has been shown that a device with rigid-body architecture may be advantageous over those with the traditional material-deformation based architecture [7, 8, 78]. A device with rigid-body architecture does not rely on material deformation to provide mechanical stiffness. Thus, it is possible for the internal motion of the device to be directed into the region outside the potential well of the device dynamics. The resulting internal motion possesses a variety of dynamical properties [84, 85], which may be beneficial to harvesting energy from vibrations.

In this chapter, the potential of utilizing the dynamic behavior of a device having escaped from its potential well to enhance the energy harvesting performance is investigated. A pendulum-type device [78] under harmonic, parametrical excitation was used in this investigation. Only the period-one purely rotating orbits [85] were investigated.

5.1 Theoretical Analysis

Considering the cases of vertical and horizontal harmonic base excitations (i.e. the displacement $y_0(t)$ of the base is $y_0(t) = A\cos\Omega t$), the dimensionless governing equation

of a pendulum-type device (shown in Figure 2.1) can be written as

$$\ddot{\theta} + \gamma\dot{\theta} + \sin\theta = p\cos\omega\tau\sin(\theta + \alpha) \tag{5.1}$$

where $\alpha = 0$ and $\alpha = \pi/2$ represent vertical and horizontal excitations, respectively. θ is the angular displacement of the pendulum, ($\ddot{}$) and ($\dot{}$) denote, respectively, the first and second derivatives with respect to a scaled time variable defined as $\tau = \omega_n t$, $\omega = \Omega/\omega_n$, $p = A_e/g$ in which $A_e = A\Omega^2$, and $\gamma = 2\zeta_m + C_e/(\omega_n M\lambda)$ denotes the total damping with the intrinsic viscous mechanical damping ratio of the device ζ_m and the equivalent electrical damping coefficient $C_e = \frac{(2K_e/L)^2}{(r_w+R_L)}$, where $K_e = WK_wB_{mw}l_R\rho_w$, r_w and R_L are the internal resistance of the coil and the electrical load, respectively.

5.1.1 Exact Solution

For a period-one rotating orbit of a parametrically excited pendulum (Equation (5.1)), its angular velocity is equal to the frequency of the excitation with a small periodic perturbation with zero mean over one period [85–87]. Using the non-dimensional time variable τ defined previously, the angular velocity can be written as

$$\dot{\theta}(\tau) = \omega + \epsilon(\tau) \tag{5.2}$$

where $\epsilon(\tau)$ is a periodic function with small amplitude, which satisfies

$$|\epsilon(\tau)| << \omega \tag{5.3}$$

and

$$\int_{\tau_0}^{\tau_0+2\pi/\omega} \epsilon(\tau)\, d\tau = 0 \tag{5.4}$$

Due to the periodicity of the perturbation, using the Fourier series $\epsilon(\tau)$ can be represented as

$$\epsilon(\tau) = \sum_{k=1}^{\infty} \epsilon_k \cos(k\omega\tau + \varphi_k) \tag{5.5}$$

where coefficients ϵ_k and φ_k are the amplitude and phase of the kth harmonics of frequency $k\omega$, respectively.

Using Equations (5.2) and (5.5), the angular displacement can be readily obtained as

$$\theta(\tau) = \omega\tau + \varphi_0 + \epsilon_\theta \tag{5.6}$$

where φ_0 is the initial phase of $\theta(\tau)$, and

$$\epsilon_\theta = \sum_{k=1}^{\infty} C_k \sin(k\omega\tau + \varphi_k) \tag{5.7}$$

in which $C_k = \epsilon_k/(k\omega)$, thus

$$|\epsilon_\theta| < \frac{|\epsilon|}{\omega} << 1 \tag{5.8}$$

Note that based on the definition of the period-one rotation, Equation (5.6) represents the exact form of the solution. However, due to the infinite number of coefficients to be determined, i.e. ϵ_k, φ_k, φ_0, and the parametric term in the governing equation that generates beat frequencies, it is impossible to determine exactly the parameters by direct substitution and harmonic balance. Thus, an iterative method is used to approximately determine these parameters [86, 87].

5.1.2 Approximate Solution

5.1.2.1 Iterative Method

Substituting Equation (5.6) into the right-hand side of Equation (5.1) and expanding $\sin\theta$ and $\sin(\theta+\alpha)$ at $\epsilon_\theta = 0$ yield

$$\begin{aligned}\ddot{\theta} + \gamma\dot{\theta} =& p\cos\omega\tau\left[\sin(\omega\tau+\varphi_0+\alpha) + \cos(\omega\tau+\varphi_0+\alpha)\cdot\epsilon_\theta + O\left(\epsilon_\theta^2\right)\right] \\ &- \left[\sin(\omega\tau+\varphi_0) + \cos(\omega\tau+\varphi_0)\cdot\epsilon_\theta + O\left(\epsilon_\theta^2\right)\right]\end{aligned} \tag{5.9}$$

In this study, the following iterative process is used for the estimation of the parameters in Equation (5.6):

Step 1: The iteration starts with the zero-order approximation of θ such that $\sin\theta \approx \sin(\omega\tau+\varphi_0)$ and $\sin(\theta+\alpha) \approx \sin(\omega\tau+\varphi_0+\alpha)$. Equation (5.9) can be rewritten as

$$\ddot{\theta} + \gamma\dot{\theta} = p\cos\omega\tau\sin(\omega\tau+\varphi_0+\alpha) - \sin(\omega\tau+\varphi_0) \tag{5.10}$$

An approximate solution θ_1 can be obtained by substituting Equations (5.6) and (5.7) into Equation (5.10).

Step 2: Using the approximated parameters in Equation (5.9) and truncating the series at desired order, a modified equation of motion can be obtained and solved in combination of Equations (5.6) and (5.7).

... ...

Step n: Using the solution from the $(n-1)$th step and follow the same process in Step 2, the solution for the nth iteration can be obtained.

5.1.2.2 Under Vertical Excitation ($\alpha = 0$)

(1) First Iteration

The solution of Equation (5.10) with $\alpha = 0$ is

$$\theta_1 = \omega\tau + \varphi_{01} + \sum_{k=1}^{2} C_{1k} \sin\left(k\omega\tau + \varphi_{1k}\right) \tag{5.11}$$

where

$$\varphi_{01} = \pi - \arcsin\left(\frac{2\gamma\omega}{p}\right) \tag{5.12}$$

and

$$C_{1k} = \sqrt{{A_{1k}}^2 + {B_{1k}}^2}, \quad \varphi_{1k} = \arctan\frac{B_{1k}}{A_{1k}}, \quad k = 1, 2 \tag{5.13}$$

in which

$$\begin{aligned} A_{1k} &= \frac{R_{k1} + \frac{\gamma}{k\omega} R_{k2}}{\left(k\omega\right)^2 + \gamma^2}, \quad B_{1k} = \frac{\frac{\gamma}{k\omega} R_{k1} - R_{k2}}{\left(k\omega\right)^2 + \gamma^2} \\ R_{11} &= \cos\varphi_{01}, \quad R_{12} = -\sin\varphi_{01} \\ R_{21} &= -\frac{p}{2}\cos\varphi_{01}, \quad R_{22} = \frac{p}{2}\sin\varphi_{01} \end{aligned} \tag{5.14}$$

Note that $\sin\varphi_{01}$ is bounded in [-1,1]. Consequently, the necessary condition for the solution (5.11) to exist is

$$p \geq 2\gamma\omega \tag{5.15}$$

which gives a lower bound on the normalized excitation amplitude, p.

(2) Second Iteration

In the second iteration, using the result of the first iteration and considering the first-

order approximation, the following modified governing equation is obtained.

$$\begin{aligned}\ddot{\theta} + \gamma\dot{\theta} = &(p\cos\omega\tau - 1)\sin(\omega\tau + \varphi_{02}) \\ &+ (p\cos\omega\tau - 1)\cos(\omega\tau + \varphi_{02})\sum_{k=1}^{2} C_{1k}\sin(k\omega\tau + \varphi_{1k})\end{aligned} \tag{5.16}$$

which is solved as

$$\theta_2 = \omega\tau + \varphi_{02} + \sum_{k=1}^{4} C_{2k}\sin(i\omega\tau + \varphi_{2k}) \tag{5.17}$$

where

$$\varphi_{02} = \pi - \arcsin\left(\frac{2\gamma\omega}{\sqrt{K_1^2 + K_2^2}}\right) - \psi \tag{5.18}$$

and

$$\begin{aligned}&K_1 = p + A_{11} - \frac{pA_{12}}{2}, \quad K_2 = -B_{11} + \frac{pB_{12}}{2} \\ &\psi = \arctan\frac{K_2}{K_1} \\ &C_{2k} = \sqrt{{A_{2k}}^2 + {B_{2k}}^2}, \quad \varphi_{2k} = \arctan\frac{B_{2k}}{A_{2k}} \\ &k = 1, 2, 3, 4\end{aligned} \tag{5.19}$$

in which

$$A_{2k} = \frac{R_{k1} + \frac{\gamma}{k\omega}R_{k2}}{(k\omega)^2 + \gamma^2}, \quad B_{2k} = \frac{\frac{\gamma}{k\omega}R_{k1} - R_{k2}}{(k\omega)^2 + \gamma^2} \tag{5.20}$$

and

$$
\begin{aligned}
R_{11} &= \cos\varphi_{02} - \frac{pC_{11}}{4}\cos(\varphi_{11}+\varphi_{02}) + \frac{C_{12}}{2}\cos(\varphi_{12}-\varphi_{02}) \\
R_{12} &= -\sin\varphi_{02} + \frac{pC_{11}}{4}\sin(\varphi_{11}+\varphi_{02}) - \frac{C_{12}}{2}\sin(\varphi_{12}-\varphi_{02}) + \frac{pC_{11}}{2}\sin(\varphi_{11}-\varphi_{02}) \\
R_{21} &= -\frac{p}{2}\cos\varphi_{02} + \frac{C_{11}}{2}\cos(\varphi_{11}+\varphi_{02}) - \frac{pC_{12}}{2}\cos\varphi_{12}\cos\varphi_{02} \\
R_{22} &= \frac{p}{2}\sin\varphi_{02} - \frac{C_{11}}{2}\sin(\varphi_{11}+\varphi_{02}) + \frac{pC_{12}}{2}\sin\varphi_{12}\cos\varphi_{02} \\
R_{31} &= -\frac{pC_{11}}{4}\cos(\varphi_{11}+\varphi_{02}) + \frac{C_{12}}{2}\cos(\varphi_{12}+\varphi_{02}) \\
R_{32} &= \frac{pC_{11}}{4}\sin(\varphi_{11}+\varphi_{02}) - \frac{C_{12}}{2}\sin(\varphi_{12}+\varphi_{02}) \\
R_{41} &= -\frac{pC_{12}}{4}\cos(\varphi_{12}+\varphi_{02}) \\
R_{42} &= \frac{pC_{12}}{4}\sin(\varphi_{12}+\varphi_{02})
\end{aligned}
\tag{5.21}
$$

As $\sin(\varphi_{02}+\psi)$ is bounded in [-1,1], the necessary condition for the solution to exist is

$$\frac{2\gamma\omega}{\sqrt{K_1^2+K_2^2}} \leq 1 \tag{5.22}$$

Following a similar procedure, iterations with higher orders can be obtained.

5.1.2.3 Under Horizontal Excitation ($\alpha = \pi/2$)

(1) First Iteration

The solution of Equation (5.10) with $\alpha = \pi/2$ is

$$\theta_1 = \omega\tau + \varphi_{01} + \sum_{k=1}^{2} C_{1k}\sin(k\omega\tau + \varphi_{1k}) \tag{5.23}$$

where

$$\varphi_{01} = \arccos\left(\frac{2\gamma\omega}{p}\right) \tag{5.24}$$

and

$$C_{1k} = \sqrt{{A_{1k}}^2 + {B_{1k}}^2}, \quad \varphi_{1k} = \arctan \frac{B_{1k}}{A_{1k}}, \quad k = 1, 2 \tag{5.25}$$

in which

$$\begin{aligned} A_{1k} = \frac{-R_{k1} + \frac{\gamma}{k\omega} R_{k2}}{(k\omega)^2 + \gamma^2}, \quad B_{1k} = -\frac{\frac{\gamma}{k\omega} R_{k1} + R_{k2}}{(k\omega)^2 + \gamma^2} \\ R_{11} = -\cos\varphi_{01}, \quad R_{12} = -\sin\varphi_{01} \\ R_{21} = -\frac{p}{2}\sin\varphi_{01}, \quad R_{22} = \frac{p}{2}\cos\varphi_{01} \end{aligned} \tag{5.26}$$

Note that $\cos\varphi_{01}$ is bounded in [-1,1]. Consequently, the necessary condition for solution (5.23) to exist is

$$p \geq 2\gamma\omega \tag{5.27}$$

which gives a lower bound on the normalized excitation amplitude, p.

(2) Second Iteration

In the second iteration, using the result of the first iteration and considering the first-order approximation, the following modified governing equation is obtained.

$$\begin{aligned} \ddot{\theta} + \gamma\dot{\theta} = & p\cos\omega\tau\left[\cos\left(\omega\tau + \varphi_{02}\right) - \sin\left(\omega\tau + \varphi_{02}\right)\cdot\epsilon_{\theta_1}\right] \\ & - \left[\sin\left(\omega\tau + \varphi_{02}\right) + \cos\left(\omega\tau + \varphi_{02}\right)\cdot\epsilon_{\theta_1}\right] \end{aligned} \tag{5.28}$$

where $\epsilon_{\theta_1} = \sum_{k=1}^{2} C_{1k}\sin\left(k\omega\tau + \varphi_{1k}\right)$ is obtained from the first iteration.

Equation (5.28) is solved as

$$\theta_2 = \omega\tau + \varphi_{02} + \sum_{k=1}^{4} C_{2k}\sin\left(k\omega\tau + \varphi_{2k}\right) \tag{5.29}$$

where

$$\varphi_{02} = \arccos\left(\frac{2\gamma\omega}{\sqrt{K_1^2 + K_2^2}}\right) - \psi \tag{5.30}$$

and

$$K_1 = -A_{11} + \frac{pB_{12}}{2}, \quad K_2 = p - B_{11} - \frac{pA_{12}}{2}, \quad \psi = \arctan\frac{K_1}{K_2}$$
$$C_{2k} = \sqrt{{A_{2k}}^2 + {B_{2k}}^2}, \quad \varphi_{2k} = \arctan\frac{B_{2k}}{A_{2k}}, \quad k = 1, 2, 3, 4 \tag{5.31}$$

in which

$$A_{2k} = \frac{-R_{k1} + \frac{\gamma}{k\omega}R_{k2}}{(k\omega)^2 + \gamma^2}, \quad B_{2k} = -\frac{\frac{\gamma}{k\omega}R_{k1} + R_{k2}}{(k\omega)^2 + \gamma^2} \tag{5.32}$$

and

$$\begin{aligned}
R_{11} &= -\cos\varphi_{02} - \frac{pC_{11}}{4}\sin(\varphi_{11} + \varphi_{02}) - \frac{C_{12}}{2}\cos(\varphi_{12} - \varphi_{02}) \\
R_{12} &= -\sin\varphi_{02} + \frac{pC_{11}}{4}\cos(\varphi_{11} + \varphi_{02}) - \frac{C_{12}}{2}\sin(\varphi_{12} - \varphi_{02}) - \frac{pC_{11}}{2}\cos(\varphi_{11} - \varphi_{02}) \\
R_{21} &= -\frac{p}{2}\sin\varphi_{02} - \frac{C_{11}}{2}\cos(\varphi_{11} + \varphi_{02}) - \frac{pC_{12}}{2}\cos\varphi_{12}\sin\varphi_{02} \\
R_{22} &= \frac{p}{2}\cos\varphi_{02} - \frac{C_{11}}{2}\sin(\varphi_{11} + \varphi_{02}) - \frac{pC_{12}}{2}\sin\varphi_{12}\sin\varphi_{02} \\
R_{31} &= -\frac{pC_{11}}{4}\sin(\varphi_{11} + \varphi_{02}) - \frac{C_{12}}{2}\cos(\varphi_{12} + \varphi_{02}) \\
R_{32} &= \frac{pC_{11}}{4}\cos(\varphi_{11} + \varphi_{02}) - \frac{C_{12}}{2}\sin(\varphi_{12} + \varphi_{02}) \\
R_{41} &= -\frac{pC_{12}}{4}\sin(\varphi_{12} + \varphi_{02}) \\
R_{42} &= \frac{pC_{12}}{4}\cos(\varphi_{12} + \varphi_{02})
\end{aligned} \tag{5.33}$$

As $\cos(\varphi_{02} + \psi)$ is bounded in [-1,1], the necessary condition for the solution to exist is

$$\frac{2\gamma\omega}{\sqrt{K_1^2 + K_2^2}} \leq 1 \tag{5.34}$$

Following a similar procedure, higher-order iterations can be derived.

5.1.3 Power Output

Based on the period-one rotating solution (5.2), the average angular velocity of a pendulum in a period-one rotating orbit over one period is Ω. Thus, the effective value of the electromotive force is proportional to the excitation frequency, Ω, and

$$E = \frac{1}{\sqrt{2}} 2K_e\Omega. \tag{5.35}$$

The average electrical power delivered to the resistive load over one period, P_L , is

$$P_L = \frac{1}{2}\left(\frac{2K_e\Omega}{R_L + r_w}\right)^2 R_L \tag{5.36}$$

Equation (5.36) shows that the harvested power is neither dependent on the natural frequency of the device, nor on the intensity of the excitation. The power is proportional to the energy level of the orbit, characterized by the square of the rotating speed Ω. Excitations with higher frequencies direct the dynamics to orbits with higher energy levels, thus, more power can be harvested.

5.2 Experiments

5.2.1 Device and Experiment Setup

In the section of experiments, focus was placed on the case of vertical excitations. Figure 5.1 shows the schematic diagram of the device and the experiment setup. The device employed a mini pendulum as the coupling unit and an electromagnetic induction unit as the electrical generator. The mini pendulum had an equivalent length of L

= 5.95 cm and an equivalent mass of $M = 0.0129$ kg. The generator included a cylindrical rare-earth magnet as the rotor and two identical windings as the stator. The pendulum and the magnet were rigidly connected. The magnet was diametrically magnetized with a mass of 0.0241 kg, a radius of 6.35 mm and a length of $l_R = 2.54$ cm. The maximum magnetic flux density was measured at 0.549 T on the surface of the magnet. The two identical windings were orthogonally oriented and were respectively connected to a resistive load R_L with the same resistance. Such configuration, in the case of low frequencies where the effect of winding inductance can be neglected, ensured that the induced electromagnetic force was proportional to the angular velocity of the magnet. Thus, it could be modeled using equivalent viscous damping force [78]. The windings were fabricated using AWG #44 copper wire, each with nominally $W = 1200$ turns. The resistances, r_w, were measured at 680 ohms and 650 ohms for the two windings, respectively. The natural frequency and viscous damping ratio of the device were identified from free-vibration tests to be $\omega_n = 2.03$ Hz and $\zeta = 0.55\%$, respectively. The winding coefficient was calculated to be K_w =0.758 [78]. The centroid of the windings in the radial direction was measured at ρ_w =7.6 mm from the magnet surface, giving the equivalent magnetic flux density of $B_{mw} = 0.386$ T. The coefficient, $K_e = WK_wB_{mw}l_R\rho_w$ was calculated to be K_e =0.0664 V/(rad$\cdot s^{-1}$). The equipment used in this study included a digital-controlled vibration system (Model LW-126-13, Labworks Inc.), a digital phosphor oscilloscope (Model DPO 3040), and an electrical load circuit.

5.2.2 Bounds of Excitation Amplitude

The quadratic relationship shown in (5.36) is valid only within the stable zone of period-one rotations in the parameter space. In order to maintain a stable orbit, it is necessary that the energy of the excitation be bounded in a specific range[88–90]. The lower

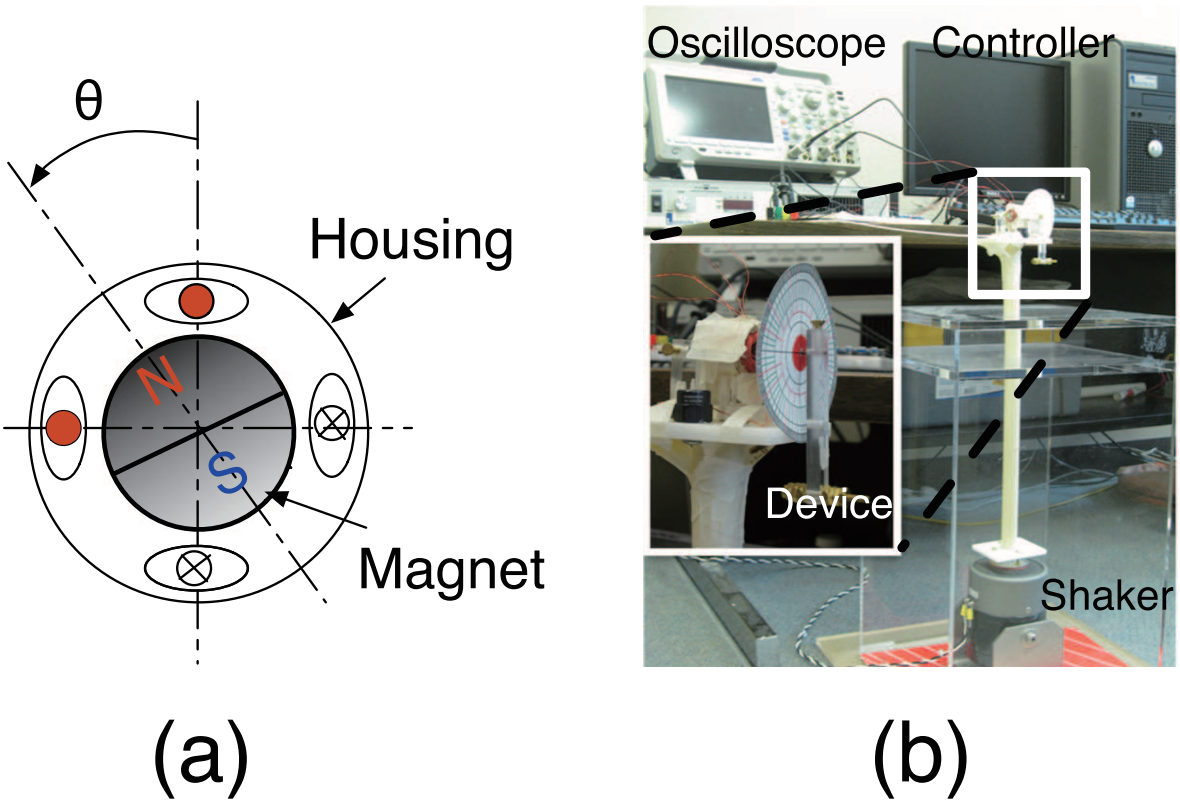

Figure 5.1: (a)Prototype Device and (b) Experiment Setup

bound prescribes the minimal energy level required to stabilize the orbit. Beyond the upper bound, the dynamics will leave the zone of period-one rotation. As shown in Equation (5.15), the lower bound can be approximately obtained as

$$p_{\min} = 2\gamma\omega \tag{5.37}$$

Analytical approximation of the upper bound is, however, difficult to obtain. Results of extensive numerical simulations, summarized in Figure 5.2, demonstrate that the lower bound can be predicted by (5.37) with satisfactory accuracy. The upper bound increases quadratically with the normalized frequency, ω. For systems with low levels of damping, e.g. $\gamma << 1$, the upper bound is almost invariant, which is orders of magnitude higher than the lower bound, indicating a relatively large stable zone of period-one rotating orbit. The same trend of the bounds was observed consistently for a large range of frequency, i.e. $1 < \omega \leq 500$. In all cases considered, $\omega > 1$ was necessary to maintain a stable period-one rotating orbit. Such a requirement indicates the possible existence of an absolute lower limit of $p > 2\gamma$. Equation (5.37) suggests that $\omega \leq p/(2\gamma)$, thus, for low-level vibrations, i.e p is small, the effectiveness of the proposed method is limited in a relatively low-frequency range.

5.2.3 Device Performance

In this study, harmonic excitations of amplitude $0.14g$, $0.18g$, and $0.22g$ were used in the experiments. Figure 5.3 shows the effect of the excitation frequency on the induced electromotive force and the power delivered to the resistive load (10 kΩ each winding). Experimental results shown in Figures 5.3(a) and 5.3(b) are consistent with the relationship expressed in equation (5.35); the induced electromotive force increased linearly with the excitation frequency. As can be seen from Figures 5.3(c) and 5.3(d), the relationship between the output power and the excitation frequency closely

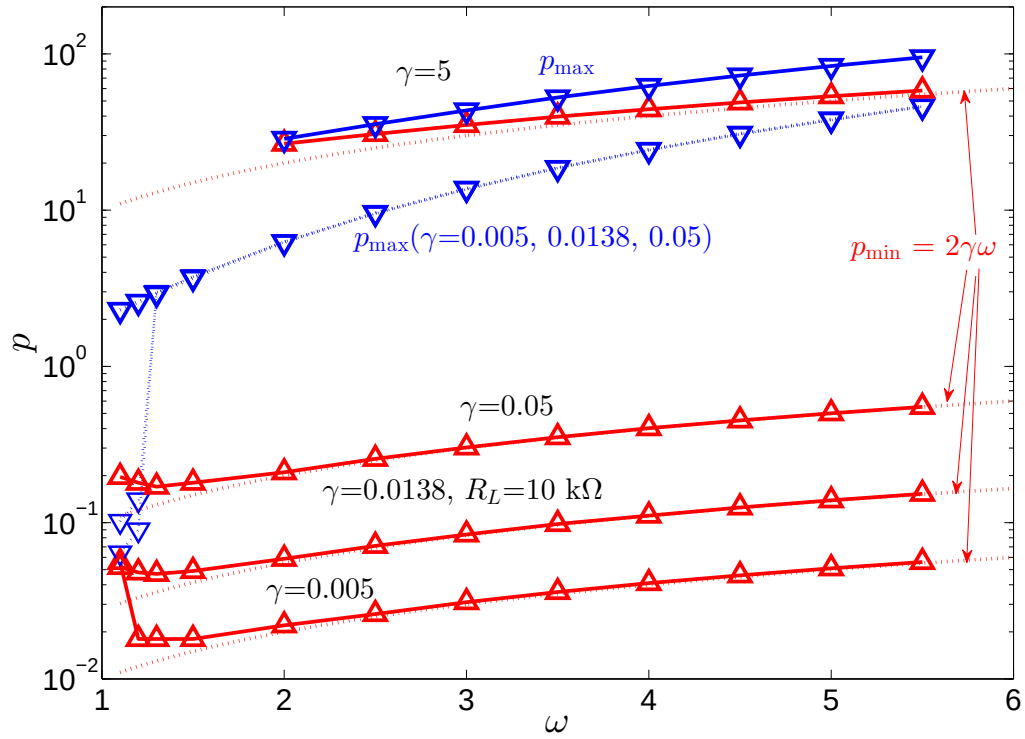

Figure 5.2: Bounds of excitation amplitude, p. Dotted: Theoretical (Equation (5.37)); Solid line with markers: Numerically calculated ($\triangle$:lower bound, $\bigtriangledown$: upper bound)

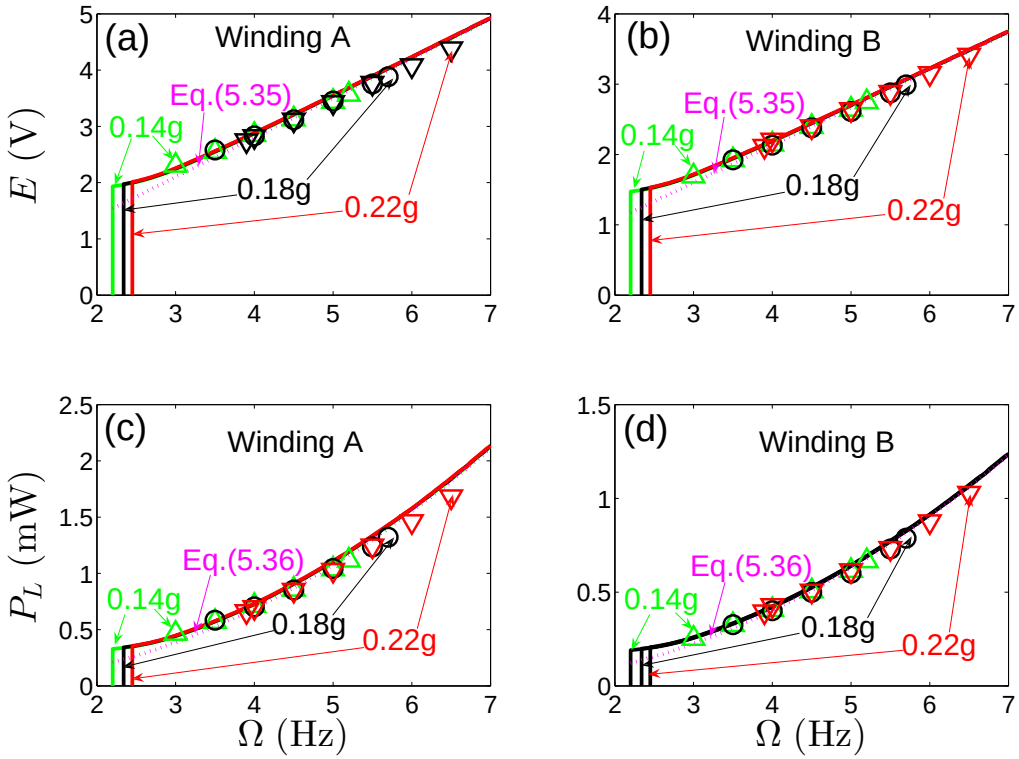

Figure 5.3: Frequency response of the device ($R_L = 10$ kΩ). Markers: Measured ($\triangle$: $0.14g$, $\bigcirc$: $0.18g$, $\triangledown$: $0.22g$); Solid lines: Numerically calculated; Dotted: Theoretical

followed equation (5.36). As the coils were fabricated manually, the actual values of the coefficient K_e were not identical for the two windings. They were identified to be K_{eA} = 0.07885 V/(rad·s^{-1}) for winding A and K_{eB} = 0.06005 V/(rad·s^{-1}) for winding B. Using the identified values, numerical simulations were performed, the results of which are also presented in Figure 5.3. It is seen that the results from numerical simulation, theoretical prediction, and experiment are in excellent agreement. Also, as indicated by equations (5.35) and (5.36), the amplitude of the excitation did not effect the power generated. The lower and upper limits of the excitation frequency were found to be 2.20 Hz/10.28 Hz, 2.34 Hz/13.23 Hz, and 2.45 Hz/16.18 Hz for excitations of 0.14g, 0.18g, and 0.22g, respectively (Figure 5.2). Due to the limitation of the capacity of the equipment, the lowest and highest frequencies achieved in experiments were 3.0 Hz/5.2 Hz, 3.5 Hz/5.7 Hz, and 3.9 Hz/6.5 Hz for the three excitations respectively.

Figure 5.4 shows the load characteristics of the device under the excitations of 0.14g, 0.18g, and 0.22g at 4 Hz. Figures 5.4(a) and 5.4(b) show the relationship between the effective values of voltage and current of the two windings, respectively. Figures 5.4(c) and 5.4(d) show the average power delivered to the electrical loads. Results from measurements were found to be consistent with those from numerical simulation and theoretical prediction. The theoretical results are not shown as they were identical to those from numerical simulation. The relationships shown in Figures 5.4(a) and 5.4(b) resemble those of a constant voltage source. With various electrical load, the effective values of voltage remained almost constant at 2.933 V for winding A and 2.234 V for winding B. Again, these values were independent of the amplitude of the excitations (Equation (5.35)). For the two larger excitations, i.e. 0.18g and 0.22g, the optimal load resistances were found to be the same, at 690 ohms for winding A and at 660 ohms for winding B, corresponding to the optimal values of output power of 3.1 mW for winding A and 1.8 mW for winding B. For the excitation of 0.14g, the electrical power increased monotonically with the electrical load until 1,000 ohms, beyond which

the dynamics escaped the stable zone of period-one rotation and entered the region of oscillation. The maximum power was measured at 2.8 mW and 1.6 mW for Winding A and Winding B, respectively. The results shown in Figures 5.4(c) and 5.4(d) also indicate that increasing the excitation intensity may improve the load capacity of the device but may not increase the output power. The maximum electrical loads for the three excitations i.e. 1,000 ohms, 600 ohms, and 300 ohms, respectively correspond to the maximum total system damping of 0.0290, 0.0347, and 0.0420. These values are consistent with the lower bounds of p shown in Figure 5.2. The independent relationship between power and excitation amplitude was further demonstrated by exciting the device at three frequencies, i.e. 4 Hz, 4.5 Hz, and 5 Hz, respectively with a range of amplitudes. The electrical load was fixed at 10 kΩ for each winding. The results, along with those from numerical simulations, are summarized in Figure 5.5. Identical to those from numerical simulations, the theoretical results are omitted. The intensities of these excitations were within the bounds ($0.06g \leq A_e \leq 9.60g$) shown in Figure 5.2, thus, the rotating orbits were stable, leading to the constant power output. It is noted that due to fabrication errors, nonlinearity of the magnet, and other structural uncertainties in the device, the two windings were not identical as expected. The voltages generated by the two windings were noticeably different. The discrepancy in voltage was amplified in the calculation of power, e.g. the optimal power of winding A was almost twice as much as that of Winding B. Such discrepancy implies existence of nonlinearity in equivalent damping force in Equation (5.1). However, the excellent agreement of the results from theoretical analysis, numerical simulation, and experiments demonstrates that the effect of such nonlinearity on the dynamics of the device may be negligible.

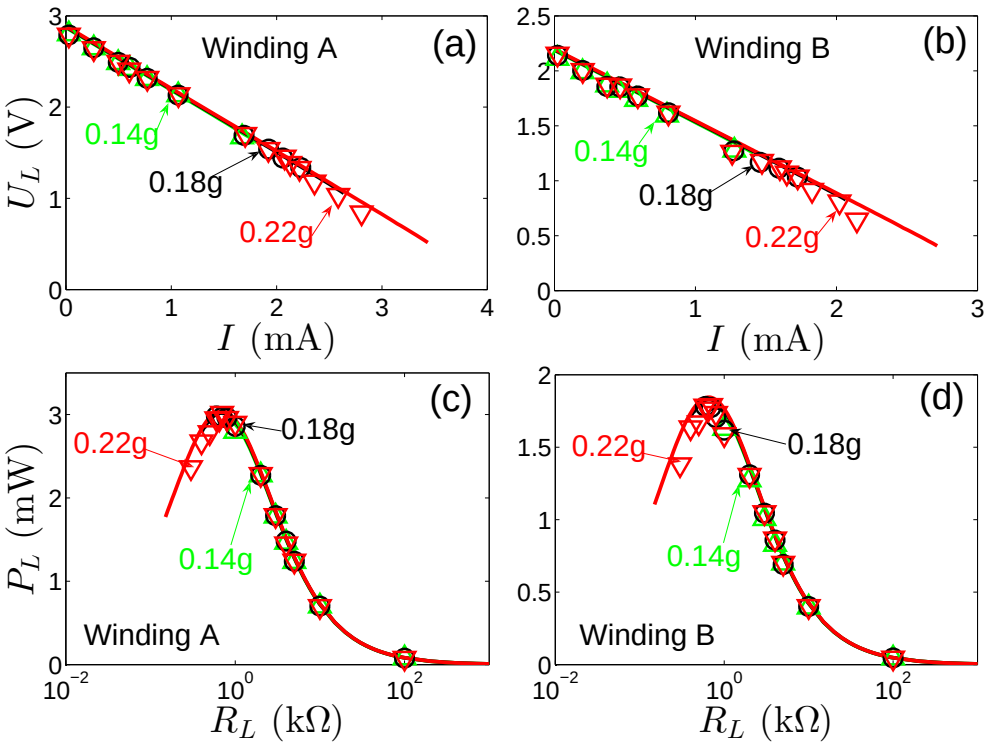

Figure 5.4: Load characteristics of harvester at 4Hz. Markers: Measured (△: $0.14g$, ◯: $0.18g$, ▽: $0.22g$); Solid lines: Numerically calculated

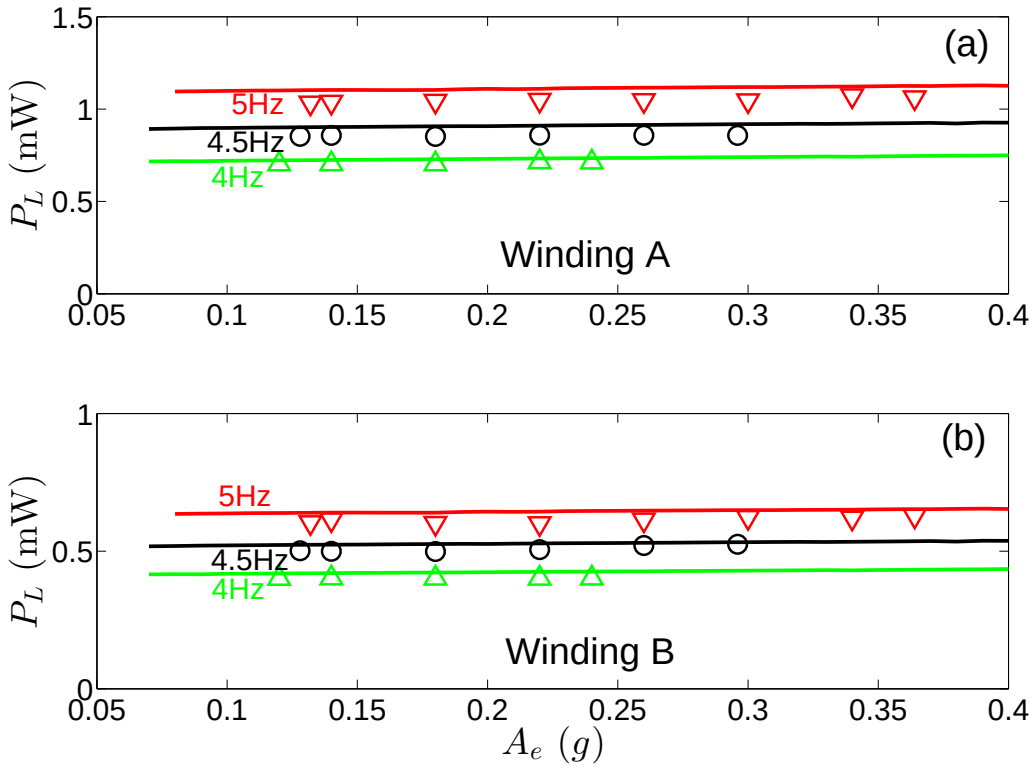

Figure 5.5: Effect of excitation intensity on output power ($R_L = 10$ kΩ). Markers: Measured; Solid lines: Numerically calculated

5.3 Concluding Remarks

In this chapter, the potential benefits of utilizing dynamics outside the potential well to enhance energy harvesting was demonstrated. Resonance is no longer a requirement for high mechanical coupling. In the cases considered, once the device dynamics is in the orbit of period-one rotation, the harvested power is proportional to the energy level of the orbit. It is neither dependent on the natural frequency nor on the intensity of the excitation. As the energy level of the orbit is proportional to the square of the excitation frequency, more power can be harvested at higher frequencies. It is noted that stable period-one rotating orbits, whose approximated solutions have been obtained through the method of Iterative Harmonic Balance, exist within a stable zone in the parameter space. In particular, for a specific level of excitation, the approximated solutions have shown that there is an upper limit of the excitation frequency, i.e. $\omega < p/(2\gamma)$, thus, for applications of low-level vibrations, the effectiveness of utilizing the period-one rotating orbits is limited in relatively low frequencies. As there exists a rich spectrum of dynamics outside the potential well [84], if there are mechanisms to deliver the device dynamics from one orbit to another, it is then possible to design an active device that utilizes a small portion of the collected energy to adjust the device dynamics in response to non-stationary ambient energy source so that the dynamics is kept outside the potential well for as long as possible; the total collected energy is thus expected to be greatly increased.

Chapter 6

EFFECTS OF NON-RESISTIVE CIRCUITS ON THE PERFORMANCE OF VIBRATORY ENERGY HARVESTER

In vibratory energy harvesting, purely resistive circuits have been conventionally considered to evaluate the device performance in the majority of the existing efforts. Compared with resistive circuits, the effects of non-resistive circuits on vibratory energy harvesting have largely remained unexplored. Because the characteristics of non-resistive circuits are different compared to those of resistive circuits, resulting in different effects of electromechanical coupling on a harvester, the device performance based on resistive loads may not be generalized for applications based on non-resistive circuits. For a resistive load, its electromechanical effect can usually be simplified as an equivalent viscous damping, which may not be true for a non-resistive load. In this chapter, the effects of non-resistive circuits on the dynamics of a vibratory energy harvester were investigated. Three types of non-resistive loads, namely a resistive load with a rectifier, a resistive load with a rectifier and a regulating capacitor, and a simple charging circuit (i.e. a capacitor-charging circuit consisting of a rectifier and a capacitor), were considered.

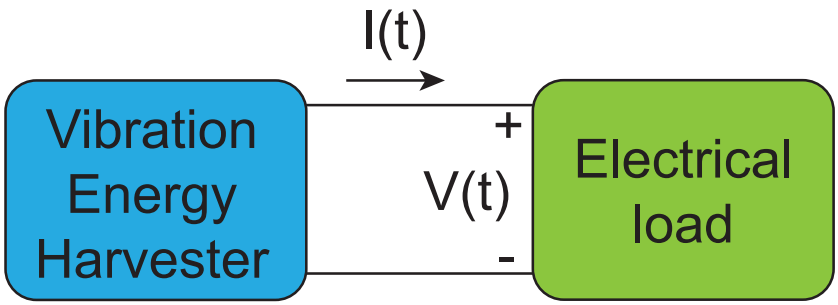

Figure 6.1: Schematic diagram of a vibratory energy harvester with electrical load.

6.1 Theoretical Analysis

Let's consider a vibratory energy harvester, including electromagnetic and piezoelectric. The governing equation of dynamics for the system with electrical load (Figure 6.1) can be generally written as

$$m\ddot{x} + c_m\dot{x} + k(x) + \kappa y = F(x,t), \tag{6.1a}$$

$$\alpha\dot{y} + \chi y + \vartheta = \kappa\dot{x}, \tag{6.1b}$$

where x denotes the displacement of the seismic mass m, c_m the linear mechanical damping coefficient, $k(x)$ the restoring force, κ the linear electromechanical coupling coefficient, and $F(x,t)$ denotes the general external force, including parametrical excitations. For inductive devices, α, χ, y, and ϑ represent the inductance L_w and internal resistance R_w of the winding, the induced current $I(t)$, and the voltage across the electrical load $V(t)$, respectively. For capacitive ones, they represent the capacitance C_p and internal conductance of the piezoelectric element, the induced voltage $V(t)$ and the current through the electrical load $I(t)$, respectively. Since the internal conductance of the piezoelectric element is small enough to be ignored, the term with respect to χ is omitted in the performance analysis of capacitive harvesters.

6.1.1 Resistive Loads

For a resistive load, $\vartheta = \beta y$ where β is the load resistance for electromagnetic harvester and the load conductance for piezoelectric harvester. For low-frequency excitations, the electromechanical coupling, shown in Equation(6.1b), could be approximated to an algebraic relationship if $\alpha << \chi + \beta$, i.e. $(\chi + \beta)y = \kappa\dot{x}$. The reverse effect of the electromechanical coupling on the system dynamics can be calculated as $\kappa y = \frac{\kappa^2}{\chi+\beta}\dot{x}$, which is equivalent to additional damping in device dynamics shown in Equation (6.1a). The governing equation of device dynamics can be rewritten as

$$m\ddot{x} + (c_m + c_e)\dot{x} + k(x) = F(x,t), \tag{6.2}$$

where $c_e = \frac{\kappa^2}{\chi+\beta}$ is the equivalent electrical damping. It indicates that in this case, the performance of a vibration energy harvester under low-frequency excitations could be evaluated based on the damping mechanism.

6.1.2 Non-Resistive Loads

If the electrical load is not a resistive load, the reverse effect of the electromechanical coupling may have influence not only on system damping but also on the natural frequency of a harvester. Here, three basic cases (Figure6.2) are considered: (I) a resistive load with a full-bridge rectifier, (II) a resistive load with a full-bridge rectifier and a regulating capacitor C_r, and (III) a simple charging circuit consisting of a full-bridge rectifier and an energy storing element (e.g. capacitor and battery). Because of the voltage drop of the full-bridge rectifier V_r, in all three cases considered, there is current (i.e. $I(t) \neq 0$) flowing into electrical loads only when the rectifier is turned on. Otherwise, $I(t) = 0$.

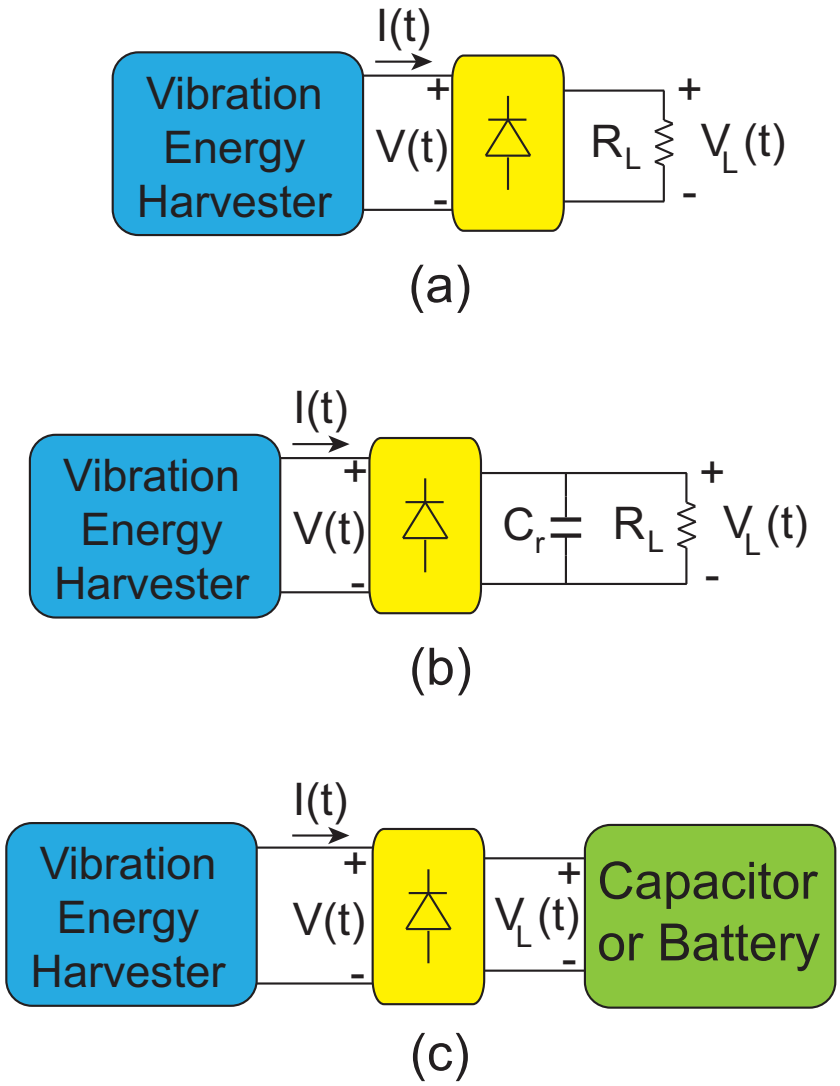

Figure 6.2: Three basic types of non-resistive load considered, (a) Resistive load with a full-bridge rectifier, (b) Resistive load with a full-bridge rectifier and a regulating capacitor C_r, and (c) the simplest charging circuit consisting of a full-bridge rectifier and an energy storing element (e.g. capacitor and battery).

6.1.2.1 Electromagnetic vibration energy harvester

For an electromagnetic harvester, the variables y and ϑ in Equation (6.1b) are $y = I(t)$, and $\vartheta = V(t)$.

- (I) A resistive load with a full-bridge rectifier

  When $|V(t)| < V_r$, $I(t) = 0$ (i.e. $\kappa y = 0$) and $V(t) = \kappa\dot{x}$. When $|V(t)| \geq V_r$ (i.e. $I(t) \neq 0$), based on the circuit shown in Figure 6.2(a), the relationship of $V(t)$ to the voltage drop of the rectifier and the induced current can be calculated to be $V(t) = R_L I(t) + V_r \text{sgn}(I(t))$, where $\text{sgn}(y)$ is the signum function defined as,

$$\text{sgn}(y) = \begin{cases} 1, & y > 0 \\ 0, & y = 0 \\ -1, & y < 0. \end{cases} \tag{6.3}$$

  Substituting $V(t) = R_L I(t) + V_r \text{sgn}(I(t))$ into Equation (6.1b), one obtains $L_w \dot{I}(t) + (R_w + R_L) I(t) + V_r \text{sgn}((t)) = \kappa\dot{x}$. For low-frequency excitation and $L_w << R_w + R_L$, the induced current can be approximately expressed as $I(t) = \frac{\kappa}{R_w+R_L}\dot{x} - \frac{V_r}{R_w+R_L}\text{sgn}(I(t)) = \frac{\kappa}{R_w+R_L}\dot{x} - \frac{V_r}{R_w+R_L}\text{sgn}(\dot{x})$ because $\text{sgn}(I(t)) = \text{sgn}(\dot{x})$. The reverse effect of the electromechanical coupling on the system dynamics can be obtained as

$$\kappa y = \kappa I(t) = \frac{\kappa^2}{R_w + R_L}\dot{x} - \frac{\kappa V_r}{R_w + R_L}\text{sgn}(\dot{x}). \tag{6.4}$$

The governing equation of the system dynamics can be derived as

$$\begin{cases} \begin{cases} m\ddot{x} + c_m\dot{x} + k(x) = F(x,t), \\ V(t) = \kappa\dot{x}, \end{cases} & |V(t)| < V_r \\ \begin{cases} m\ddot{x} + (c_m + c_e)\dot{x} - \frac{\kappa V_r}{(R_w+R_L)}\mathrm{sgn}(\dot{x}) + k(x) = F(x,t), \\ V(t) = \frac{R_L}{R_w+R_L}\kappa\dot{x} + \frac{R_w}{R_w+R_L}V_r\mathrm{sgn}(\dot{x}), \end{cases} & |V(t)| \geq V_r \end{cases} \tag{6.5}$$

where $c_e = \frac{\kappa^2}{R_w+R_L}$. Equation (6.5) shows that for an electromagnetic device, the presence of the rectifier reduces the damping contributed by the electrical resistance, but has no effect on the natural frequency of the system. When the rectifier is off, the system is in the open-circuit state, and thus no energy dissipated by the resistance. When the rectifier is turned on, the reverse effect of the electromechanical coupling contains two terms: the equivalent electrical damping, which is due to the resistance, and the equivalent dry friction, i.e. $-\frac{\kappa V_r}{(R_w+R_L)}\mathrm{sgn}(\dot{x})$, resulted from the voltage drop of the rectifier, as shown in Equation (6.4). Such negative dry friction reduces the effects of the equivalent electrical damping on the system dynamics. Because of the voltage drop of the rectifier, the voltage across the resistance is reduced, and thus the output current of the device, leading to less energy harvested than that from a pure resistor. Since the reverse effect of the electromechanical coupling is proportional to the output current of the device, the reduced output current leads to reduction of the reverse effect of the electromechanical coupling, and thus reducing the system damping. For a linear device, smaller damping results in larger system response and more narrow bandwidth.

- (II) A resistive load with a full-bridge rectifier and a regulating capacitor

When the rectifier is off, $I(t) = 0$ (i.e. $\kappa y = 0$), $V(t) = \kappa\dot{x}$, and $V_L(t) = V_L(t_0)e^{-\frac{1}{R_L C_r}(t-t_0)}$ in which $V_L(t_0)$) is the voltage across the regulating capacitor when the regulating capacitor starts to discharge at the time t_0. When the rectifier is turned on (i.e. $I(t) \neq 0$), $C_r\dot{V}_L + \frac{V_L}{R_L} = I(t)\text{sgn}(I(t))$, and $V(t) = (V_L + V_r)\text{sgn}(I(t) = (V_L(t) + V_r)\,\text{sgn}(\dot{x})$. In such a situation, the governing equation of the system dynamics is derived to be

$$\begin{cases} \begin{cases} m\ddot{x} + c_m\dot{x} + k(x) = F(x,t) \\ V(t) = \kappa\dot{x} \qquad\qquad\qquad |V(t)| < V_r + V_L(t_0) \\ V_L(t) = V_L(t_0)e^{-\frac{1}{R_L C_r}(t-t_0)} \end{cases} \\ \\ \begin{cases} m\ddot{x} + c_m\dot{x} + k(x) + \left(\kappa C_r\dot{V}_L + \frac{\kappa}{R_L}V_L\right)\text{sgn}(\dot{x}) = F(x,t) \\ L_w C_r\ddot{V}_L + \left(\frac{L_w}{R_L} + R_w C_r\right)\dot{V}_L + \left(1 + \frac{R_w}{R_L}\right)V_L = \kappa|\dot{x}| - V_r \quad |V(t)| \geq V_r + V_L(t_1) \\ V(t) = (V_L(t) + V_r)\,\text{sgn}(\dot{x}) \end{cases} \end{cases} \tag{6.6}$$

where t_1 is the time instant when the rectifier is turned on. Equation (6.6) shows that when the rectifier is off, the system has the same dynamical equation as that at case (I); when the rectifier is turned on, the regulating capacitor and the inductance of the winding builds up an LC circuit. The natural frequency and damping ratio of the LC circuit can be calculated as

$$\omega_{n_{LC}} = \sqrt{\frac{1 + \frac{R_w}{R_L}}{L_w C_r}}, \tag{6.7a}$$

$$\xi_{LC} = \frac{\frac{L_w}{R_L} + R_w C_r}{2\sqrt{L_w C_r\left(1 + \frac{R_w}{R_L}\right)}}. \tag{6.7b}$$

It is noticed that the energy stored in the regulating capacitor cannot be trans-

ferred back to the device due to the rectifier, and is ultimately dissipated by the resistor. Actually, the rectifier obstructs the establishment of a complete electrical oscillation, reducing its effect on device properties (e.g. natural frequency). Since the resistor is connected to the regulating capacitor in parallel, the equivalent impedance of the electric load is smaller than that of case (I), resulting in much more output current, and thus more power delivered to the resistor. The increase of output current also indicates an enhanced reverse effect of the electromechanical coupling, leading to smaller device response than that of case (I).

- (III) The simplest charging circuit

  When the rectifier is switched off, $I(t) = 0$, $V(t) = \kappa\dot{x}$, and $V_L(t) = V_L(t_0)$ in which $V_L(t_0)$) is the voltage across the capacitor when the rectifier is off at the time instant t_0. When the rectifier is switched on (i.e. $I(t) \neq 0$), $V_L(t) = V_L(t_1) + \frac{1}{C_s}\int_{t_1}^{t} |I(t)|\mathrm{dt}$ where t_1 is the beginning time at which the storing capacitor C_s starts to be charged, and $V(t) = (V_L + V_r)\mathrm{sgn}(I(t)) = (V_L(t) + V_r)\,\mathrm{sgn}(\dot{x})$. In this situation, the governing equation of the system dynamics is derived as

$$\begin{cases} \begin{cases} m\ddot{x} + c_m\dot{x} + k(x) = F(x,t) \\ V(t) = \kappa\dot{x} \qquad\qquad |V(t)| < V_r + V_L(t_0) \\ V_L(t) = V_L(t_0) \end{cases} \\ \\ \begin{cases} m\ddot{x} + c_m\dot{x} + k(x) + \kappa C_s\dot{V}_L\mathrm{sgn}(\dot{x}) = F(x,t) \\ L_w C_s\ddot{V}_L + R_w C_s\dot{V}_L + V_L = \kappa|\dot{x}| - V_r \qquad |V(t)| \geq V_r + V_L(t_1) \\ V(t) = (V_L(t) + V_r)\,\mathrm{sgn}(\dot{x}) \end{cases} \end{cases} \tag{6.8}$$

From Equation (6.8), it can be seen that when the rectifier is off, the governing equation of the system is the same as those of cases (I) and (II). When the rectifier is switched on, because of the effect of the rectifier, the induced electricity is saved in the storing capacitor. As more energy stored in the capacitor, shown by the increasing voltage across it, the system response gradually settled at the open-circuit state. The ultimate voltage across the capacitor equals to the voltage amplitude of the device at open circuit minus the voltage drop of the rectifier.

6.1.2.2 Piezoelectric vibration energy harvester

For a piezoelectric harvester, in Equation (6.1b), $y = V(t)$, and $\vartheta = I(t)$.

- (I) A resistive load with a full-bridge rectifier

  When $|V(t)| < V_r$, $I(t) = 0$, and $V(t) = \frac{\kappa}{C_p}x$, contributing an additional stiffness, i.e. $\frac{\kappa^2}{C_p}x$, to the system. When $|V(t)| \geq V_r$, based on the circuit shown in Figure 6.2(a), the relationship of $I(t)$ to the voltage drop of the rectifier and the induced voltage can be calculated to be $I(t) = \frac{1}{R_L}V(t) - \frac{V_r}{R_L}\text{sgn}(V(t))$. Substituting this relationship into Equation (6.1b) can obtain $C_p\dot{V}(t)+\frac{1}{R_L}V(t)-\frac{V_r}{R_L}\text{sgn}(V(t)) = \kappa\dot{x}$. For low-frequency excitation and $C_p << \frac{1}{R_L}$, the induced voltage can be approximated as $V(t) = \kappa R_L\dot{x} + V_r\text{sgn}(V(t))$. Since $\text{sgn}(V(t)) = \text{sgn}(\dot{x})$, $V(t) = \kappa R_L\dot{x} + V_r\text{sgn}(\dot{x})$. The reverse effect of the electromechanical coupling on the system dynamics can be derived as

  $$\kappa V(t) = \kappa^2 R_L\dot{x} + \kappa V_r\text{sgn}(\dot{x}). \tag{6.9}$$

  Equation (6.9) shows that the reverse effect of the electromechanical coupling can be identical to be an additional damping and a dry friction. The governing

equation of system dynamics can be written as

$$\begin{cases} \begin{cases} m\ddot{x} + c_m\dot{x} + k(x) + \frac{\kappa^2}{C_p}x = F(x,t), \\ V(t) = \frac{\kappa}{C_p}x, \end{cases} & |V(t)| < V_r, \\ \begin{cases} m\ddot{x} + \left(c_m + c_e + \frac{\kappa V_r}{|\dot{x}|}\right)\dot{x} + k(x) = F(x,t), \\ V(t) = \kappa R_L\dot{x} + V_r\mathrm{sgn}(\dot{x}), \end{cases} & |V(t)| \geq V_r. \end{cases} \tag{6.10}$$

where the equivalent electrical damping $c_e = \kappa^2 R_L$. Equation (6.10) shows that for a piezoelectric device, the natural frequency depends on the combination of two cases, i.e. $|V(t)| < V_r$ and $|V(t)| \geq V_r$. Note that the system stiffness at $|V(t)| < V_r$ is greater than that at $|V(t)| \geq V_r$, while the increase of the voltage drop V_r enlarges the duration of the system at $|V(t)| < V_r$, increasing the system stiffness and thus the natural frequency. When $|V(t)| \geq V_r$, besides the additional damping c_e due to the resistance R_L, the voltage drop of the rectifier also contributes a dry friction to the system. Hardening stiffness combined with the dry friction lead to the decrease of the system response. For a piezoelectric harvester, the system response with the electrical load in case (I) is thus smaller than that with pure resistive load.

- (II) A resistive load with a full-bridge rectifier and a regulating capacitor
  When the rectifier is switched off, $I(t) = 0$, $V(t) = \frac{\kappa}{C_p}x$, and $V_L(t) = V_L(t_0)e^{-\frac{1}{R_L C_r}(t-t_0)}$ in which $V_L(t_0)$) is the voltage across the regulating capacitor when the regulating capacitor starts to discharge at the time t_0. When the rectifier is switched on, $I(t) = C_r\dot{V}(t) + \frac{1}{R_L}V(t) - \frac{V_r}{R_L}\mathrm{sgn}(V(t))$. The governing equation of system

dynamics in this situation can be derived as

$$\begin{cases} \begin{cases} m\ddot{x} + c_m\dot{x} + k(x) + \frac{\kappa^2}{C_p}x = F(x,t) \\ V(t) = \frac{\kappa}{C_p}x & |V(t)| < V_r + V_L(t_0), \\ V_L(t) = V_L(t_0)e^{-\frac{1}{R_L C_r}(t-t0)} \end{cases} \\ \\ \begin{cases} m\ddot{x} + c_m\dot{x} + k(x) + \kappa\left(V_L + V_r\right)\mathrm{sgn}(\dot{x}) = F(x,t) \\ (C_p + C_r)\dot{V}_L + \frac{1}{R_L}V_L = \kappa|\dot{x}| & |V(t)| \geq V_r + V_L(t_1), \\ V(t) = (V_L + V_r)\,\mathrm{sgn}(\dot{x}) \end{cases} \end{cases} \tag{6.11}$$

where t_1 is the time instant when the rectifier is turned on. Comparing Equation (6.11) to (6.10), it can be found that when the rectifier is turned off, the system at cases (I) and (II) has the same stiffness, but the duration at case (II) is longer than that at case (I) because of the voltage across the regulating capacitor, resulting in the increase of the global stiffness of the system. When the rectifier is turned on, in case (II), the presence of the regulating capacitor parallel connected to the resistance reduces the impedance of the electrical load, resulting in reduction of the voltage across the electrical load, and thus the power delivered to the resistance and the output voltage of the device $V(t)$. The reduced output voltage of the device decreases the reverse effect of the electromechanical coupling, leading to the increase of the system response. Therefore, the system at case (II) has a higher natural frequency and larger response, but less power output, as compared to that at case (I).

- (III) The simplest charging circuit

  When the rectifier is off, $I(t) = 0$, $V(t) = \frac{\kappa}{C_p}x$, and $V_L(t) = V_L(t_0)$ in which $V_L(t_0)$) is the voltage across the capacitor when the rectifier is turned off at the

time t_0. When the rectifier is on, $V(t) = (V_L + V_r)\,\mathrm{sgn}(V(t)) = (V_L + V_r)\,\mathrm{sgn}(\dot{x})$, and $I(t) = C_s\dot{V}_L\mathrm{sgn}(V(t)) = C_s\dot{V}_L\mathrm{sgn}(\dot{x})$ because of $\mathrm{sgn}(V(t)) = \mathrm{sgn}(\dot{x})$, in which C_s is the capacitor for storing the energy harvested. The governing equation of system dynamics can be obtained as

$$\begin{cases} \begin{cases} m\ddot{x} + c_m\dot{x} + k(x) + \frac{\kappa^2}{C_p}x = F(x,t) \\ V(t) = \frac{\kappa}{C_p}x \qquad\qquad |V(t)| < V_r + V_L(t_0) \\ V_L(t) = V_L(t_0) \end{cases} \\ \\ \begin{cases} m\ddot{x} + c_m\dot{x} + k(x) + \kappa V(t) = F(x,t) \\ V_L = V_L(t_1) + \frac{\kappa}{C_p+C_s}\int_{t_1}^{t} |\dot{x}|\mathrm{dt} \qquad |V(t)| \geq V_r + V_L(t_1). \\ V(t) = (V_L + V_r)\,\mathrm{sgn}(\dot{x}) \end{cases} \end{cases} \tag{6.12}$$

where $V_L(t_1)$ is the voltage across the capacitor C_s when the capacitor starts to be charged at the time t_1. From Equation 6.12, it can be seen that the simplest charging circuit only has an effect on the system stiffness. When the rectifier is turned off, the system has the stiffness at the state of open circuit, which is the same as those at cases (I) and (II). When the rectifier is turned on, the capacitor C_s starts to be charged, softening the system stiffness. As more electrical energy is stored in the capacitor, shown by the increasing voltage across it, the system response finally settled at the open-circuit state. The ultimate voltage across the capacitor equals to the voltage of the piezoelectric harvester at open circuit minus the voltage drop of the rectifier.

6.2 Results and Discussion

To verify the theoretical analysis, the numerical investigation was conducted using the MathWorks Simscape^{TM}. Here, we place focus on the effects of the electrical loads on the device dynamics and performance, so only linear devices are considered. For a linear electromagnetic harvester, the system has the parameters of $m = 12.9 \times 10^{-3}$ kg, $c_m = 0.0812$ N·s/m, $k'(0) = 319.48$ N/m, $\kappa = 6.712$ N/A, $\alpha = L_w = 0.1$ mH, and $\chi = R_w = 700\Omega$. Based on the parameters given, the natural frequency and mechanical damping ratio of the device can be calculated to be $\omega_n = 25$ Hz and $\xi_m = 0.02$, respectively. For a linear piezoelectric harvester, the parameters of the system are $m = 10.3 \times 10^{-3}$ kg, $c_m = 0.6296$ N·s/m, $k'(0) = 5983.9$ N/m, $\kappa = 0.0129$ N/V, and $\alpha = C_p = 58.99$ μF. The natural frequency of the system is identified to be $\omega_{n_{oc}} = 146.73$ Hz at the open circuit and $\omega_{n_{sc}} = 121$ Hz at the short circuit. The mechanical damping ratio of the system is calculated to be $\xi_m = 0.04$. During the numerical study for both electromagnetic and piezoelectric harvesters, the excitation amplitude was fixed at $0.5g$ where g is the gravitational acceleration.

6.2.1 Electromagnetic vibration energy harvester

The load characteristics of the electromagnetic harvester was first investigated. The excitation frequency was fixed at 25 Hz which was the natural frequency of the electromagnetic harvester. Three types of electrical loads, such as a resistor with a parallel capacitor, a resistor with a full-bridge rectifier, and a resistor with a full-bridge rectifier and a regulating capacitor, were considered. The results from numerical studies for these three cases are summarized in Figures 6.3, 6.4, and 6.5, respectively. Note that the parallel capacitor reduced the impedance of the electrical load, causing the decrease of the optimal resistive load. Moreover, increasing the parallel capacitor reduced the

current through the resistive load R_L, resulting in the decrease of the power delivered to the resistive load. When the parallel capacitor was up to a certain value, e.g. $C_r = 1$ mF, the system was close to the short-circuit state, while the power delivered to the resistive load could be ignored compared to the input power of the excitation, as shown in Figure 6.3. Figure 6.4 presents the effect of a rectifier on the load characteristics of the device. Because of the rectifier acting as a negative dry friction, increasing its voltage drop was beneficial for decreasing the electrical damping. However, increasing the voltage drop also reduced the voltage across the resistive load. Thus, the rectifier caused the increase of device response and the decrease of the power delivered to the resistive load, but no effect on the optimal resistive load of the device. It can be seen that the maximum power delivered to the resistive load was reduced from 2.707 mW to 1.090 mW as the voltage drop increased from 0 V to 1.6 V. Figure 6.5 shows the effect of a regulating capacitor combined with a rectifier on the load characteristics of the device. Because of the presence of the rectifier, increasing the regulating capacitor resulted in the increase of the optimal resistive load, i.e. $R_{L_{opt}}$ increasing from 1300 Ω to 2000 Ω as C_r increased from 0 mF to 1 mF; while the related maximum power delivered to the resistive load only had a little decrease (Figure 6.5(c)).

The frequency-response performance of the electromagnetic harvester was then evaluated. The same electrical loads in the test of load characteristics were considered. The resistive load R_L was fixed at 1300 Ω. Figure 6.6 shows the effect of a resistive load with a parallel capacitor on the frequency-response performance of the device. Since the parallel capacitor had the effect on the electrical impedance, increasing the parallel capacitor lead to the decreasing of the output voltage of the device, and thus reducing the power delivered to the resistive load. In addition, it can be seen that although the capacitor and the inductance established an LC circuit, increasing the parallel capacitor only slightly changed the natural frequency of the device because in the cases considered, the oscillating effect of the LC circuit was small enough to be

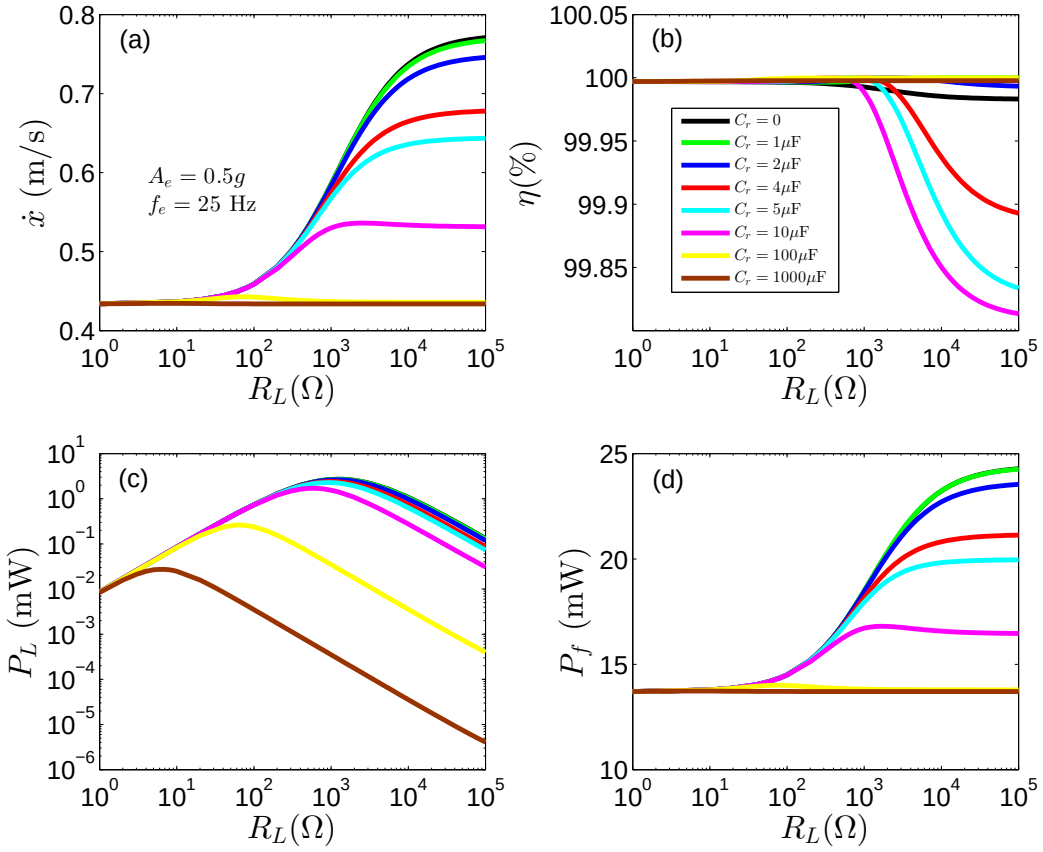

Figure 6.3: Effects of a parallel capacitor on load characteristics of an electromagnetic harvester under the excitation of $A_e = 0.5g$ and $f_e = 25$Hz: (a) Velocity $\dot{x}$, (b) Work efficiency of the excitation $\eta = \frac{\int_0^{\frac{2\pi}{\omega}} F(x,t)\dot{x}\mathrm{dt}}{\int_0^{\frac{2\pi}{\omega}} |F(x,t)\dot{x}|\mathrm{dt}}$ where ω is the excitation frequency, (c) Average power delivered to the resistance P_L, and (d) Average input power of the excitation P_f.

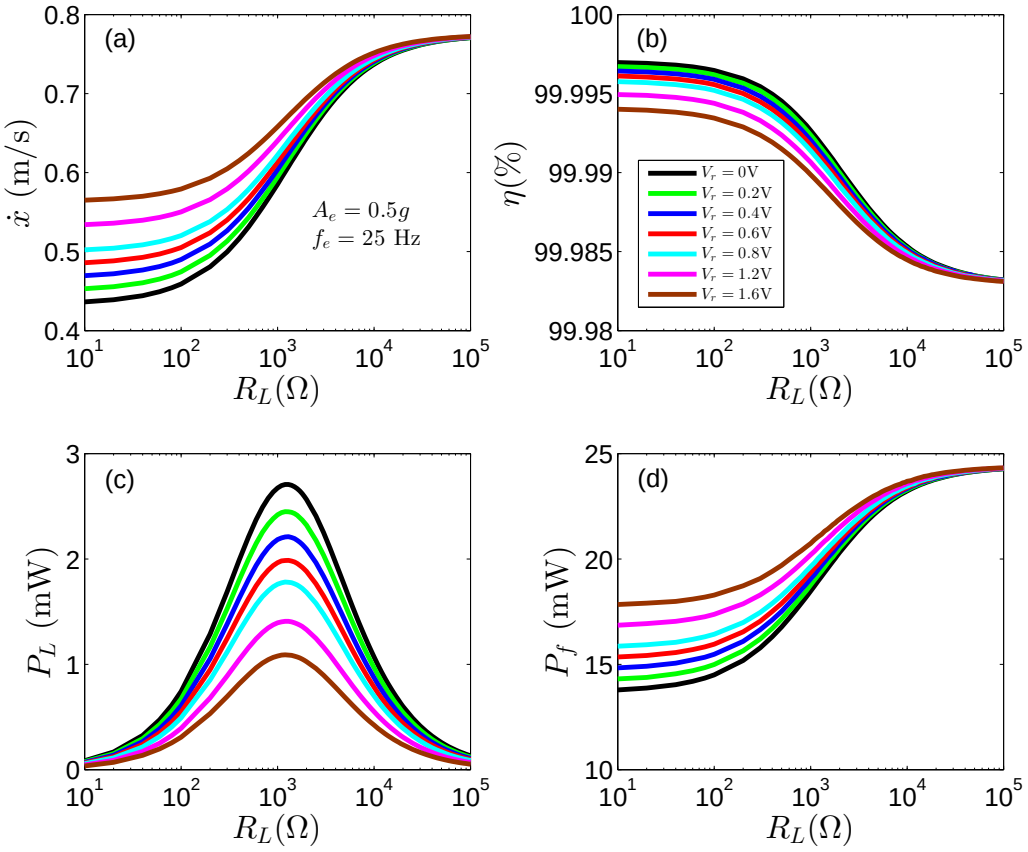

Figure 6.4: Effects of a full-bridge rectifier on load characteristics of an electromagnetic harvester under the excitation of $A_e = 0.5g$ and $f_e = 25$Hz: (a) Velocity $\dot{x}$, (b) Work efficiency of the excitation $\eta = \frac{\int_0^{\frac{2\pi}{\omega}} F(x,t)\dot{x}\mathrm{dt}}{\int_0^{\frac{2\pi}{\omega}} |F(x,t)\dot{x}|\mathrm{dt}}$ where ω is the excitation frequency, (c) Average power delivered to the resistance P_L, and (d) Average input power of the excitation P_f.

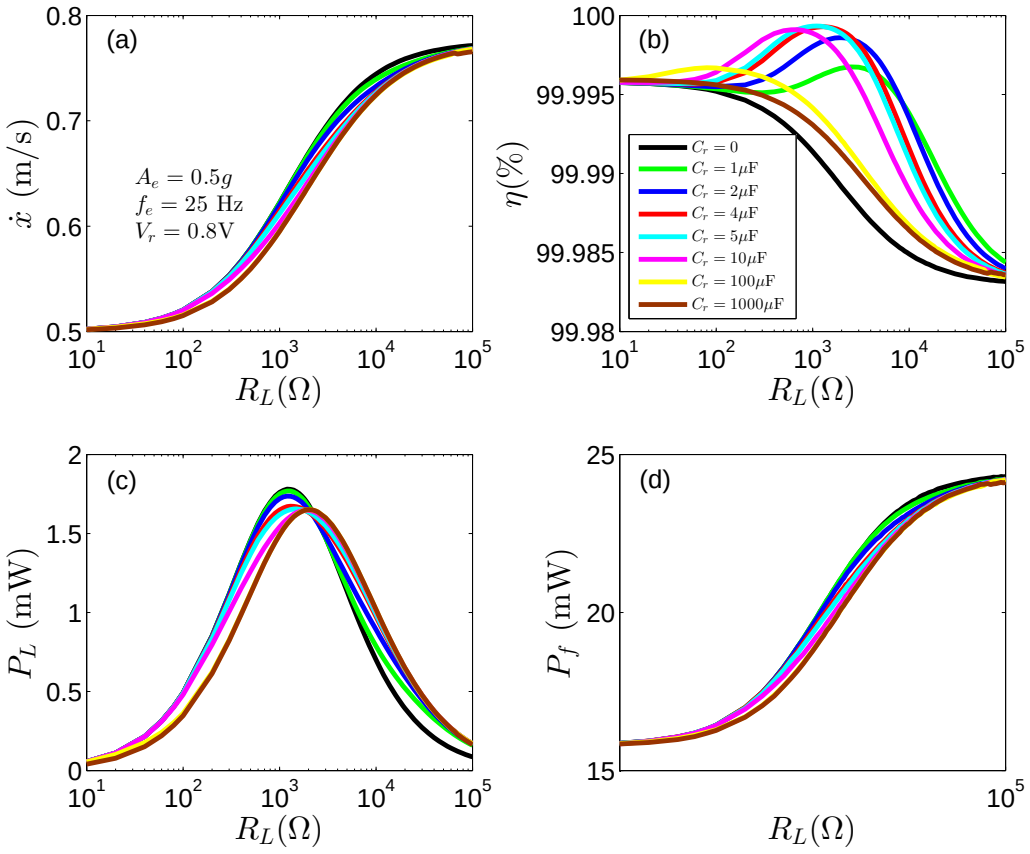

Figure 6.5: Effects of a parallel capacitor with a full-bridge rectifier on load characteristics of an electromagnetic harvester under the excitation of $A_e = 0.5g$ and $f_e = 25$Hz: (a) Velocity $\dot{x}$, (b) Work efficiency of the excitation $\eta = \frac{\int_0^{\frac{2\pi}{\omega}} F(x,t)\dot{x}\mathrm{dt}}{\int_0^{\frac{2\pi}{\omega}} |F(x,t)\dot{x}|\mathrm{dt}}$ where ω is the excitation frequency, (c) Average power delivered to the resistance P_L, and (d) Average input power of the excitation P_f.

ignored. From Equations (6.7a) and (6.7b), the natural frequency and damping of the LC circuit were calculated to be $\omega_{n_{LC}} = 19741$ Hz to 624.27 Hz and $\xi_{LC} = 28.22$ to 892.33 when the parallel capacitor increased from 1 μF to 1000 μF. Because $\xi_{LC} >> 1$, the LC circuit was over-damped system and could be approximated to be a first-order system. If the oscillating effect of the LC circuit played a significant role, however, the LC circuit could dramatically change the frequency-response performance of the device. Consider an unrealistic example, such as $L_w = 0.003$ H, $C_r = 0.003$ F, and $R_w = 0.2\ \Omega$. The natural frequency and damping ratio of the LC circuit was calculated to be $\omega_{n_{LC}} = 54.06$ Hz and $\xi_{LC} = 0.1$. Figure 6.7 shows that the under-damped LC circuit exhibited a strong effect on the device dynamics. The entire system displayed two dynamical modes which were distributed at 7.33 Hz and 181 Hz, respectively. These two mode frequencies were different to the mechanical natural frequency $\omega_n = 25$ Hz and the natural frequency of the LC circuit $\omega_{n_{LC}} = 54.06$ Hz. Besides establishing the LC circuit, as shown in Equation (6.6), the capacitor also played a role of damping. However, it is noted that the capacitor is not an energy dissipating unit. The energy stored on the capacitor was transferred back to the mechanical system. Such energy transfer between the two subsystems, i.e. mechanical and electrical, could be the cause of the observed significant change of the frequencies.

Figure 6.8 summarizes the results from frequency-response tests of an electromagnetic harvester with a resistive load and a full-bridge rectifier (case (I)). It can be seen that the voltage drop could increase the device response (Figure 6.8(a)), but reduced the power delivered to the resistive load significantly (Figure 6.8(c)), because the voltage drop caused the decrease of the voltage across the resistive load, leading to the decrease of the output current of the device, and thus weakening the reverse effect of the electromechanical coupling. When the voltage drop increased from 0V to 1.6V, the maximum power delivered to the resistive load was reduced from 2.721 mW to 1.1 mW, with 59.6% reduction. Therefore, the output power obtained from pure resistance

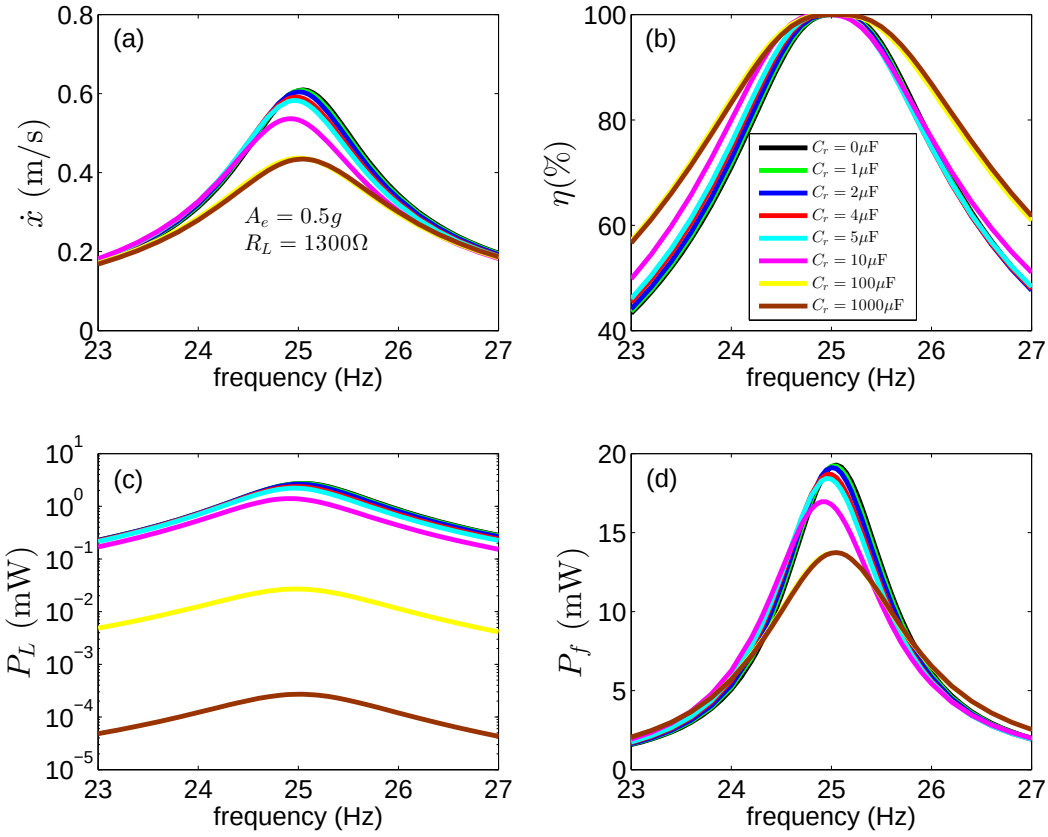

Figure 6.6: Effects of a parallel capacitor on single frequency-response performance of an electromagnetic harvester with a resistive load ($R_L = 1300\Omega$): (a) Velocity $\dot{x}$, (b) Work efficiency of the excitation $\eta = \frac{\int_0^{\frac{2\pi}{\omega}} F(x,t)\dot{x}\mathrm{dt}}{\int_0^{\frac{2\pi}{\omega}} |F(x,t)\dot{x}|\mathrm{dt}}$ where ω is the excitation frequency, (c) Average power delivered to the resistance P_L, and (d) Average input power of the excitation P_f.

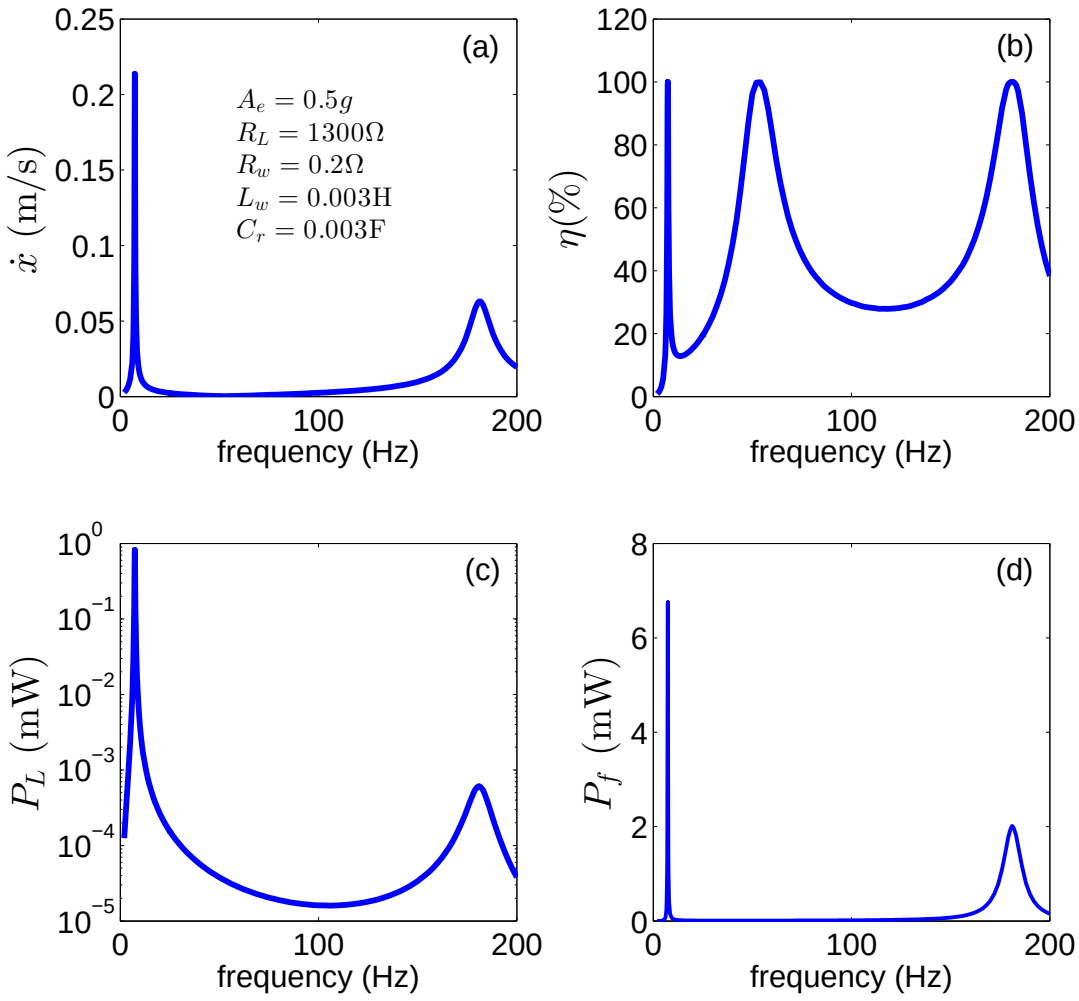

Figure 6.7: Effects of a parallel capacitor on single frequency-response performance of an electromagnetic harvester with a resistive load ($R_L = 1300\Omega$): (a) Velocity $\dot{x}$, (b) Work efficiency of the excitation $\eta = \frac{\int_0^{\frac{2\pi}{\omega}} F(x,t)\dot{x}\text{dt}}{\int_0^{\frac{2\pi}{\omega}} |F(x,t)\dot{x}|\text{dt}}$ where ω is the excitation frequency, (c) Average power delivered to the resistance P_L, and (d) Average input power of the excitation P_f. The parameters of the electrical elements were $L_w = 0.003\text{H}$, $C_r = 0.003\text{F}$, and $R_w = 0.2\Omega$.

overestimated that obtained from the electrical load shown in case (I). Figure 6.8 also shows that the rectifier had no effect on the natural frequency of the device.

Figure 6.9 shows the effects of a regulating capacitor on the frequency-response performance of the electromagnetic harvester. The voltage drop of the rectifier was fixed at 0.8 V. For comparison, the results regarding the system without the regulating capacitor are also presented. As predicted by the theoretical analysis, the presence of the regulating capacitor in parallel connection reduced the impedance of the electrical load, causing more current through the electrical load than that of case (I). The increase of the output current indicated the strengthening of the reverse effect of the electromechanical coupling, equaling to the increase of the system damping, which lead to the decrease of the system response as shown in Figure 6.9(a). Because of the decrease of the device response, the output voltage of the electromagnetic harvester was reduced. Combined the reduced output voltage with the reduced impedance, thus, the voltage across the resistive load was reduced, leading to the decrease of the power delivered to the resistive load (Figure 6.9(c)). Although the regulating capacitor and the inductance of the winding constructed an LC circuit, its effect on the resonance frequency of the system was not exhibited because of the high damping ratio of the LC circuit and the one-way properties of the rectifier for electrical energy transfer.

Figure 6.10 shows the effects of charging circuit on the performance of the electromagnetic device. The excitation frequency was fixed at 25 Hz. Three capacitors were employed, i.e. C_s = 5 mF, 10 mF, and 50 mF. It can be seen that before the voltage across the capacitor reached to the final value, the response of the harvester was transient and non-stationary. As more energy stored in capacitors (i.e. the increase of the voltage across it), the device response gradually settled at the final open-circuit state even the three capacitors had different capacitance. At the open-circuit state, the voltage across capacitors equaled to the amplitude of the open-circuit voltage of the harvester minus the voltage drop of the rectifier, i.e. $V_{L_{ult}} = 4.42$ V. When the voltage

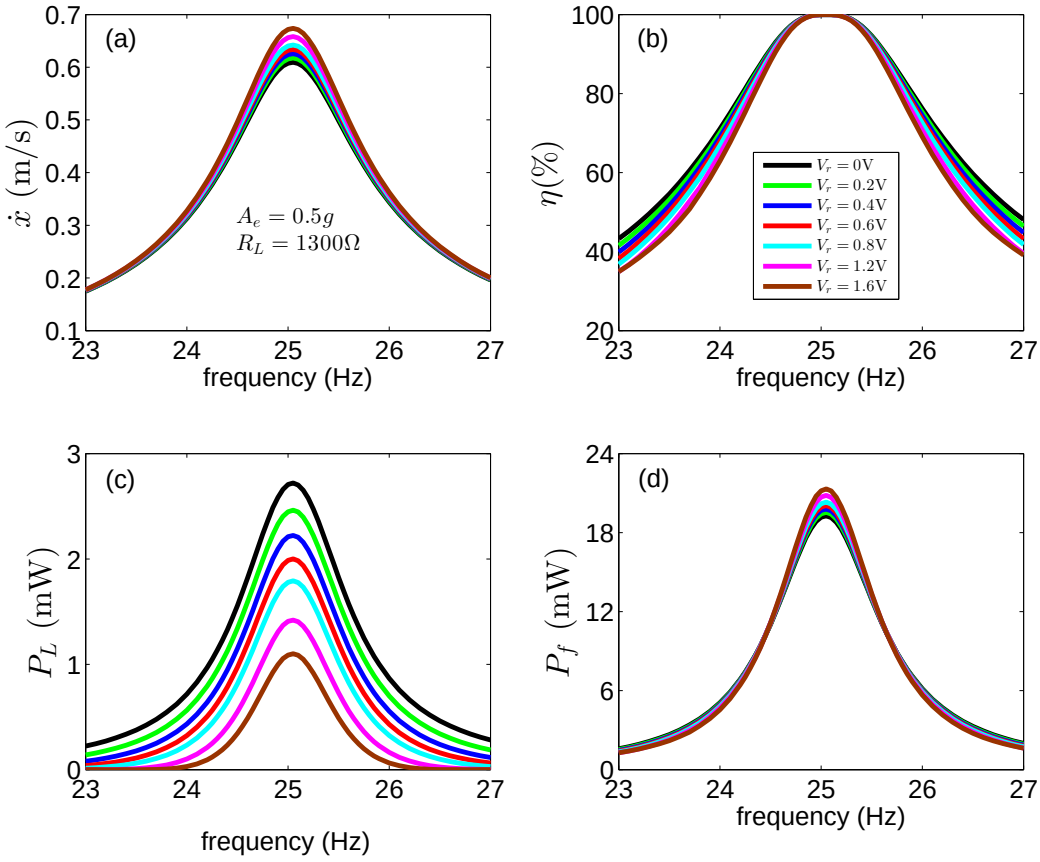

Figure 6.8: Effects of a full-bridge rectifier on single frequency-response performance of an electromagnetic harvester with a resistive load ($R_L = 1300\Omega$): (a) Velocity $\dot{x}$, (b) Work efficiency of the excitation $\eta = \frac{\int_0^{\frac{2\pi}{\omega}} F(x,t)\dot{x}\mathrm{dt}}{\int_0^{\frac{2\pi}{\omega}} |F(x,t)\dot{x}|\mathrm{dt}}$ where ω is the excitation frequency, (c) Average power delivered to the resistance P_L, and (d) Average input power of the excitation P_f.

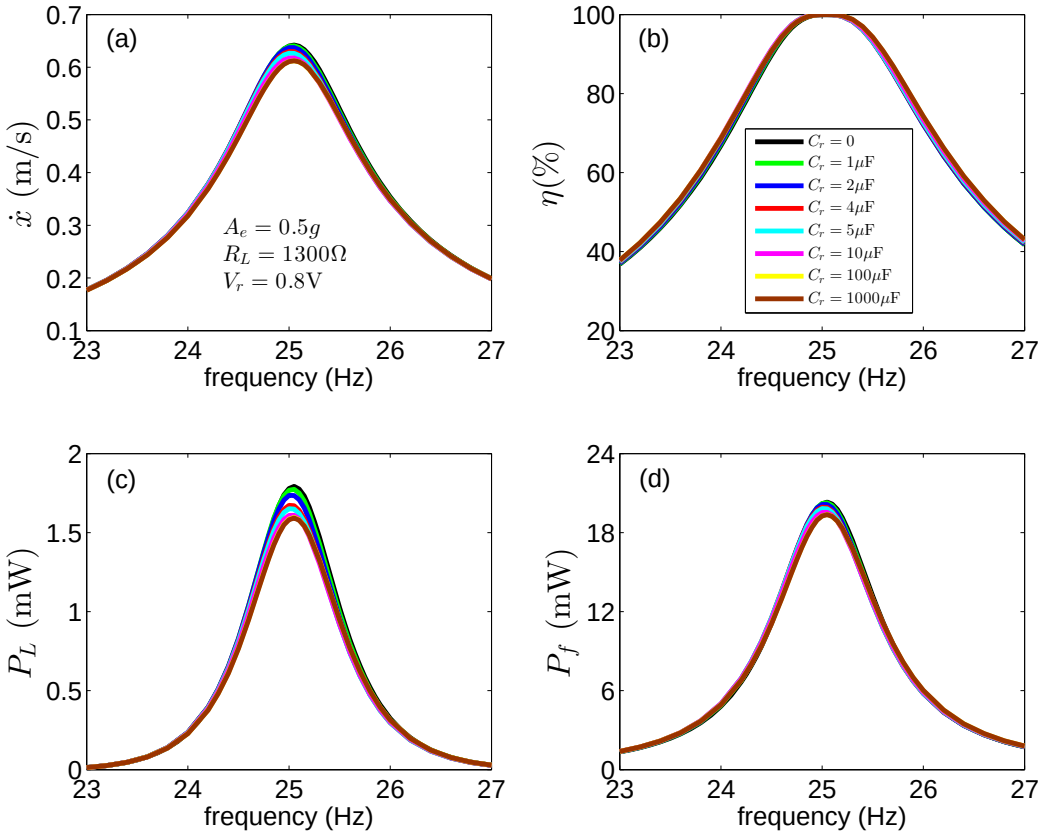

Figure 6.9: Effects of a parallel capacitor with a full-bridge rectifier on single frequency-response performance of an electromagnetic harvester with a resistive load ($R_L = 1300\Omega$): (a) Velocity $\dot{x}$, (b) Work efficiency of the excitation $\eta = \frac{\int_0^{\frac{2\pi}{\omega}} F(x,t)\dot{x}\text{dt}}{\int_0^{\frac{2\pi}{\omega}} |F(x,t)\dot{x}|\text{dt}}$ where ω is the excitation frequency, (c) Average power delivered to the resistance P_L, and (d) Average input power of the excitation P_f.

across the capacitors was charged to be 99% of the ultimate voltage, the ratio of the charging time for these three capacitors (i.e. $t_{10mF} : t_{5mF} : t_{1mF}$) was 9.74 : 4.88 : 1, which was smaller than the ratio of the capacitance values, i.e. 10 : 5 : 1. The related average power was calculated to be 0.3265 mW for $C_s = 1$ mF, 0.336 mW for $C_s = 5$ mF, and 0.3343 mW for $C_s = 10$ mF, respectively.

6.2.2 Piezoelectric vibration energy harvester

The load characteristics of a piezoelectric harvester was first investigated. The excitation frequency was fixed at 121 Hz which was the same to $\omega_{n_{sc}}$ of the device. Three types of electrical loads used in the load test of the electromagnetic harvester were also considered. The results from numerical studies for these three cases are summarized in Figures 6.11, 6.12, and 6.13, respectively. Since the parallel capacitor reduced the impedance of the electrical load, increasing the parallel capacitor resulted in the state of the system closing to the short circuit, and thus the natural frequency of the system approaching the natural frequency at the short circuit. As a result, the device was at resonance with the excitation. As shown in Figure 6.11 (a) and (b), the device velocity was kept in the same value, and the work efficiency of the excitation was $\eta = 100\%$, when the parallel capacitor increased over $100C_p$. Because of the decrease of the impedance caused by the parallel capacitor, the increase of the parallel capacitor lead to the decrease of the optimal resistive load of the device and the power delivered to the resistive load, as shown in Figure 6.11 (c). Since the device was at resonance with the excitation when the parallel capacitor was not less than $100C_p$, the input power of the excitation was kept in the same level which is independent of the resistive load R_L (Figure 6.11 (d)). Figure 6.12 shows the effects of the full-bridge rectifier on the load characteristics of the device. As indicated by Equation (6.10), the voltage drop of the rectifier not only caused the hardening of the system stiffness but also contributed a

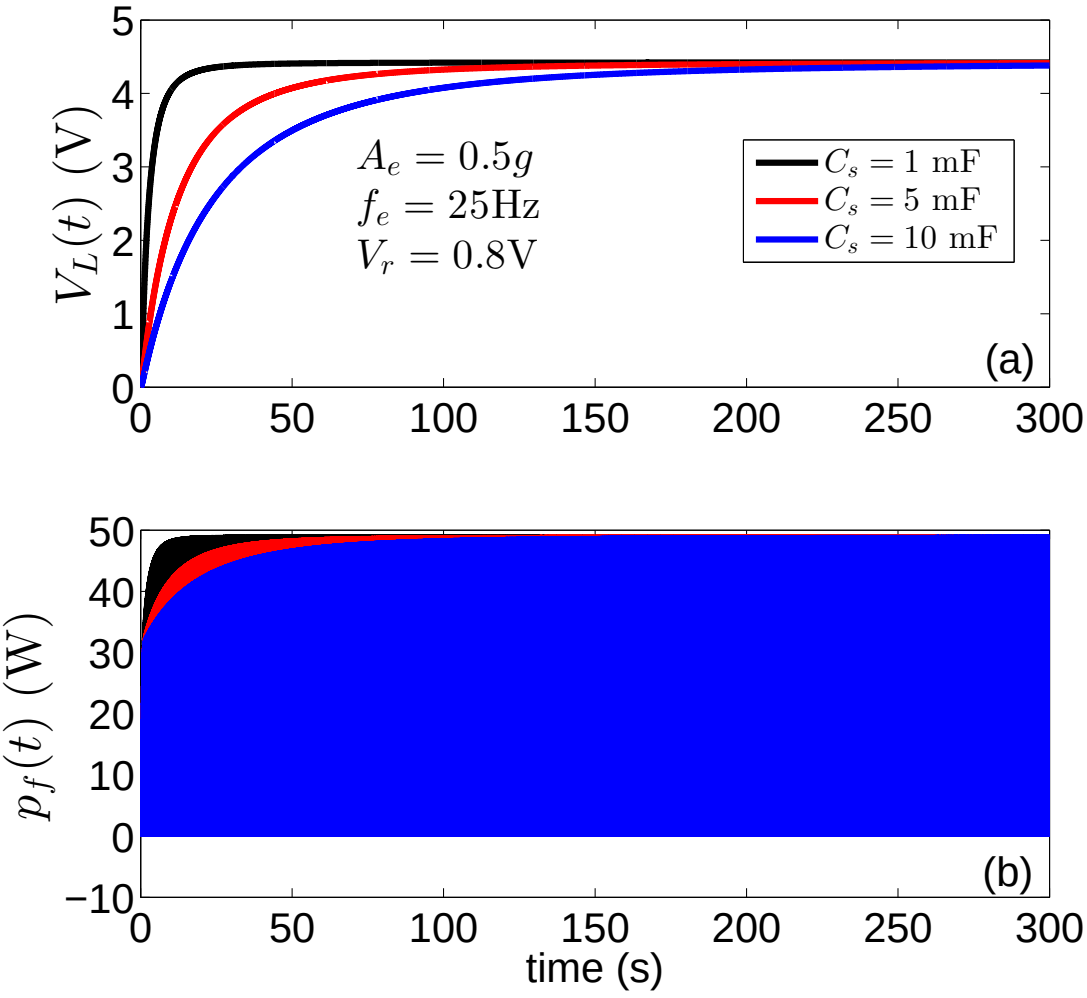

Figure 6.10: When the electricity generated by an electromagnetic harvester is stored in capacitors, time history of: (a) Voltage across the capacitor $V_L(t)$ and (b) instantaneous power of the excitation $p_f(t)$. The excitation was fixed at $0.5g$ and 25 Hz, and the voltage drop was 0.8V. Blue: $C_s = 10$ mF; Red: $C_s = 5$ mF; and Dark: $C_s = 1$ mF. Time for charging the capacitor to 99% ultimate voltage ($V_{L_{ult}} = 4.42$ V) was 29.4 s for $C_s = 1$ mF, 143.6 s for $C_s = 5$ mF, and 286.4 s for $C_s = 10$ mF, respectively. At such time instant, the energy stored in the capacitor $E_{C_s} = \frac{1}{2} C_s V_L$ was 0.0096 J for $C_s = 1$ mF, 0.0479 J for $C_s = 5$ mF, and 0.0957 J for $C_s = 10$ mF, respectively.

dry friction to the system. Thus, increasing the voltage drop lead to the decrease of the device response, as shown in Figure 6.12(a). Figure 6.12(b) shows that the work efficiency of the excitation decreased with the increase of the voltage drop. As shown in Figure 6.12(c), the voltage drop had no effect on the optimal resistive load of the piezoelectric harvester, i.e. $R_{L_{opt}} = 3500\Omega$, but the power delivered to the resistive load became smaller because the voltage drop reduced the device response, and thus the input power of the excitation (Figure 6.12(d)). Figure 6.13 describes the effects of a parallel capacitor with a rectifier on the load characteristics of the piezoelectric harvester. Compared to the cases shown in Figures 6.11 and 6.12, it can be seen that the combination of the parallel capacitor and the rectifier was beneficial for improving device performance. It is noticed that with the rectifier, the increase of the parallel capacitor resulted in the increase of the optimal resistive load of the piezoelectric harvester, i.e. $R_{L_{opt}}$ increasing from 3500Ω to 5000Ω when C_r increased from $0C_p$ to $1000C_p$, as shown in Figure 6.13(c).

The frequency response of the piezoelectric harvester was then evaluated. The same electrical loads in the load test were considered. The resistive load was fixed at 3500Ω. Figure 6.14 shows the effect of a resistive load with a parallel capacitor on the frequency response performance of the device. It can be seen that increasing the parallel capacitor decreased the natural frequency of the device because the involvement of the parallel capacitor lead to the decrease of the impedance of the electrical load, while the stiffness of the device was decreasing with the decrease of the electrical impedance. Thus, the natural frequency of the device gradually decreased to the natural frequency at the short circuit, i.e. $\omega_{n_{sc}} = 121$ Hz when the capacitor increased to $1000C_p$. Since the decrease of the impedance of the electrical load caused the decrease of the output voltage of the device, the reverse effect of the electromechanical coupling became weakening, resulting in the increase of device response, as shown in Figure 6.14(a). Figure 6.14(b) shows that the increase of the parallel capacitor narrowed the frequency range in which

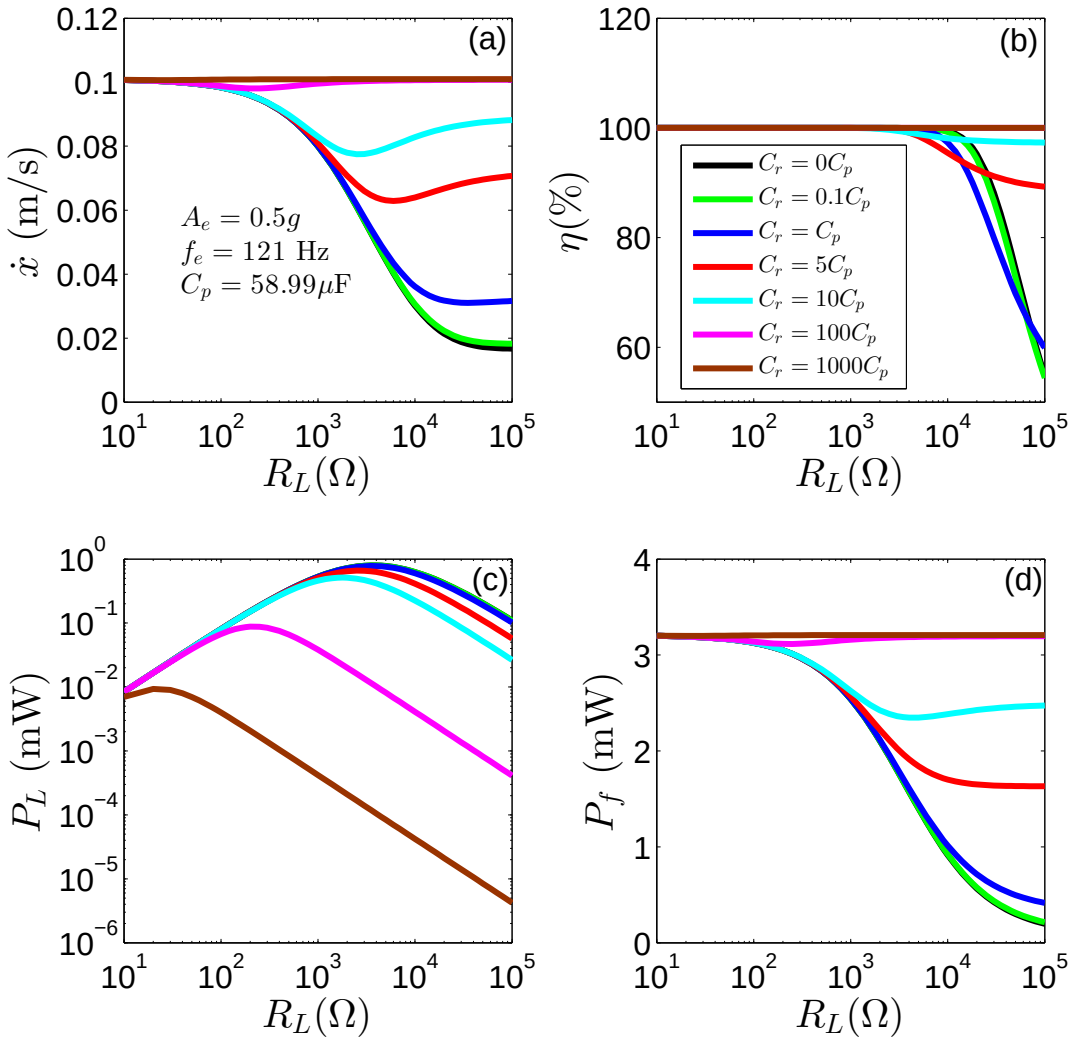

Figure 6.11: Effects of a parallel capacitor on load characteristics of a piezoelectric harvester under the excitation of $A_e = 0.5g$ and $f_e = 121$Hz: (a) Velocity $\dot{x}$, (b) Work efficiency of the excitation $\eta = \frac{\int_0^{\frac{2\pi}{\omega}} F(x,t)\dot{x}\mathrm{dt}}{\int_0^{\frac{2\pi}{\omega}} |F(x,t)\dot{x}|\mathrm{dt}}$ where ω is the excitation frequency, (c) Average power delivered to the resistance P_L, and (d) Average input power of the excitation P_f.

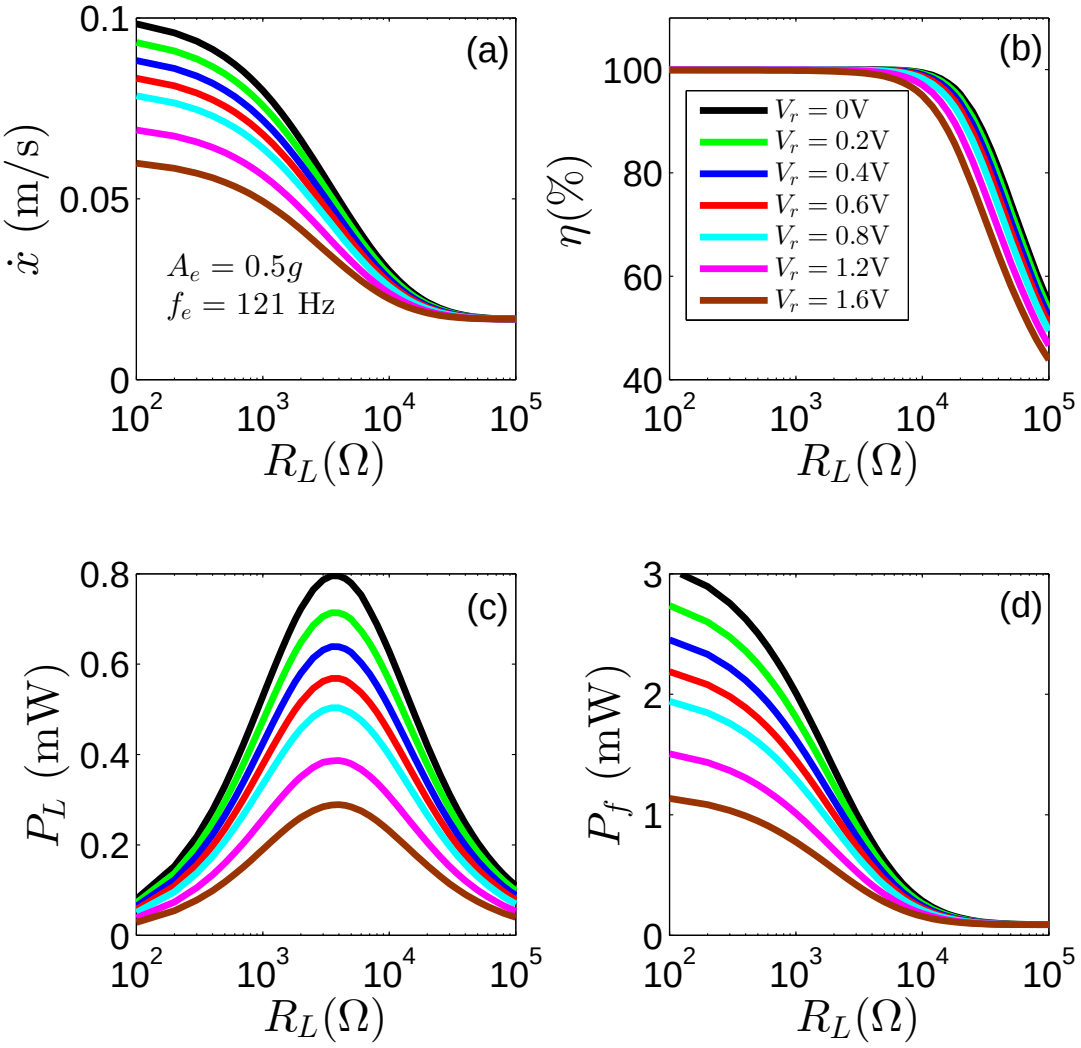

Figure 6.12: Effects of a full-bridge rectifier on load characteristics of a piezoelectric harvester under the excitation of $A_e = 0.5g$ and $f_e = 121$Hz: (a) Velocity $\dot{x}$, (b) Work efficiency of the excitation $\eta = \frac{\int_0^{\frac{2\pi}{\omega}} F(x,t)\dot{x}\mathrm{dt}}{\int_0^{\frac{2\pi}{\omega}} |F(x,t)\dot{x}|\mathrm{dt}}$ where ω is the excitation frequency, (c) Average power delivered to the resistance P_L, and (d) Average input power of the excitation P_f.

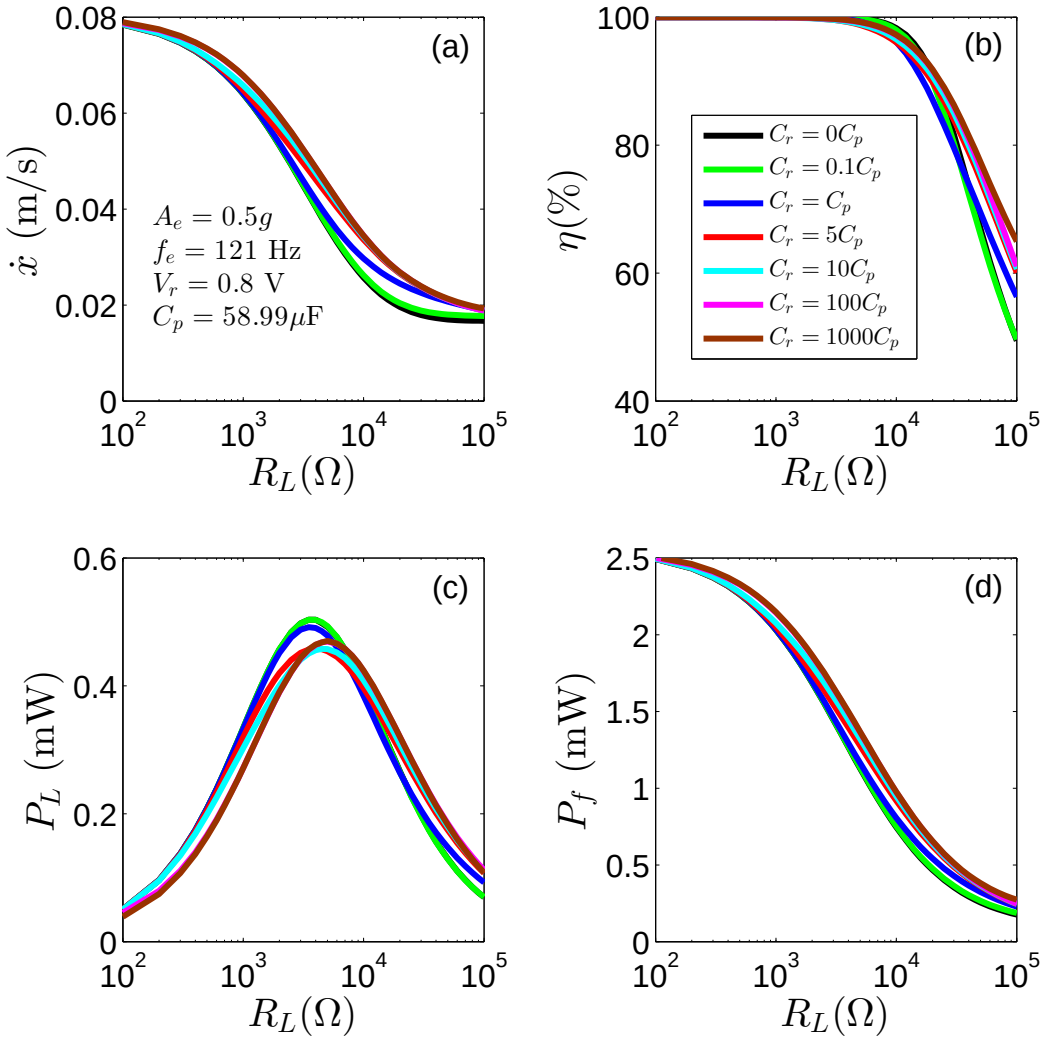

Figure 6.13: Effects of a parallel capacitor with a full-bridge rectifier on load characteristics of a piezoelectric harvester under the excitation of $A_e = 0.5g$ and $f_e = 121$Hz: (a) Velocity $\dot{x}$, (b) Work efficiency of the excitation $\eta = \frac{\int_0^{\frac{2\pi}{\omega}} F(x,t)\dot{x}\mathrm{dt}}{\int_0^{\frac{2\pi}{\omega}} |F(x,t)\dot{x}|\mathrm{dt}}$ where ω is the excitation frequency, (c) Average power delivered to the resistance P_L, and (d) Average input power of the excitation P_f.

the work efficiency of the excitation was as high level. Because of the decrease of the impedance of the electrical load, the power delivered to the electrical load became smaller as the increase of the parallel capacitor, as shown in Figure 6.14(c). In the contrary, the input power of the excitation was increased when the parallel capacitor increased (Figure 6.14(d)). The reason was that the increase of the parallel capacitor resulted in the enlarging of the device response.

Figure 6.15 summarizes the results from numerical studies about the effects of a resistive load with a rectifier on the frequency response performance of the piezoelectric harvester. It can be seen that the voltage drop of the rectifier not only hardened the stiffness of the device but also reduced the device response, as predicted by the theoretical analysis for case (I). Figure 6.15(a) shows the relationship between the system response and the voltage drop of the rectifier. Because of the presence of the rectifier, not only the stiffness of the system became more hardening, but an additional equivalent dry friction was also introduced to the system dynamics, compared to those of the system with the pure resistance. These two factors caused the decrease of the system response. With the increase of the voltage drop, the system response became smaller. Moreover, the presence of the voltage drop not only reduced the voltage across the resistance but also extended the duration of the system at the open circuit, leading to significant decrease of the power delivered to the resistance. For example, the maximum P_L decreased from 0.799mW to 0.337mW when the voltage drop V_r increased from 0V to 1.6V as shown in Figure 6.15(c). It is noticed that the extension of the system at the open circuit hardened the system stiffness, which resulted in the natural frequency shifted to the higher. For example, the natural frequency was increased from 122 Hz to 125 Hz when the voltage drop of the rectifier increased from 0V to 1.6V.

Figure 6.16 shows the effects of the resistive load with the regulating capacitor and the rectifier on the frequency-response performance of the device. The voltage drop of the rectifier was fixed at 0.8 V. As the parallel connection of the regulating capac-

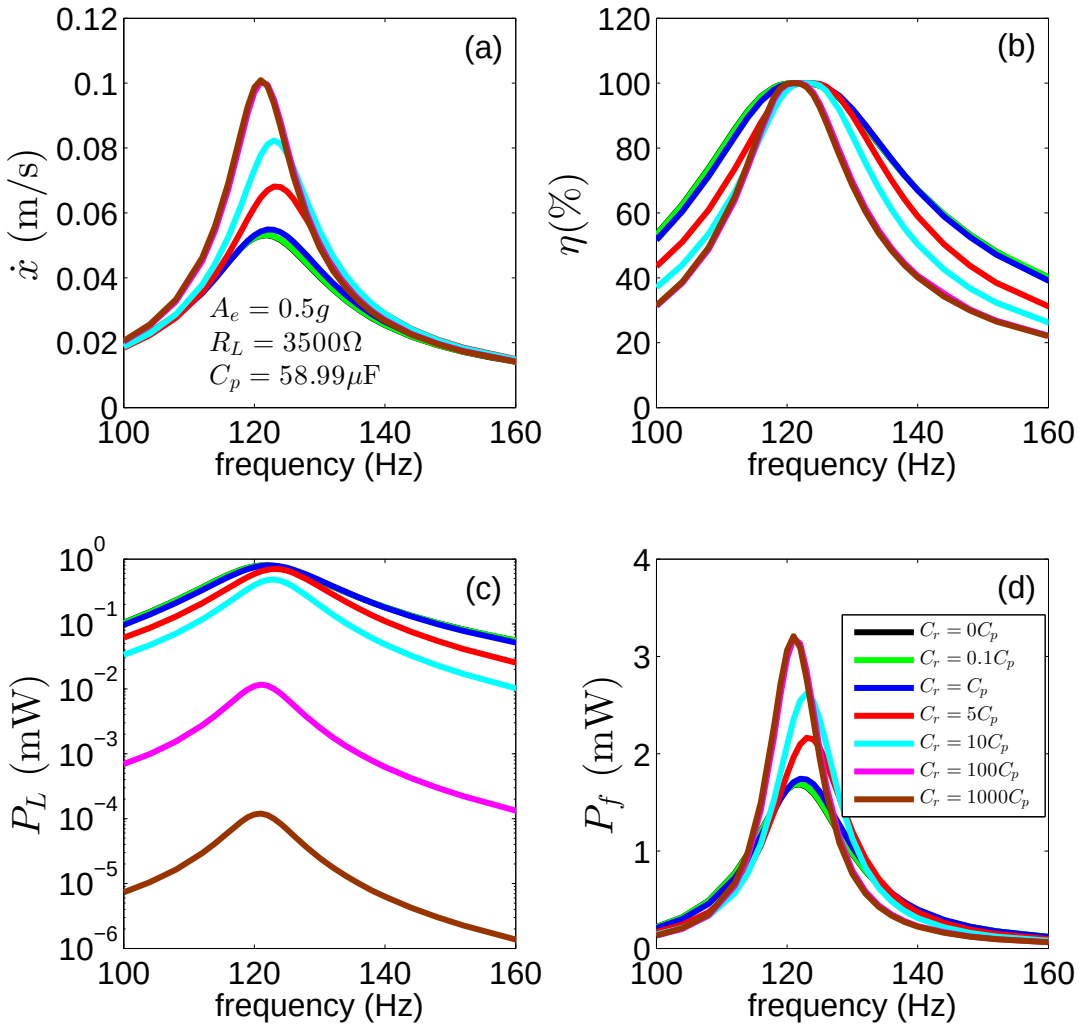

Figure 6.14: Effects of a parallel capacitor on single frequency-response performance of a piezoelectric harvester with a resistive load ($R_L = 3500\Omega$): (a) Velocity $\dot{x}$, (b) Work efficiency of the excitation $\eta = \frac{\int_0^{\frac{2\pi}{\omega}} F(x,t)\dot{x}\mathrm{dt}}{\int_0^{\frac{2\pi}{\omega}} |F(x,t)\dot{x}|\mathrm{dt}}$ where ω is the excitation frequency, (c) Average power delivered to the resistance P_L, and (d) Average input power of the excitation P_f.

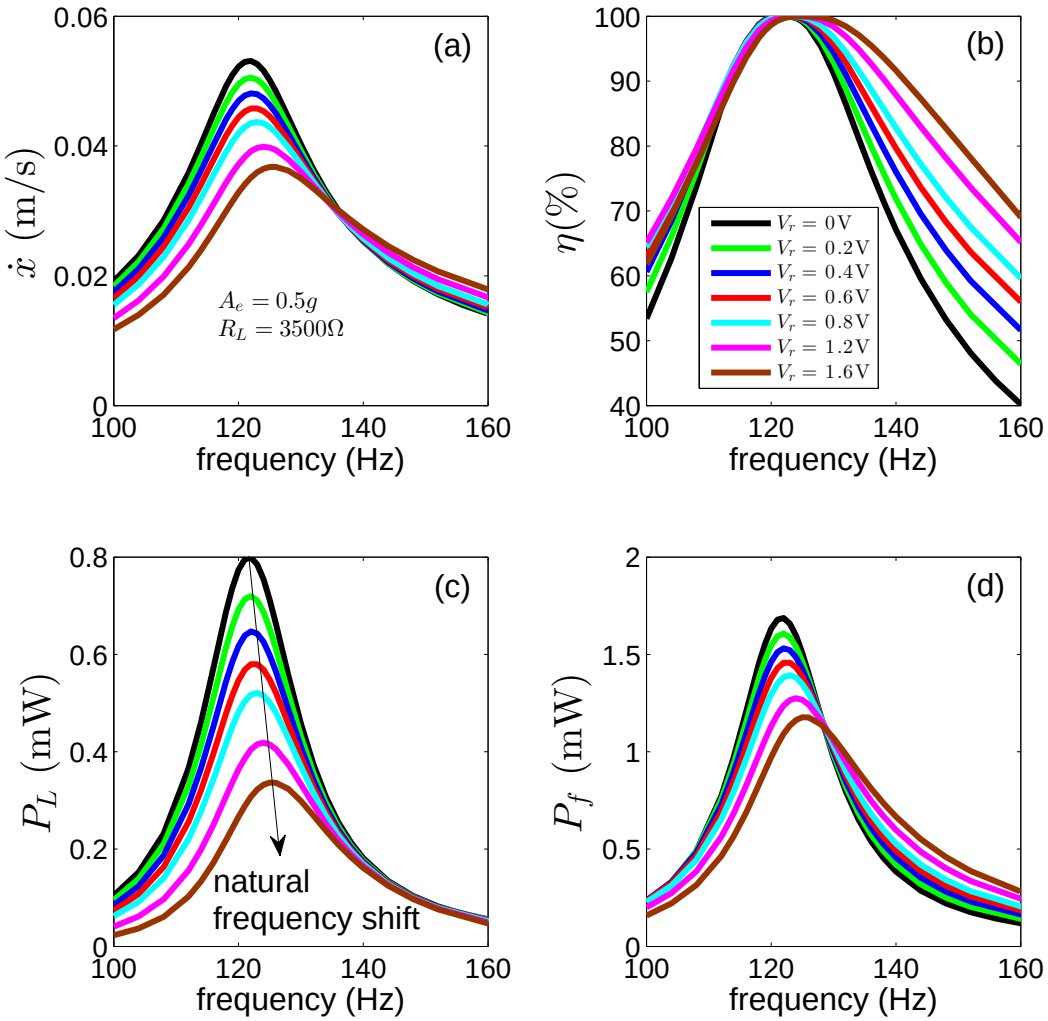

Figure 6.15: Effects of a full-bridge rectifier on single frequency-response performance of a piezoelectric harvester with a resistive load ($R_L = 3500\Omega$): (a) Velocity $\dot{x}$, (b) Work efficiency of the excitation $\eta = \frac{\int_0^{\frac{2\pi}{\omega}} F(x,t)\dot{x}\mathrm{dt}}{\int_0^{\frac{2\pi}{\omega}} |F(x,t)\dot{x}|\mathrm{dt}}$ where ω is the excitation frequency, (c) Average power delivered to the resistance P_L, and (d) Average input power of the excitation P_f.

itor reduced the impedance of the electrical load, the output voltage of the harvester became smaller, which reduced the reverse effect of the electromechanical coupling, being equivalent to the decrease of the damping, as compared to the case without the regulating capacitor. For a linear piezoelectric harvester, the decrease of the damping enlarged the system response. Different from the case of a resistive load with a parallel capacitor, the presence of the rectifier resisted the increase of device response. Combined the two factors, thus, the device response in this case was increased but could not be up to the same level as that in the case of a resistive load with a parallel capacitor, as shown in Figure 6.16(a). It is noted that when the regulating capacitor was employed, the output voltage and duration of the harvester at the closed circuit were both reduced, resulting in the decrease of the power delivered to the resistance. With the increase of the regulation capacitor, the power output was reduced and ultimately tended to a constant, as shown in Figure 6.16(c). Compared to the case of pure resistive load, the natural frequency of the device was shifted from 122Hz to 123Hz, while the maximum power deliver to the resistive load was reduced from 0.799 mW to less than 0.521 mW. In this situation, therefore, using the case of pure resistive load to predict the case of the resistive load with the regulating capacitor and the rectifier lead to not only 53.36% overestimation on the maximum output power of the device, but also 1% underestimation on the natural frequency of the device. For the piezoelectric harvester, the presence of the regulating capacitor caused the increase of the device response, resulting in the increase of the input power of the excitation (Figure 6.16(d)).

Figure 6.17 displays the results from the investigation of the effects of charging circuit on the performance of the piezoelectric harvester. The excitation frequency was fixed at 146 Hz which was closed to $\omega_{n_{oc}}$ of the device. Three storing capacitors were used, i.e. $C_s = 0.1$ mF, 0.5 mF, and 1 mF. With charging circuits, the device response finally settled at the open-circuit state when the voltage across capacitors tended to the ultimate voltage which was the difference between the amplitude of the open-circuit

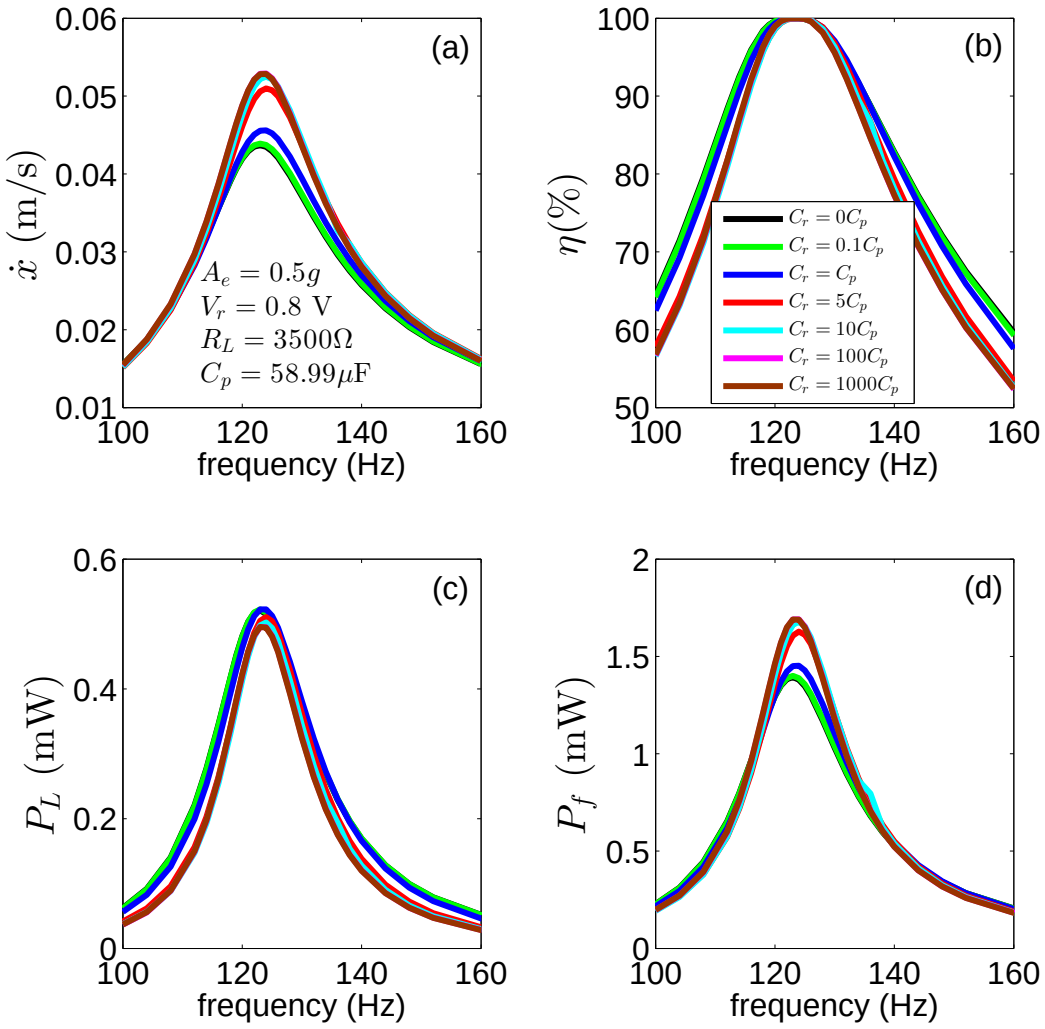

Figure 6.16: Effects of a parallel capacitor with a full-bridge rectifier on single frequency-response performance of a piezoelectric harvester with a resistive load ($R_L = 3500\Omega$): (a) Velocity $\dot{x}$, (b) Work efficiency of the excitation $\eta = \frac{\int_0^{\frac{2\pi}{\omega}} F(x,t)\dot{x}\mathrm{dt}}{\int_0^{\frac{2\pi}{\omega}} |F(x,t)\dot{x}|\mathrm{dt}}$ where ω is the excitation frequency, (c) Average power delivered to the resistance P_L, and (d) Average input power of the excitation P_f.

voltage of the harvester and the voltage drop of the rectifier ($V_{L_{ult}} = 22.86$ V). When the voltage across the capacitors was charged to be 99% of the ultimate voltage, the ratio of the charging time for these three capacitors (i.e. $t_{1mF} : t_{0.5mF} : t_{0.1mF}$) was $13.75 : 6.42 : 1$, which was greater than the ratio of the capacitance values, i.e. $10 : 5 : 1$. The related average power was calculated to be 0.2822 mW for $C_s = 0.1$ mF, 0.2197 mW for $C_s = 0.5$ mF, and 0.2054 mW for $C_s = 1$ mF, respectively. For the piezoelectric harvester, larger capacitor had longer charging time and lower average power.

6.3 Concluding Remarks

In this chapter, the effects of three types of non-resistive loads on the performance of vibration energy harvesters were investigated. The theoretical and numerical results have confirmed that the device performance obtained from resistive loads cannot be generalized for applications based on non-resistive loads. For both electromagnetic and piezoelectric harvesters, using the results obtained from resistive loads to evaluate device performance not only result in more than 50% overestimation in the maximum power delivered to the resistive load for the cases (I) and (II), but also underestimate the optimal resistive load in case (II). For an electromagnetic harvester, although the regulating capacitor and the device inductance establish an LC circuit, its effect on the frequency characteristics of the device cannot be observed because of the over-damping ratio of the LC circuit. The unrealistic example considered has shown that for an under-damped LC circuit, however, the device dynamics can be significant affected. In such system dynamics, the capacitor plays a role of damping. Different from the dissipated damping, however, the damping contributed by the capacitor facilitates energy transfer between mechanical and electrical subsystems without energy dissipation. Such evidence indicates the possibility of using damping to adjust device performance. For a piezoelectric harvester, the resonance frequency of the device with a resistive load

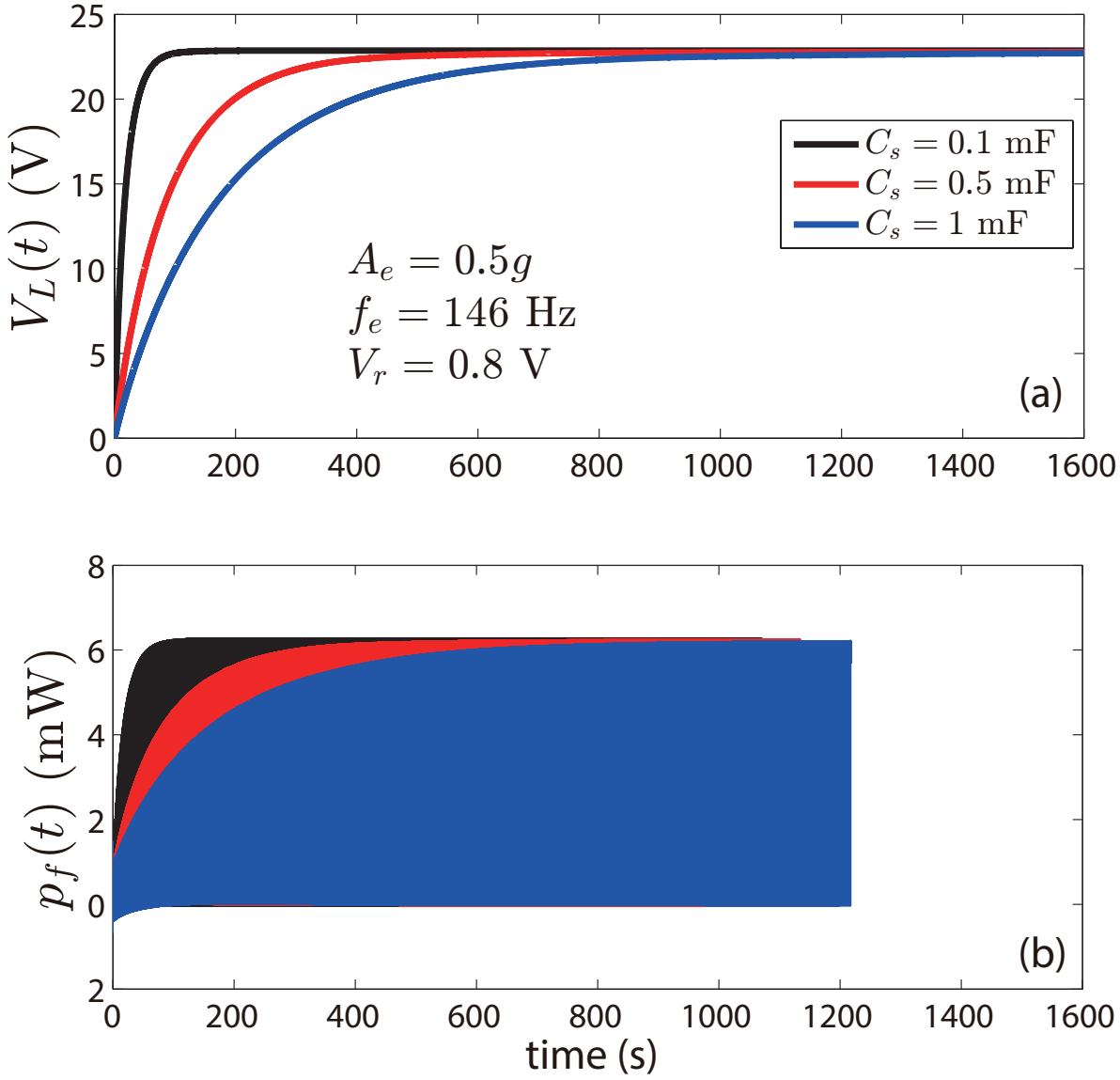

Figure 6.17: When the electricity generated by a piezoelectric harvester is stored in capacitors, time history of: (a) Voltage across the capacitor $V_L(t)$ and (b) instantaneous power of the excitation $p_f(t)$. The excitation was fixed at $0.5g$ and 146 Hz, and the voltage drop was 0.8V. Blue: $C_s = 1$ mF; Red: $C_s = 0.5$ mF; and Dark: $C_s = 0.1$ mF. Time for charging the capacitor to 99% ultimate voltage ($V_{L_{ult}} = 22.86$ V) was 90.7 s for $C_s = 0.1$ mF, 582.7 s for $C_s = 0.5$ mF, and 1246.9 s for $C_s = 1$ mF, respectively. At such time instant, the energy stored in the capacitor $E_{C_s} = \frac{1}{2} C_s V_L$ was 0.0256 J for $C_s = 0.1$ mF, 0.1280 J for $C_s = 0.5$ mF, and 0.2561 J for $C_s = 1$ mF, respectively.

is smaller than that of the device with a non-resistive load. For the charging circuit, the results have suggested that larger storing capacitor is beneficial for an electromagnetic harvester but not for a piezoelectric device.

Chapter 7

MANIPULATING ROLES OF THE EXCITATION TO ENHANCE ENERGY HARVESTING PERFORMANCE

Harvesting energy from vibrations has been reckoned as a promising, enabling technology because of its potential in revolutionizing a variety of applications, such as sensing [4, 91], monitoring[77], in vivo powering of medical devices [92, 93], etc. The past two decades have witnessed considerable advances in vibratory energy harvesting, but its well-regarded promise still remains far from reality. A careful review of the literature appears to lead to the conclusion that some fundamental aspects of energy transfer in an energy harvesting system have been overlooked and the lack of such understandings may have been the culprit of the current technological stagnation in this field.

The objective of vibratory energy harvesting is to extract as much energy as possible from a vibrating body – the source. In doing so, a harvester must dynamically interact with the source, rendering a problem of targeted energy transfer between two systems [30, 94]. If the harvested energy is negligible compared to that of the source, it is admissible to assume that the harvesting activity does not alter the vibrations of the source, i.e. the source can be treated as an infinite energy source. If one considers the problem in the entire parameter space, it is equivalent to the problem of global optimization, in which the harvested energy is the target for maximization. For devices

whose responses to external excitations can be described in closed-form expressions, e.g. linear devices, the optimization problem can be solved exactly because the closed-form solutions span the entire parameter space [13]. For nonlinear devices, the optimization problem cannot be exactly solved because of the lack of closed-form representations of the responses. As a compromise, nonlinear devices/designs have been traditionally evaluated using the harvested energy as the performance indicator within a subset of the parameter space [9]. For example, the frequency responses obtained from the approximated, analytical solutions have been widely used for this purpose. If even the approximated solutions are not available, devices have been evaluated using numerical simulations and physical experiments that cover even smaller subspace of the parameter space. Caution must be exercised for such optimization based on a subset of the parameter space because the results may not be generalized. Not only may the conditions of the evaluations in the subset space favor one device over another, rendering an unfair comparison [62], the comparison itself also does not provide useful implication in the device performance outside the subset of the parameter space. For example, under a single-frequency excitation and provided that the stringent requirements on initial conditions are met, nonlinear devices perform well over a wider range of frequencies than linear devices [50, 78, 79, 81]. Because of the inapplicability of the principle of superposition, however, such a "broadband"performance does not indicate a satisfactory performance if the excitation is of rich frequency content. On the contrary, nonlinear devices may not offer any benefit under a multi-frequency excitation [59, 61, 62]. Thus, when the response cannot be described in closed form, such as the case of a nonlinear device, one has to return to the original problem of energy transfer.

There has been substantial work related to energy transfer between two systems. An account of targeted energy transfer most relevant to the current study can be found in Vakakis et el [95]. The effects of coupling strength on the performance of vibratory energy harvesting have been treated in [96, 97]. Although the excitation (or the host

vibration) is the source of the energy to be harvested, the excitation can temporally behave as a sink for a limited time, during which energy flows from the harvester back to the excitation. To the best knowledge of the authors, the role of the excitation acting as a sink in energy harvesting has not been examined. In this chapter, we show that the overlooked role of the excitation as a sink is important for the effectiveness and efficiency of a device. When the closed-form representation of the device response cannot be found, manipulating the roles of the excitation to minimize the extent to which it acts as a sink appears to be a viable alternative to the theoretical optimal solution.

7.1 Theoretical analysis

Following the most common practice in this field, let's consider an energy harvester and assume that the energy is harvested through a resistive load. The governing equation for the system can be generally written as

$$m\ddot{x} + c_m\dot{x} + k(x) + \kappa y = F(x,t), \tag{7.1a}$$

$$\alpha\dot{y} + \beta y = \kappa\dot{x}, \tag{7.1b}$$

where x denotes the displacement of the mass m, c_m the linear mechanical damping coefficient, $k(x)$ the restoring force, κ the linear electromechanical coupling coefficient, and $F(x,t)$ denotes the general external force, including parametrical excitations. For inductive devices, y, α and β represent the induced current, the inductance of the winding and the total resistance, respectively. For capacitive ones, they represent the induced voltage, the capacitance of the piezoelectric element and the load conductance, respectively. Over a reasonable period of time T, e.g. the fundamental period of a periodic oscillation, the harvested energy is $E_h = \beta\int_0^T y^2 dt$. The total dissipated

energy $E_d = c_m \int_0^T \dot{x}^2 dt + \beta \int_0^T y^2 dt$ is compensated by the net work of the excitation over T, i.e. $E_f = \int_0^T F(x,t)\dot{x}dt$.

The process of energy transfer between the excitation and the harvester can be analyzed using a generalized phase. As shown in Fig. 7.1, taking the force direction as the polar axis $\overrightarrow{\mathbf{OL}}$, the force $F(x,t)$ can be represented by the force vector: $\overrightarrow{\mathbf{F}} = (|F(x,t)|, 0)$. The velocity $\dot{x}$ can be denoted as the projection of the vector $\overrightarrow{\dot{\mathbf{x}}} = (A_v, \phi(t))$ on the polar axis $\overrightarrow{\mathbf{OL}}$, where A_v is the magnitude of the velocity and $\phi(t)$ is defined as the generalized, instantaneous phase between $\overrightarrow{\mathbf{F}}$ and $\overrightarrow{\dot{\mathbf{x}}}$. For periodic cases, A_v can be defined as the amplitude of the response, therefore $\cos\phi(t) = \frac{\dot{x}}{A_v}\,\mathrm{sgn}\,(F(t))$. Note that for the case where multiple harmonics exist in the response, which could be due to nonlinear system response and/or a broadband excitation, the generalized phase $\phi(t)$ is a nonlinear function of time. However, if there is a dominating frequency ω_d in the response, a linear approximation may be possible, i.e. $\phi(t) \approx \omega_d t + \phi_0$, ϕ_0 being a constant phase lag. The instantaneous power of the excitation is $p_f(t) = \overrightarrow{\mathbf{F}} \cdot \overrightarrow{\dot{\mathbf{x}}} = |F(x,t)|A_v \cos\phi(t)$. The role of the excitation in the energy transfer process is reflected by the instantaneous phase, $\cos\phi(t) > 0$ indicating that excitation works as an energy source to the device and $\cos\phi(t) < 0$ indicating that excitation draws energy from the device, acting as a sink. The net work of the excitation can be rewritten as $E_f = \int_0^T |F(x,t)|A_v \cos\phi(t)dt = |W^+| - |W^-|$ where W^+ and W^- denote the positive and negative work over T, respectively. The sum of the absolute values of the positive and negative work represents the actual "effort"of the excitation. It has been shown that under the global resonance condition [83], $|W^-| = 0$, the total effort of the excitation is completely converted into the useful work. Under a non-resonant condition, $|W^-| \neq 0$, thus $|W^+| - |W^-| < |W^+| + |W^-|$, only part of the total effort of the excitation contributes to the useful work. Therefore, the performance of the harvester can be

evaluated using the coupling efficiency defined as

$$\eta = \frac{|W^+| - |W^-|}{|W^+| + |W^-|} = \frac{\int_0^T |F(t)| \cos\phi(t) dt}{\int_0^T |F(t)||\cos\phi(t)| dt}. \tag{7.2}$$

For a given excitation, adjustment of the phase can lead to changes in the work of the excitation and the coupling efficiency η, i.e. $\Delta E_f = \Delta W^+ - \Delta W^-$ and $\Delta\eta = \frac{2\left(\Delta W^+|W^-| - \Delta W^-|W^+|\right)}{(|W^+| + \Delta W^+ + |W^-| + \Delta W^-)(|W^+| + |W^-|)}$. There are five general possibilities:

- Case I: $\Delta W^+ \geq 0$ and $\Delta W^- < 0$, then $\Delta\eta > 0$ and $\Delta E_f > 0$;
- Case II: $\Delta W^+, \Delta W^- < 0$ and $\frac{\Delta W^+}{\Delta W^-} < 1$, then $\Delta\eta > 0$ and $\Delta E_f > 0$;
- Case III: $\Delta W^+, \Delta W^- < 0$ and $1 \leq \frac{\Delta W^+}{\Delta W^-} < \frac{W^+}{W^-}$, then $\Delta\eta > 0$ and $\Delta E_f \leq 0$;
- Case IV: $\Delta W^+, \Delta W^- < 0$ and $\frac{W^+}{W^-} \leq \frac{\Delta W^+}{\Delta W^-}$, then $\Delta\eta \leq 0$ and $\Delta E_f < 0$;
- Case V: $\Delta W^+ < 0$ and $\Delta W^- > 0$, then $\Delta\eta < 0$ and $\Delta E_f < 0$.

Note that when the coupling efficiency increases, $\Delta\eta > 0$, the total harvested energy increases because of the reduction of the negative work (Case I, II), except when the reduction of the positive work is more significant (Case III). When the coupling efficiency reduces, $\Delta\eta < 0$, the total energy harvested reduces (Case IV, V). Thus, if it is possible to adjust the phase such that the positive work of the excitation is increased and the negative work is reduced, the harvested energy will increase.

7.2 Experimental materials and model

In this section, vibro-impact was utilized to introduce sudden phase changes. An inductive device was constructed with a unilateral constraint to provide a nonlinearity that allows for a sudden change of the role of the excitation. The device (Fig. 7.2) consisted of a diamagnetically levitated sheet of pyrolytic graphite (31.5 mm $\times$31.5 mm

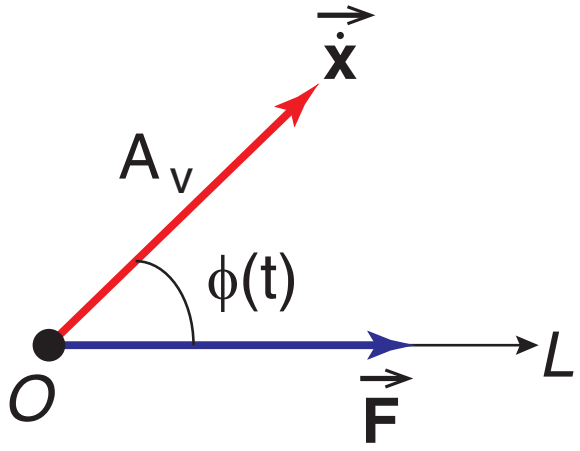

Figure 7.1: Vector representation of the excitation $F(x,t)$ and the velocity of the response $\dot{x}(t)$.

$\times$1 mm)[98–100]. Eight identical windings were symmetrically attached to both sides of the graphite. The windings were fabricated using #44 AWG copper wire (each with 160 turns) and were connected in series giving a total resistance of $R_w = 315.7\ \Omega$. A resistive load, R_L was used as the electrical load to evaluate the device behavior. In this example, the inductive devices under low-frequency excitations were considered. Thus, the electromechanical coupling, represented in Eq. (7.1b), could be approximated as an algebraic relationship (because $\alpha << \beta$), i.e. $\beta y = \kappa\dot{x}$. The effect of the electromechanical coupling on the device dynamics could be represented as an effective electrical damping, i.e. $c_e = \kappa^2/\beta$. Therefore, the effect of R_w and R_L on the system can be equivalent to the electrical damping c_e. The mass of the pyrolytic graphite with the attached windings was 3.11×10^{-3} kg. Levitation was achieved over a sixteen-block array of cubic (12.7 mm) NdFeB magnets. The maximum magnetic flux density was measured to be 0.645 T on the surface of the magnet. At static equilibrium, the air gap between the levitated component and magnet was $z_{gap} = 0.25$ mm. Because the air gap was much smaller than the length scale of the pyrolytic graphite sheet (PGS), the squeeze-film effect was considerable [101]. In order to reduce such effect, a through hole of 3.23 mm in diameter was drilled in the center of every magnet, parallel to the

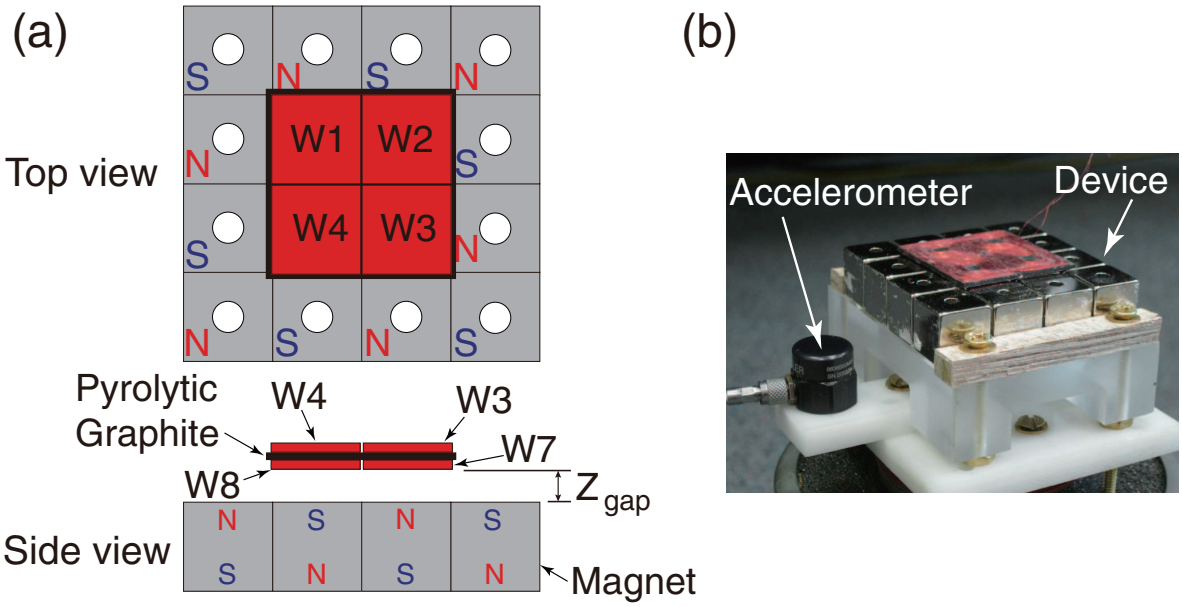

Figure 7.2: Prototype Device. (a) Schematic diagrams, and (b) the experiment apparatus (the shaker, the electrical load, and the oscilloscope are not shown).

magnetization direction. The linear fundamental frequency and mechanical damping ratio of the device were identified from the free-vibration tests to be $\omega_0 = 16.1$ Hz and $\xi_m = 9.66\%$, respectively. The device was tested on a shaker (Model LW-126-13, Labworks Inc.). Measurements were obtained using an oscilloscope (Model DPO 3040).

Because of the unilateral constraint, the dynamics of the device under a vertical, base excitation can be represented by the following equations [102]

$$\begin{aligned} \ddot{z} + 2\omega_0\xi\dot{z} + g - \frac{F_d(z)}{m} = f(t), \quad z > -z_{gap} \\ \dot{z} \to -e_k\dot{z}, \quad z = -z_{gap}, \end{aligned} \tag{7.3}$$

where z is the displacement of the PGS center with respect to its rest position, and e_k is the coefficient of restitution, identified to be $e_k = 0.6$ in this study. The flipping of the velocity can be represented using the phase $\phi(t)$, i.e. $\cos\phi(t) \to -e_k \cos\phi(t)$. The total damping includes the mechanical damping (ξ_m) and the equivalent electrical damping (ξ_e), i.e. $\xi = \xi_m + \xi_e$. Symbol g denotes the gravitational acceleration. The

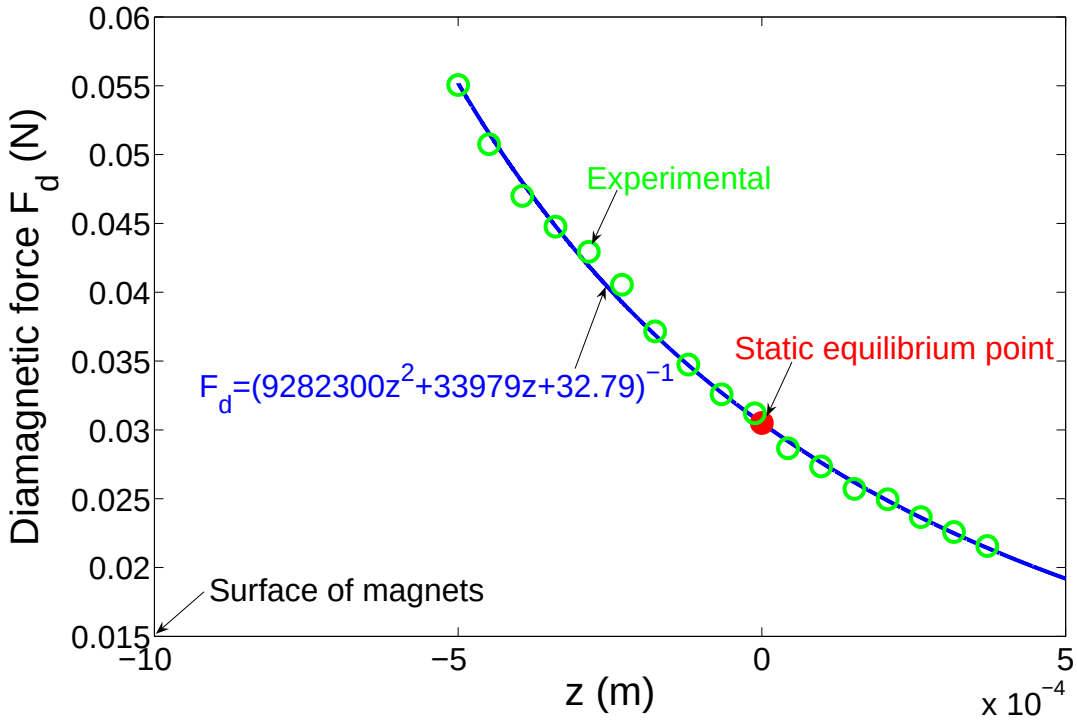

Figure 7.3: Relationship between diamagnetic force and the displacement. Line: fitting function, circle: experimental results, solid circle: rest position of the center of pyrolytic graphite.

diamagnetic force $F_d(z)$ was determined experimentally to be $F_d(z) = (9.2823 \times 10^6 z^2 + 3.3979 \times 10^4 z + 32.79)^{-1}$ as shown in Fig. 7.3.

7.3 Results and Discussion

Fig. 7.4 summarizes the results from the numerical and experimental studies conducted for single-frequency excitations, i.e. $f(t) = A_e \cos \omega t$. The numerical simulations were conducted using the Dormand-Prince method (MATLAB© ode45). Four excitation levels, $A_e = 0.2\ g$, $0.4\ g$, $0.6\ g$, $1.0\ g$, were considered. Because of the limitations of the experiment apparatus, only the excitation level of $A_e = 0.2\ g$ was used for the experiments. For all the experimental cases, the resistive load was fixed at $R_L = 1\ \text{k}\Omega$,

corresponding to an electrical damping ratio of $\xi_e = 18\%$. The results for the artificial case without the amplitude constraint and thus without impacts were obtained using the theoretical model, Eq. (7.3). They are also shown for comparison. The excellent agreement between the numerical and experimental results shown in Fig. 7.4(a) demonstrates the validity of the theoretical model. The instantaneous changes of the phase due to the impacts were favorable outside the resonant zone of the device, as shown in Fig. 7.4(a) and (b). The correlation between the coupling efficiency and the harvested energy appeared to be consistent, i.e. reducing the coupling efficiency led to the reduction of the harvested energy and increasing the harvested energy led to the increased efficiency, as predicted respectively by cases IV and V and cases I and II discussed previously. In some small regions, 10.4∼11.2 Hz, 19∼19.9 Hz, case III dominated. Fig. 7.4(c) illustrates the changes of the absolute values of the positive and negative work of the excitation due to the phase changes. When the frequency of the excitation was much lower than that of the device, the positive and negative work simultaneously decreased, corresponding to cases II, III, and IV. For excitations with frequencies close to the fundamental frequency of the device, the positive work reduced but the negative work increased, corresponding to case V. At higher excitation frequencies, case I dominated, i.e. the negative work was reduced and the positive work was increased. Fig. 7.5 shows the time histories of the instantaneous work of the excitation for the five different cases (i.e. I∼V) under a single-frequency excitation of different frequencies with a fixed amplitude $A_e = 1\ g$. It is noted that for the type of device architecture considered, mechanical impacts occur only at times when the seismic mass is moving away from the rest position. When the period of the excitation is shorter than the natural period of the device, there is generally a phase lag $0 < \Delta\varphi < \frac{\pi}{2}$ of the velocity of the response. The excitation does positive work as the seismic mass immediately moves away from the rest position. The positive work then gradually changes to negative because of the frequency mismatch. The exact size of the region within which the

work is positive depends on the phase lag. A minimal distance between the constraint and the rest position is required to guarantee that impacts would occur in the region of negative work, corresponding to case I. As the period of excitation approaches the natural period of the device, the region of the positive work is enlarged, requiring a larger distance prior to the impact, otherwise case III, IV or V could dominate depending on the parameters. At resonance, the phase lag is zero. The instantaneous work of the excitation is non-negative. Impacts downgrade the performance by turning the positive work to negative, corresponding to case V. When the period of the excitation is longer than the natural period of the device, the phase lag of the response velocity is $-\frac{\pi}{2} < \Delta\varphi < 0$. The excitation does positive work during the whole course of the seismic mass moving away from the rest position. Thus, impacts occur in the region of the positive work. Cases II$\sim$V could dominate depending on the parameters.

Fig. 7.6 shows the results from numerical studies for band-limited excitations with a bandwidth of 10 Hz and a flat power spectral density of $0.005\pi\ g^2{\cdot}\text{Hz}^{-1}$. The results resembled those of the single-frequency excitations. If the energy of the excitation was concentrated on higher frequencies, it appeared to be guaranteed that the instantaneous phase change would improve the performance (case I). Band-limited excitations with different bandwidths ($5 \sim 15$ Hz) were also considered. The results demonstrated qualitatively the same trend. They are not shown for brevity.

7.4 Concluding Remarks

Although the excitation is ultimately the source of the harvested energy, the extent of the excitation acting as a sink is critical to energy harvesting efficiency because it represents the wasted "effort"of the excitation not converted to harvested energy. The contradictory roles of the excitation were shown to be dictated by the mismatch between the properties of the excitation and the device. The degree of such mismatch

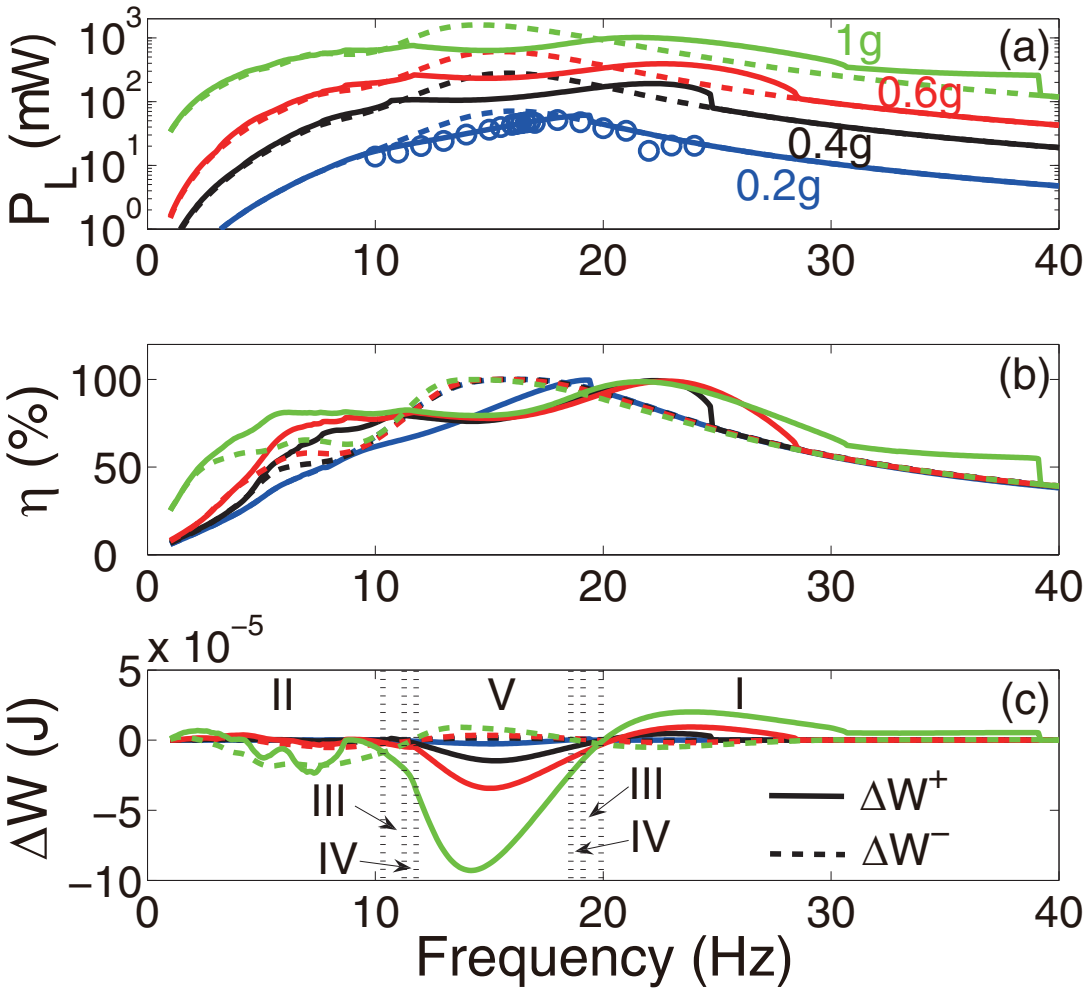

Figure 7.4: Results obtained under single-frequency excitations ($R_L = 1$ kΩ). (a) The average power P_L delivered to the resistive load, (b) the coupling efficiency η, (c) changes in the positive and negative work of the excitations ΔW. Lines: numerical results, circles: experimental results. In (a) and (b), solid lines: the prototype device, dashed lines: the artificial system without the amplitude constraint.

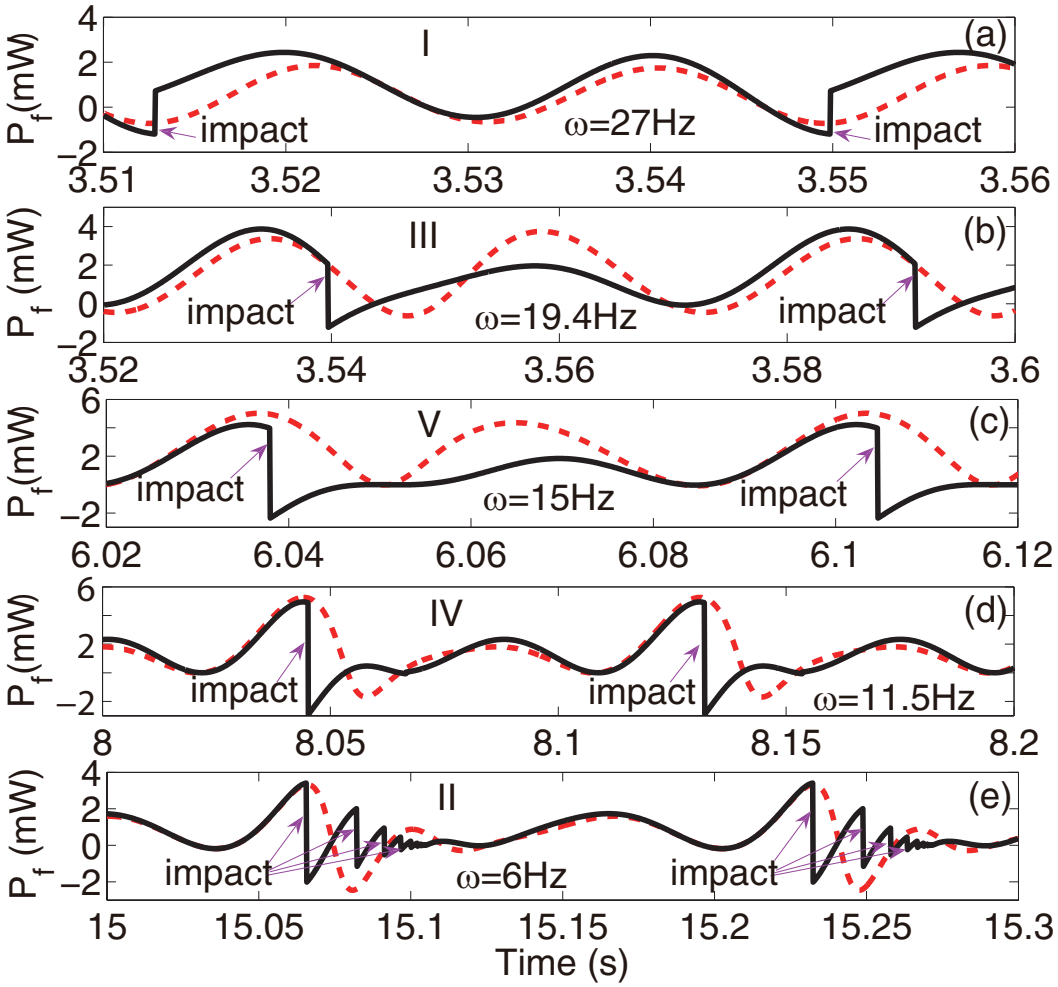

Figure 7.5: The instantaneous work of single-frequency excitations ($A_e = 1$ g, $R_L = 1$ kΩ) for the five difference cases (i.e. I∼V). Solid lines: the prototype device. Dashed lines: the artificial system without the amplitude constraint.

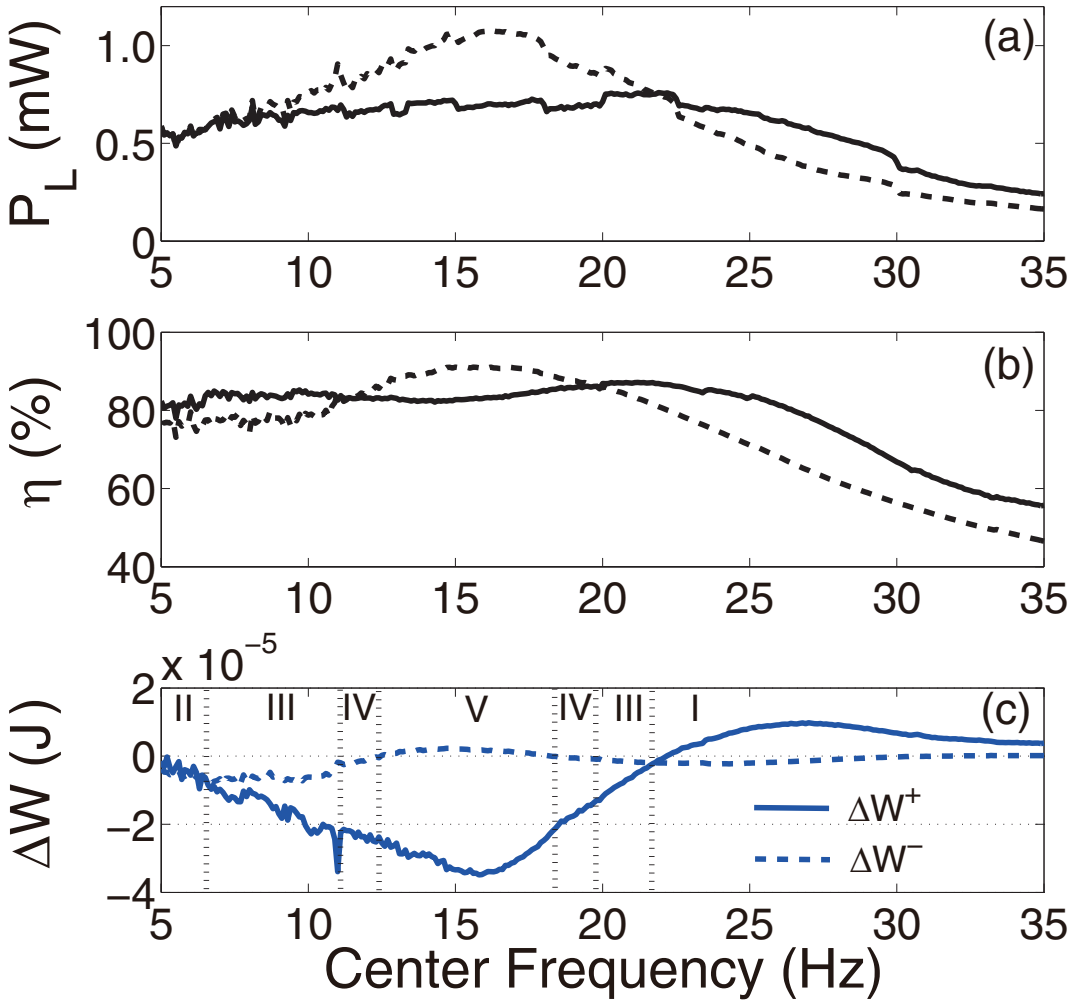

Figure 7.6: Numerical results obtained using band-limited excitations ($R_L = 1$ kΩ, bandwidth = 10 Hz, and PSD = 0.005π g^2·Hz^{-1}). (a) The average power P_L delivered to the resistive load, (b) the coupling efficiency η, and (c) the changes in the positive and negative work of the excitations ΔW. In (a) and (b), solid lines: the prototype device, dashed lines: the artificial system without the amplitude constraint.

can be represented by the generalized phase angle between the device response and the excitation. As demonstrated, an instantaneous phase angle shift can be achieved via vibro-impacts and it changes the role of the excitation. If the phase angle shift occurs at appropriate time instants such that it switches the excitation from being a sink to being a source, the mismatch is temporarily eliminated and the harvested energy can be dramatically increased. For example, the power increased from 153.1μW to 258.2μW at $A_e = 0.6g$ and $\omega = 26$ Hz. For random excitations with a 10 Hz bandwidth, the vibro-impact was shown to dramatically increase the device bandwidth and the device efficiency was kept around 80% for center frequencies up to 20 Hz. It is noted that vibro-impact occurs only when the seismic mass touches the magnets. Phase flipping caused by vibro-impact is thus not necessarily a continuous action and requires no energy compared to active methods that tune the natural frequencies. Because real-world ambient vibrations are normally random with broad bandwidths, a panacean solution of eliminating the mismatch based on passive methods is unlikely to exist. Thanks to continuously improving ultra-low power sensing and switching technologies, methods in which the role of the excitation is monitored and adjusted would be more promising in bringing vibratory energy harvesting to fruition.

Chapter 8

CONCLUSIONS

The aim of this study was to explore an effective technology of harvesting energy from low-level ambient vibrations. This study has investigated the effects of mechanical coupling on vibration energy harvesters, identifying some fundamental features regarding nonlinear resonance, damping, parametric excitation, bandwidth, dynamics with potential energy outside the potential well, and the roles of excitation. It has been shown that the role of excitation as a sink plays a significant role in vibration energy harvesting. The methods based on manipulating the roles of excitation to minimize the extent to which it acts as a sink has exhibited a huge potential to enhance energy harvesting performance. This study has also identified the effects of electrical loads on the performance of electromagnetic and piezoelectric harvesters. Three different types of non-resistive loads (i.e., a resistance with a rectifier, a resistance with a rectifier and a regulating capacitor, and a charging circuit consisting of a rectifier and a capacitor) have been used, and their impact on the harvester performance have been evaluated and compared.

In the aspect of mechanical coupling, this study has shown that when the energy of excitations is distributed over a broad spectrum of frequencies, existing methods cannot provide an effective solution; however, the method based on manipulating the roles of excitation shows a great potential to improve device performance. For existing methods, when the potential energy of linear or nonlinear harvesters is constrained

by their potential wells, the maximum performance can be achieved only at global resonance. When the potential energy escapes from the potential well, however, resonance is no longer a requirement for obtaining high device performance. Results have shown that although the response of nonlinear harvesters at subharmonic vibrations (i.e. the so-called nonlinear resonance) could be larger than that at global resonance, the amount of energy harvested at subharmonic vibrations can be orders of magnitude lower. It has also been found that tunable damping in a nonlinear harvester is advantageous to facilitating the resonance condition, while the parameterization of excitation is beneficial for extending the resonance condition to multiple zones of the excitation frequency. Even though the working frequency zone of nonlinear harvesters could be widened, it does not mean that nonlinear harvesters have broad bandwidth, because the principle of superposition does not apply. Theoretical and/or numerical results have demonstrated that for vibration energy harvesters, both linear and nonlinear, using bandwidth as a criterion of performance evaluation is not applicable. For the method based on manipulating the roles of excitation, theoretical and numerical results in chapter 7 have verified that the proposed harvester can overcome the limitation of bandwidth, exhibiting outstanding performance even under multi-frequency excitations.

With respect to electrical loads, the main findings are that using results obtained from resistive load to evaluate device performance based on non-resistive loads leads to significant overestimation at the power output and underestimation at the optimal resistance for the system. For an electromagnetic vibration energy harvester, if the LC circuit is an under-damped system and the energy stored in the capacitor can be transferred back to the mechanical system, the device dynamics can be significantly changed; while the capacitor not only helps establish the LC circuit, it also plays a role of damping to facilitate energy transfer between mechanical and electrical subsystems without energy dissipation. For a piezoelectric vibration energy harvester, both the

rectifier and capacitor affect harvester damping and stiffness. With a charging circuit, both electromagnetic and piezoelectric harvesters exhibit similar dynamic behavior, i.e. their responses are transient and non-stationary but gradually settle at an open-circuit state as more energy is stored in the capacitor. Thus, the final energy stored in the capacitor depends on the capacitance and the amplitude of open-circuit voltage of the harvesters. Since the natural frequency of a piezoelectric device at open circuit is different to that at closed circuit, it is thus suggested that for a piezoelectric device, designing the natural frequency at open circuit is at resonance with the excitation. In addition, the numerical results has also suggested that a larger storing capacitor is beneficial for an electromagnetic device, while the reverse applies for a piezoelectric device.

Contributions from this study were mainly within the fields of vibration energy harvesting and system dynamics. In vibration energy harvesting, the dominant trend reported in the literature is designing passive harvesters with broad bandwidth to fit real-world ambient vibrations, which are normally random with broad bandwidth. However, it is noted from this study that such a panacean solution is unlikely to exist. Results from the investigation of mechanical coupling and electrical loads have verified that seeking ways to increase harvester bandwidth and response can be ineffective to enhancing energy harvesting performance. The study suggests that in bringing vibratory energy harvesting to fruition, active methods in which the role of the excitation is monitored and adjusted in real time is more promising. The study has also shown that the introduction of rectifier and capacitor has effects on the damping and natural frequency of harvesters, differing from the effects of pure resistance, which is usually simplified as damping. Such results suggest that harvester performance should be evaluated while driving the actual electrical loads, not while driving purely resistive loads. In system dynamics, this study has found a global resonance condition which integrates the resonance condition for linear and nonlinear systems. The related results have proved

that the traditional condition of nonlinear resonances (i.e. sub- and super-harmonic resonances) is not true.

In this study, the potential of the method based on manipulating the roles of excitation has been shown in vibration energy harvesting, and the effects of non-resistive loads have been investigated. However, this study does not design and investigate an active harvester based on manipulating the roles of excitation, and also does not involve any optimization about the design of device (e.g. materials and dimensions) and circuits. To apply the active technology of vibration energy harvesting in reality, it is necessary to conduct some correlated investigations in the future. In addition, the concept of global resonance developed in this study also provides some new insights into nonlinear dynamics. The additional damping offered by a capacitor in an electromagnetic harvester provides a potential way to use damping to adjust device performance. Thus, further investigations which may be carried out in the future are summarized as follows:

- Design and development of an active harvester based on manipulating the roles of excitation. During this stage, besides theoretical and numerical evidence, the feasibility of the active method also need be validated by experimental evidence before it can be applied in practice.
- Optimization of the design of active device (e.g. materials and dimensions) and circuits. These factors also play a significant role in enhancing the efficiency of harvesters.
- Analytical methods based on the concept of global resonance should be developed for nonlinear dynamics.
- Potential of using damping to adjust device dynamics should be further investigated.

Bibliography

[1] C. B. Williams and R. B. Yates. Analysis of a micro-electric generator for microsystems. *Sensor. Actuat. A-Phys.*, 52:8–11, 1996.

[2] M. Umeda, K. Nakamura, and S. Ueha. Analysis of the tranformation of mechanical impact energy to electric energy using piezoelectric vibrator. *Jpn. J. Appl. Phys.*, 35:3267–3273, 1996.

[3] C. Shearwood and R. B. Yates. Development of an electromagnetic microgenerator. *Electronics Letters*, 33:1883–1884, 1997.

[4] R. Amirtharajah and A. P. Chandrakasan. Self-powered signal processing using vibration-based power generation. *IEEE Journal of Solid State Circuits*, 33(5):687–695, 1998.

[5] M. Goldfarb and L. D. Jones. On the efficiency of electric power generation with piezoelectric ceramic. *J. Dyn. Syst. Meas. Control*, 121:566–571, 1999.

[6] H. A. Sodano, D. J. Inman, and G. Park. A review of power harvesting from vibration using piezoelectric materials. *The Shock and Vibration Digest*, 36(3):197–205, 2004.

[7] S. P. Beeby, M. J. Tudor, and N. M. White. Energy harvesting vibration sources for microsystems applications. *Meas. Sci. Technol.*, 17:175–195, 2006.

[8] K. A. Cook-Chennault, N. Thambi, and A. M. Sastry. Powering mems portable devices-a review of non-regenerative and regenerative power supply systems with special emphasis on piezoelectric energy harvesting systems. *Smart Mater. Struct.*, 17:043001, 2008.

[9] R. L. Harne and K. W. Wang. A review of the recent research on vibration energy harvesting via bistable systems. *Smart Mater. Struct.*, 22:023001 (12pp), 2013.

[10] M. Daqaq, R. Masana, A. Erturk, and D. D. Quinn. On the role of nonlinearities in vibratory energy harvesting: A critical review and discussion. *Appl. Mech. Rev.*, 66:040801, 2014.

[11] H. Li, C. Tian, and Z. D. Deng. Energy harvesting from low frequency applications using piezoelectric materials. *Appl. Phys. Rev.*, 1:041301, 2014.

[12] S. D. Moss, O. R. Payne, G. A. Hart, and C. Ung. Scaling and power density metrics of electromagnetic vibration energy harvesting devices. *Smart Mater. Struct.*, 24:023001 (14pp), 2015.

[13] N. G. Stephen. On energy harvesting from ambient vibration. *J. Sound Vib.*, 293:409–425, 2006.

[14] L. Tang, Y. Yang, and C. K. Soh. Toward broadband vibration-based energy harvesting. *J. Intell. Mater. Syst. Struct.*, 21(18):1867–1897, 2010.

[15] E. S. Leland and P. K. Wright. Resonance tuning of piezoelectric vibration energy scavenging generators using compressive axial preload. *Smart Mater. Struct.*, 15:1413–1420, 2006.

[16] V. R. Challa, M. G. Prasad, Y. Shi, and F. T. Fisher. A vibration energy harvesting device with bidirectional resonance frequency tunability. *Smart Mater. Struct.*, 17:015035 (10pp), 2008.

[17] D.J. Morris, J.M. Youngsman, M.J. Anderson, and D.F. Bahr. A resonant frequency tunable, extensional mode piezoelectric vibration harvesting mechanism. *Smart Mater. Struct.*, 17:065021, 2008.

[18] X. Wu, J. Lin, S. Kato, K. Zhang, T. Ren, and L. Liu. A frequency adjustable vibration energy harvester. In *Proceedings of Power MEMS*, pages 245–248, Sendai, 2008.

[19] C. Peters, D. Maurath, W. Schock, F. Mezger, and Y. Manoli. A closed-loop wide-range tunable mechanical resonator for energy harvesting systems. *J. Micromech. Microeng.*, 19:094004, 2009.

[20] S.M. Shahruz. Design of mechanical band-pass filters for energy scavenging. *J. Sound Vib.*, 292:987–998, 2006.

[21] H. Xue, Y. Hu, and Q. Wang. Broadband piezoelectric energy harvesting devices using multiple bimorphs with different operating frequencies. *IEEE Trans. Ultrason. Ferroelectr. Freq. Control*, 55:2104–2108, 2008.

[22] M. Ferrari, V. Ferrari, M. Guizzetti, D. Marioli, and A. Taroni. Piezoelectric multifrequency energy converter for power harvesting in autonomous microsystems. *Sensor. Actuat. A-Phys.*, 142:329–335, 2008.

[23] J. Liu, H. Fang, Z. Xu, X. Mao, X. Shen, D. Chen, H. Liao, and B. Cai. A mems-based piezoelectric power generator array for vibration energy harvesting. *Microelectron. J.*, 39:802–806, 2008.

[24] A. R. M. Foisal, C. Hong, and G. Chung. Multi-frequency electromagnetic energy harvester using a magnetic spring cantilever. *Sensor. Actuat. A-Phys.*, 182:106–113, 2012.

[25] K. Mikoshiba, J. M. Manimala, and C. T. Sun. Energy harvesting using an array of multifunctional resonators. *J. Intell. Mater. Syst. Struct.*, 24:168, 2012.

[26] F. Cottone, H. Vocca, and L. Gammaitoni. Nonlinear energy harvesting. *Phys. Rev. Lett.*, 102(8):080601, 2009.

[27] L. Gammaitoni, I. Neri, and H. Vocca. Nonlinear oscillators for vibration energy harvesting. *Appl. Phys. Lett.*, 94(16):164102, 2009.

[28] A. Triplett and D. D. Quinn. The effect of non-linear piezoelectric coupling on vibration-based energy harvesting. *J. Intell. Mater. Syst. Struct.*, 20(16):1959–1967, 2009.

[29] R. Ramlan, M. J. Brennan, B. R. Mace, and I. Kovacic. Potential benefits of a non-linear stiffness in an energy harvesting device. *Nonlinear Dyn.*, 59:545–558, 2010.

[30] T. W. Ma. Opportunities for using nonlinear oscillators to enhance energy harvesting from impulsively loaded structures. *J. Sys. Control Eng.*, 225(4):467–474, 2011.

[31] B. P. Mann and N. D. Sims. Energy harvesting from the nonlinear oscillations of magnetic levitation. *J. Sound Vib.*, 319:515–530, 2009.

[32] B. Marinkovic and H. Kosera. Smart sanda wide bandwidth vibration energy harvesting platform. *Appl. Phys. Lett.*, 94:103505, 2009.

[33] D. A. W. Barton, S. G. Burrow, and L. R. Clare. Energy harvesting from vibrations with a nonlinear oscillator. *J. Vib. Acoust.*, 132(2):021009, 2010.

[34] L. G. W. Tvedt, S. D. Nguyen, and E. Halvorsen. Nonlinear behavior of an electrostatic energy harvester under wide- and narrowband excitation. *J. Microelectromech. Syst.*, 19:305–316, 2010.

[35] E. Sardini and M. Serpelloni. An efficient electromagnetic power harvesting device for low-frequency applications. *Sensor. Actuat. A-Phys.*, 172:475–482, 2011.

[36] G. Sebald, H. Kuwano, D. Guyomar, and B. Ducharne. Experimental duffing oscillator for broadband piezoelectric energy harvesting. *Smart Mater. Struct.*, 20:102001 (10pp), 2011.

[37] S. D. Nguyen and E. Halvorsen. Nonlinear springs for bandwidth-tolerant vibration energy harvesting. *J. Microelectromech. Syst.*, 20(6):1225–1227, 2011.

[38] X. Dai, X. Miao, L. Sui, H. Zhou, and X. Zhao. Tuning of nonlinear vibration via topology variation and its application in energy harvesting. *Appl. Phys. Lett.*, 100:031902, 2012.

[39] R. Xu, A. Lei, C. Dahl-Petersen, K. Hansen, M. Guizzetti, K. Birkelund, E.V. Thomsen, and O. Hansen. Screen printed pzt/pzt thick film bimorph mems cantilever device for vibration energy harvesting. *Sensor. Actuat. A-Phys.*, 188:383–388, 2012.

[40] P. Wang, H. Liu, X. Dai, Z. Yang, Z. Wang, and X. Zhao. Design, simulation, fabrication and characterization of a micro electromagnetic vibration energy harvester with sandwiched structure and air channel. *Microelectronics Journal*, 43:154–159, 2012.

[41] W. Hilber and B. Jakoby. A magnetic membrane actuator in composite technology utilizing diamagnetic levitation. *IEEE Sensors Journal*, 13(7):2786–2791, 2013.

[42] P. Huang, T. Tsai, and Y. Yang. Wide-bandwidth piezoelectric energy harvester integrated with parylene-c beam structures. *Microelectronic Engineering*, 111:214–219, 2013.

[43] A. Erturk, J. Holfmann, and D. J. Inman. A piezomagnetoelastic structure for broadband vibration energy harvesting. *Appl. Phys. Lett.*, 94:254102, 2009.

[44] M. Ferrari, M. Baú, M. Guizzetti, and V. Ferrari. A single-magnet nonlinear piezoelectric converter for enhanced energy harvesting from random vibrations. *Sensor. Actuat. A-Phys.*, 172:287–292, 2011.

[45] R. Masana and M. Daqaq. Energy harvesting in the super-harmonic frequency region of a twin-well oscillator. *J. Appl. Phys.*, 111:044501, 2012.

[46] Y. Zhu and J. W. Zu. Enhanced buckled-beam piezoelectric energy harvesting using midpoint magnetic force. *Appl. Phys. Lett.*, 103:041905, 2013.

[47] S. Zhou, J. Cao, A. Erturk, and J. Lin. Enhanced broadband piezoelectric energy harvesting using rotatable magnets. *Appl. Phys. Lett.*, 102:173901, 2013.

[48] A. F. Arrieta, T. Delpero, A. E. Bergamini, and P. Ermanni. Broadband vibration energy harvesting based on cantilevered piezoelectric bi-stable composites. *Appl. Phys. Lett.*, 102:173904, 2013.

[49] W. Q. Liu, A. Badel, F. Formosa, Y. P. Wu, and A. Agbossou. Novel piezoelectric bistable oscillator architecture for wideband vibration energy harvesting. *Smart Mater. Struct.*, 22:035013 (11pp), 2013.

[50] S.D. Nguyen, E. Halvorsen, and I. Paprotny. Bistable springs for wideband microelectromechanical energy harvesters. *Appl. Phys. Lett.*, 102:023904, 2013.

[51] M. Soliman, E. M. Abdel-Rahman, E. F. El-Saadany, and R. R. Mansour. A wideband vibration-based energy harvester. *J. Micromech. Microeng.*, 18:115021, 2008.

[52] M. Soliman, E. M. Abdel-Rahman, E. F. El-Saadany, and R. R. Mansour. A design procedure for wideband micropower generators. *J. Microelectromech. Syst.,*, 18:1288–1299, 2009.

[53] D. Hoffmann, B. Folkmer, and Y. Manoli. Fabrication, characterization and modelling of electrostatic micro-generators. *J. Micromech. Microeng.*, 19:094001, 2009.

[54] L. Blystad, E. Halvorsen, and S. Husa. Piezoelectric mems energy harvesting systems driven by harmonic and random vibrations. *IEEE Trans. Ultrason. Ferroelectr. Freq. Control*, 57(4):908–919, 2010.

[55] H. Liu, C. J. Tay, C. Quan, T. Kobayashi, and C. Lee. Piezoelectric mems energy harvester for low-frequency wibrations with wideband operation range and steadily increased output power. *J. Microelectromech. Syst.*, 20(5):1131–1142, 2011.

[56] H. Liu, C. Lee, T. Kobayashi, C. J. Tay, and C. Quan. A new s-shaped mems pzt cantilever for energy harvesting from low frequency vibrations below 30 hz. *Microsyst. Technol.*, 18:497–506, 2012.

[57] C. P. Le, E. Halvorsen, O. Srasen, and E. M. Yeatman. Microscale electrostatic energy earvester esing internal impacts. *J. Intell. Mater. Syst. Struct.,*, 23:1409–1421, 2012.

[58] L. C. J. Blystad and E. Halvorsen. A piezoelectric energy harvester with a mechanical end stop on one side. *Microsyst. Technol.*, 17(4):259–262, 2012.

[59] M. Daqaq. Response of uni-modal duffing-type harvesters to random forced excitations. *J. Sound Vib.*, 329:3621C3631, 2010.

[60] G. Sebald, H. Kuwano, D. Guyomar, and B. Ducharne. Simulation of a duffing oscillator for broadband piezoelectric energy harvesting. *Smart Mater. Struct.*, 20(7):075022, 2011.

[61] P. L. Green, K. Worden, K. Atallah, and N. D. Sims. The benefits of duffing-type nonlinearities and electrical optimisation of a mono-stable energy harvester under white gaussian excitations. *J. Sound Vib.*, 331:4504–4517, 2012.

[62] E. Halvorsen. Fundamental issues in nonlinear wideband-vibration energy harvesting. *Phys. Rev. E*, 87:042129, 2013.

[63] G. A. Lesieutre, G. K. Ottman, and H. F. Hofmann. Damping as a result of piezoelectric energy harvesting. *J. Sound Vib.*, 269:991–1001, 2004.

[64] D. Guyomar, A. Badel, E. Lefeuvre, and C. Richard. Toward energy harvesting using active materials and conversion improvement by nonlinear processing. *IEEE Trans. Ultrason. Ferroelectr. Freq. Control*, 52:584–595, 2005.

[65] X. Wang and L. Lin. Dimensionless optimization of piezoelectric vibration energy harvesters with different interface circuits. *Smart Mater. Struct.*, 22:085011 (20pp), 2013.

[66] M. Lallart and D. Guyomar. An optimized self-powered switching circuit for nonlinear energy harvesting with low voltage output. *Smart Mater. Struct.*, 17:035030 (8pp), 2008.

[67] Y.K. Ramadass and A.P. Chandrakasan. An efficient piezoelectric energy harvesting interface circuit using a bias-flip rectifier and shared inductor. *IEEE J. Solid-State Circuits*, 45(1):189–204, 2010.

[68] H. A. Sodano, D. J. Inman, and G. Park. Generation and storage of electricity from power harvesting devices. *J. Intell. Mater. Syst. Struct.*, 16(1):67–75, 2005.

[69] K. L. Turner, S. A. Miller, P. G. Hartwell, N. C. MacDonald, S. H. Strogatz, and S. G. Adams. Five parametric resonances in a microelectromechanical system. *Nature*, 396:149–152, 1998.

[70] J. J. Thomsen. *Vibrations and Stability: advanced theory, analysis, and tools.* Springer, 2003.

[71] D. R. Merkin. *Introduction to the Theory of Stability.* Springer, 1996.

[72] Sakae Yamamura. *AC Motors for High-Performance Applications.* Marcel Dekker, Inc., 1986.

[73] P. L. Cochran. *Polyphase Induction Motors.* Marcel Dekker, Inc., 1989.

[74] H. B. Radousky and H. Liang. Energy harvesting: an integrated view of materials devices and applications. *Nanotechnology*, 23:502001 (35pp), 2012.

[75] C. Hayashi. *Nonlinear oscillation in physical systems.* McGraw-Hill, New York, 1964.

[76] R. A. Horn and C. R. Johnson. *Matrix Analysis.* Cambridge University Press, 1985.

[77] N. G. Elvin, N. Lajnef, and A. A. Elvin. Feasibility of structural monitoring with vibration powered sensors. *Smart Mater. Struct.*, 15:977, 2006.

[78] T. W. Ma, H. Zhang, and N. S. Xu. A novel parametrically excited nonlinear energy harvester. *Mech. Syst. Signal Pr.*, 28:323–332, 2012.

[79] T. W. Ma and H. Zhang. Enhancing mechanical energy harvesting with dynamics escaped from potential well. *Appl. Phys. Lett.*, 100:114107, 2012.

[80] J. Miles. Resonance and symmetry breaking for the pendulum. *Physica D: Nonlinear Phenomena*, 31:252–268, 1988.

[81] A. F. Arrieta, P. Hagedorn, A. Erturk, and D. J. Inman. A piezoelectric bistable plate for nonlinear broadband energy harvesting. *Appl. Phys. Lett.*, 97:104102, 2010.

[82] T. Ma, N. Xu, and H. Zhang. A nonlinear method for harvesting mechanical energy from vibrations. In *Earth and Space 2010: Engineering, Science, Construction, and Operations in Challenging Environments*, pages 2267–2276, Honolulu, HI, March 2010.

[83] T. W. Ma and H. Zhang. Reaping the potentials of nonlinear energy harvesting with tunable damping and modulation of the forcing functions. *Appl. Phys. Lett.*, 104:214104, 2014.

[84] J. M. T. Thompson. Chaotic phenomena triggering the escape from a potential well. *Proc. R. Soc. Lond. A*, 421:195–225, 1989.

[85] M. J. Clifford and S. R. Bishop. Rotating periodic orbits of the parametrically excited pendulum. *Phys. Lett. A*, 201:191–196, 1995.

[86] H. Zhang and T. W. Ma. Iterative harmonic balance for period-one rotating solution of parametric pendulum. *Nonlinear Dyn.*, 70(4):2433–2444, 2012.

[87] H. Zhang and T. W. Ma. Period-one rotating solutions of horizontally excited pendulum based on iterative harmonic balance. *Advances in Pure Mathematics*, 5:413–427, 2015.

[88] W. Garira and S. R. Bishop. Rotating solutions of the parametrically excited pendulum. *J. Sound Vib.*, 263:233–239, 2003.

[89] X. Xu and M. Wiercigroch. Approximate analytical solutions for oscillatory and rotational motion of a parametric pendulum. *Nonlinear Dyn.*, 47:311–320, 2007.

[90] S. Lenci, E. Pavlovskaia, G. Rega, and M. Wiercigroch. Rotating solutions and stability of parametric pendulum by perturbation method. *J. Sound Vib.*, 310:243–259, 2008.

[91] S. Roundy and P. K. Wright. A piezoelectric vibration based generator for wireless electronics. *Smart Mater. Struct.*, 13:1131–1142, 2004.

[92] GT Hwang, H. Park, JH Lee, SK Oh, K Park, M. Byun, H. Park, G. Ahn, CK Jeong, K. No, HS Kwon, SG Lee, B. Joung, and KJ Lee. Self-powered cardiac pacemaker enabled by flexible single crystalline pmn-pt piezoelectric energy harvester. *Adv. Mat.*, 26(28):4880–4887, 2014.

[93] C. Dagdeviren, B.D. Yang, Y. Su, P.L. Tran, P. Joe, E. Adnerson, J. Xia, V. Doraiswamy, B. Dehdashti, X. Feng, B. Lu, R. Poston, Z. Khalpey, R. Ghaffari, Y. Huang, M.J. Slepian, and J.A. Rogers. Conformal piezoelectric energy harvesting and storage from motions of the heart, lung, and diaphragm. *Proc. Natl. Acad. Sci.*, 111(5):1927–1932, 2014.

[94] D. M. McFarland, L. A. Bergman, and A. F. Vakakis. Experimental study of non-linear energy pumping occurring at a single fast frequency. *Internat. J. Non-Linear Mech.*, 40:891–899, 2005.

[95] A. F. Vakakis, O. V. Gendelman, L. A. Bergman, D. M. McFarland, G. Kerschen, and Y. S. Lee. *Nonlinear targeted energy transfer in mechanical and structural systems.* Springer Science & Business Media, illustrated edition, 2008.

[96] R. L. Harne. Theoretical investigations of energy harvesting efficiency form structural vibraion using piezoelectric and electromagetic oscillators. *J. Acoust. Soc. Am.*, 132(1):162–172, July 2012.

[97] V. R. Challa, S. Cheng, and D. P. Arnold. The role of coupling strength in

the performance of electrodynamic vibrational energy harvesters. *Smart Mater. Struct.*, 22:025005 (11pp), 2013.

[98] A. K. Geim, M. D. Simon, M. I. Boamfa, and L. O. Heflinger. Magnet levitation at your fingertips. *Nature*, 400:323–324, 1999.

[99] P. A. Dunne, J. Hilton, and J.M.D. Coey. Levitation in paramagnetic liquids. *J. Magn. Magn. Mater.*, 316:273–276, 2007.

[100] L. Liu and F. G. Yuan. Nonlinear vibration energy harvester using diamagnetic levitation. *Appl. Phys. Lett.*, 98:203507, 2011.

[101] H. Sumali. Squeeze-film damping in the free molecular regime: model validation and measurement on a mems. *J. Micromech. Microeng.*, 17:2231C2240, 2007.

[102] S. W. Shaw and P. J. Holmes. A periodically forced piecewise linear oscillator. *J. Sound Vib.*, 90(1):129–155, 1983.